NSEL Report Series
Report No. NSEL-012
July 2008

Performance-based Engineering Framework and Ductility Capacity Models for Buckling-Restrained Braces

Blake M. Andrews
Larry A. Fahnestock
Junho Song

NSEL
NEWMARK STRUCTURAL ENGINEERING LABORATORY

Department of Civil and Environmental Engineering
University of Illinois at Urbana-Champaign

UILU-ENG-2008-1806

ISSN: 1940-9826

The Newmark Structural Engineering Laboratory (NSEL) of the Department of Civil and Environmental Engineering at the University of Illinois at Urbana-Champaign has a long history of excellence in research and education that has contributed greatly to the state-of-the-art in civil engineering. Completed in 1967 and extended in 1971, the structural testing area of the laboratory has a versatile strong-floor/wall and a three-story clear height that can be used to carry out a wide range of tests of building materials, models, and structural systems. The laboratory is named for Dr. Nathan M. Newmark, an internationally known educator and engineer, who was the Head of the Department of Civil Engineering at the University of Illinois [1956-73] and the Chair of the Digital Computing Laboratory [1947-57]. He developed simple, yet powerful and widely used, methods for analyzing complex structures and assemblages subjected to a variety of static, dynamic, blast, and earthquake loadings. Dr. Newmark received numerous honors and awards for his achievements, including the prestigious National Medal of Science awarded in 1968 by President Lyndon B. Johnson. He was also one of the founding members of the National Academy of Engineering.

Contact:
Prof. B.F. Spencer, Jr.
Director, Newmark Structural Engineering Laboratory
2213 NCEL, MC-250
205 North Mathews Ave.
Urbana, IL 61801
Telephone (217) 333-8630
E-mail: bfs@uiuc.edu

This technical report is based on the first author's M.S. thesis under the same title which was completed in July 2008. The second and third authors served as the thesis advisors for this work.

Financial support for this research was provided in part by the Dwight David Eisenhower Transportation Fellowship Program administered by the National Highway Institute, an organization of the Federal Highway Administration. This support is gratefully acknowledged. The authors also would like to thank Robert Tremblay for providing detailed information about the testing program described in [14] and Toru Takeuchi for communication regarding his BRB CPD capacity modeling concepts [20].

The cover photographs are used with permission. The Trans-Alaska Pipeline photograph was provided by Terra Galleria Photography (http://www.terragalleria.com/).

Abstract

Buckling-restrained braces (BRBs) have recently become popular in the United States for use as primary members of seismic lateral-force-resisting systems. A BRB is a steel brace that does not buckle in compression but instead yields in both tension and compression. Concentrically-braced frames incorporating BRBs are known as buckling-restrained braced frames (BRBFs). Although design guidelines for BRB application have been developed, procedures for assessing performance and quantifying reliability are needed.

This report proposes a performance-based engineering framework (PBEF) for a BRBF subjected to seismic loads. The proposed framework quantifies the risk of BRB failure due to low-cycle fatigue fracture of the BRB core. The components of the PBEF include: stochastic modeling of seismic loads; dynamic analyses of BRBFs; cumulative plastic ductility (CPD) (i.e. fatigue) models for buckling-restrained braces; structural reliability analyses; parametric studies on how BRB and BRBF properties affect performance; and fragility modeling. In addition to the report, appendix files are attached which provide detailed information on the research program.

For stochastic modeling of seismic loadings, input ground acceleration records were randomly generated from power spectrum models and modulated with envelope functions (to account for non-stationarity). The generated time records were used as input excitations to single-degree-of-freedom lumped-mass system models that represented the BRBFs. The BRB hysteretic behavior was modeled using a Bouc-Wen model. Non-linear dynamic time-history analyses were performed to obtain BRB core deformation time history records.

In this study, significant effort was made to develop models that predict BRB CPD capacity. The result was BRB remaining capacity (RC) models, which, given the BRB core deformation history as an input, predict the remaining CPD capacity of the brace, where values less than zero indicate failure.

Given BRB demand (i.e. core deformation histories generated from the dynamic analyses) and supply (i.e. remaining capacity predicted by the RC models), reliability analyses were performed to evaluate the probability of brace failure. The analyses were conducted using the first order reliability method. In the reliability analyses, the epistemic uncertainty in the fatigue capacity predictions was accounted for explicitly, and, as a result, the probabilities of brace failure were calculated in terms of mean probability, 90% confidence level probability, and 95% confidence level probability.

Using the tools described above, a parametric study was conducted to explore the effects of the seismic loading, BRB, and BRBF characteristics on the probability of brace failure. For given seismic loadings, surfaces of reliability indices were constructed in order to determine the probability of brace failure directly from BRB and BRBF properties, without the need to perform individual reliability analyses each time. Also, for a given set of BRB and BRBF properties, fragility curves were created that provide conditional probability of brace failure given ground shaking intensity parameters. Though this report describes the specific application of a PBEF to the BRB fatigue problem, the components of the PBEF may be interchanged independently, leading to great overall flexibility and the potential for application of the framework to many other problems.

Table of Contents

Chapter 1

INTRODUCTION

1.1 Background and Motivation

Buckling-restrained braces (BRBs) have recently become popular for use in the primary lateral-force-resisting systems of structures located in high seismic regions of the United States. Concentrically-braced frames (CBFs) incorporating BRBs are known as buckling-restrained braced frames (BRBF). A BRB is a steel brace that does not buckle in compression but instead yields in both tension and compression. It consists of an inner yielding steel structure and an outer restraining structure that prevents the inner structure from buckling. Often this outer structure is a concrete-filled steel tube (CFT). Figure 1.1 presents a typical CFT BRB [1], and Figure 1.2 shows a picture of BRBs manufactured by Star Seismic [25].

Since BRBFs are a relatively new structural system in the U.S., current design provisions require qualification tests to demonstrate acceptable BRB performance. Numerous isolated BRB tests have been conducted in support of building projects and as part of research programs [1-15], and several large-scale BRBFs have also been tested [16-18]. In general, these experiments have shown that BRBs exhibit robust cyclic performance and possess large ductility capacity. Although BRB cumulative ductility demands under seismic excitation can be reasonably estimated from nonlinear dynamic analysis [e.g. 19, 33], no generally accepted method exists for predicting the cumulative plastic ductility (CPD) capacity of BRBs, where CPD capacity is defined by the cumulative plastic deformation sustained before fracture of the steel core. In addition, CPD capacity has been shown to be dependent on loading history; Carden [9] and Fahnestock [16] have observed that braces which undergo large maximum deformations exhibit lower CPD capacity than those braces which undergo relatively smaller maximum deformations. Furthermore, other important parameters affecting capacity have not been clearly identified yet. As an effort to answer these needs, this research addresses the development of ductility capacity models for BRBs using the maximum likelihood estimation (MLE) method. Following the development of CPD capacity models, a performance-based engineering framework (PBEF) is developed which utilizes the CPD capacity models to predict the probability of brace failure when subjected to seismic loads. The PBEF is used to perform parametric studies and fragility analyses to explore the effects of the seismic loading, BRBF, and BRB properties on system reliability.

1.2 Prior and Related Research

Little research has been performed in the past to assess the ductility capacity of BRBs. One research program that has addressed CPD capacity of BRBs is that of Takeuchi et al. [20]. In this research, Takeuchi et al. developed a deterministic model for deformation capacity that is based on fatigue testing results for BRBs. Imposed brace deformation is divided into skeleton and Bauschinger parts as described by Benavent-

Climent [21]. The primary equation to predict cumulative plastic strain capacity is as follows:

$$\chi = \frac{1}{\frac{\alpha_s}{\chi_{SO}} + \frac{1-\alpha_s}{4}\left[\frac{\overline{\Delta}\varepsilon_{ph}^{\,1+m_2}}{C}\right]^{-1/m_2}} \tag{1.1}$$

where χ is the predicted cumulative plastic strain capacity; α_s is the ratio of cumulative plastic strain due to skeleton deformation to the total cumulative plastic strain; χ_{SO} is the cumulative plastic strain to the point of fracture caused by only skeleton plastic strain, which is regarded as the results from a simple tension test; $\overline{\Delta}\varepsilon_{ph}$ is half of the average plastic strain amplitude imposed on the BRB; and C and m_2 are obtained from a constant-amplitude fatigue test. To utilize the Takeuchi et al. model, then,

- A constant amplitude fatigue test must be performed to determine constants C and m_2 (Takeuchi et al. provide recommended values);
- χ_{SO} must be calculated from a simple tension test or estimated; and
- The imposed BRB force-deformation history must be analyzed using the Rainflow method [22] to determine the average plastic strain amplitude $\overline{\Delta}\varepsilon_{ph}$ and must be divided into skeleton and Bauschinger parts to determine α_s; or $\overline{\Delta}\varepsilon_{ph}$ and α_s, can be estimated from the maximum structural response as indicated by Akiyama [34].

While the Takeuchi et al. model is a significant step forward towards developing reliable BRB CPD capacity models, it has a few areas in which it could be improved, namely that:

1) Model error is not explicitly quantified (i.e. the model is deterministic);
2) Fatigue curves for BRBs must be known to use the model; and
3) Both the imposed force and deformation time histories must be known to predict CPD capacity (if estimated values of $\overline{\Delta}\varepsilon_{ph}$ and α_s are not used).

To improve CPD capacity modeling in these areas, in this research program, BRB CPD capacity models were developed that are probabilistic (i.e. they have an explicitly quantified model error) and are based upon knowing readily available brace properties (geometric and material properties) and only the imposed deformation history (no brace force data is required). Since the models are probabilistic, they are readily applicable to the PBEF described herein.

1.3 Contents and Layout

This research is divided into two parts. In Part 1, BRB CPD capacity models were created, and in Part 2, a performance-based engineering framework (PBEF) was developed. The goals of the research in Part 1 were to create CPD capacity models which could predict the failure of BRBs due to fatigue fracture. These models were to be as parsimonious as possible (having the fewest predictive terms) but also be accurate and precise. Furthermore, the models needed to be intuitive and readily applicable in an engineering analysis context. In Part 2 of the research, a PBEF was developed that utilizes the best CPD capacity models from Part 1 to predict the failure of BRBFs subjected to seismic loads due to fatigue fracture of BRBs. The PBEF was then utilized to perform parametric studies and fragility analyses to explore the effects of BRB and BRBF properties on the reliability of the BRBF system.

Overviews of Part 1 and Part 2 of the research program are given in Sections 1.4 and 1.5, respectively. Details of Part 1 and Part 2 of the research program are then covered in Chapters 1 to 6 and 7 to 11, respectively. Finally, conclusions and lessons learned from the research are given in Chapter 12.

1.4 Capacity Modeling Overview

The development of BRB CPD capacity models is outlined in the flowchart presented in Figure 1.3. In Chapter 2, the compilation of a BRB test database from literature review of brace tests is described; from this test database, predictive parameters were developed to be used as inputs to BRB CPD capacity models, and this is recounted in Chapter 3. Predictive parameters were divided into BRB material properties, geometric properties, and parameters that characterized the imposed deformation history. Following the creation of predictive parameters, CPD capacity models were developed using a MLE methodology. Three types of capacity models were investigated in this research:

1) End-capacity models: these predict a total, static CPD capacity of BRBs. If the imposed deformation exceeds the end-capacity, the BRB is said to fail.

2) Damage models: in these models, damage accumulates with imposed deformation and is measured by a damage index, where 0 indicates no damage, and 1 indicates failure.

3) Remaining capacity models: these are a combination of end-capacity and damage models. They predict the remaining CPD capacity available for a brace, which decreases with the applied deformation history. When remaining capacity reaches 0, the brace is said to fail.

End capacity models were developed first, and are described in Chapter 4. Next, damage models were investigated (Chapter 5). Finally, given lessons learned from the development of end-capacity and damage models, remaining capacity models were developed, and this is described in Chapter 6. The most applicable remaining capacity models were then used in Part 2 of this research, as described in the following section.

1.5 Performance-Based Engineering Framework Overview

In Part 2 of the research program, a performance-based engineering framework (PBEF) for a BRBF subjected to seismic loads was developed. The proposed framework quantifies the risk of BRB failure due to low-cycle fatigue fracture of the BRB core. The overall architecture of the PBEF is presented in Figure 1.4. The components of the PBEF can be divided into three categories: modules, analyses, and results. Modules were mathematical constructs used to model the physical reality; analyses were mathematical simulations performed in Matlab®; and results were the outputs from the analyses. In addition, two analysis tracks were outlined in this research. The first analysis pathway outlines the overall PBEF, while the second is a random vibration analysis that was performed beforehand and used to inform the development of the PBEF. The overall analysis flows and PBEF components are further summarized below.

The components of Analysis Pathway 1, the performance-based engineering framework (PBEF), include: stochastic modeling of seismic loads; dynamic analyses of the BRBF; CPD models for BRBs; structural reliability analyses; parametric studies on how BRB and BRBF properties affect performance; and fragility modeling. The analysis flow of the pathway is described below.

Using the **seismic loading input module**, input ground acceleration records were randomly generated from power spectrum models and modulated with envelope functions (to account for non-stationary). The generated time records were used as input excitations to the **BRBF system model**, which was a single-degree-of-freedom lumped-mass system. Within the **BRBF system model,** the BRB hysteretic behavior was modeled using a Bouc-Wen model [38]. **Non-linear dynamic simulations** were performed to obtain BRB core deformation time history records.

This study utilizes the **BRB remaining capacity models** described in Chapter 6. Given the BRB core deformation history as inputs, the fatigue model predicts the remaining CPD capacity of the brace, where values less than zero indicated failure. The epistemic uncertainty in the model was taken into account explicitly by an overall error term identified by the MLE method.

Given BRB demand (i.e. core deformation histories generated from the dynamic analyses) and capacity (i.e. remaining capacity predicted by the CPD models), structural **reliability analyses** were performed to evaluate the probability of brace failure. The analyses were conducted using the first order reliability method (FORM) [26] and facilitated by the Matlab® open-source code, Finite Element Reliability Using Matlab® (FERUM) [27]. In the reliability analyses, the epistemic uncertainty in the fatigue capacity predictions was accounted for explicitly, and, as a result, the probabilities of brace failure were calculated in terms of mean probability, 90% confidence level probability, and 95% confidence level probability.

Using the tools described above, a **parametric study** was conducted to explore the effects of the seismic loading, BRB, and BRBF characteristics on the probability of brace failure. For given seismic loadings, surfaces of reliability indices were constructed in order to determine the probability of brace failure directly from BRB and BRBF properties. Also, for a given set of BRB and BRBF properties, **fragility analyses** were created that provided conditional probability of brace failure given ground motion intensity parameters.

Related to but separate from Analysis Pathway 1 (the PBEF) is Analysis Pathway 2, which describes a random vibration analysis, which was actually performed before development of Analysis Pathway 1 and the PBEF. The main purpose of the random vibration analysis was to determine the mean and variance of the BRB core deformation process such that distributions of the deformation descriptor predictor parameters described in Chapter 3 could be evaluated. This was accomplished by performing random vibration analysis using the **BRBF system model**, where the non-linear equations of motion were linearized using the equivalent linearization method (ELM) [28]. Using the random vibration analysis tools, the effects of seismic loading, BRB, and BRBF properties on the mean and variance of the BRB core deformation process were determined. Thus the effects of the seismic loading, BRB, and BRBF properties on BRB demands and system reliability were quantified, and this provided information about which parameters were important for consideration in the PBEF.

1.6 Introduction Figures

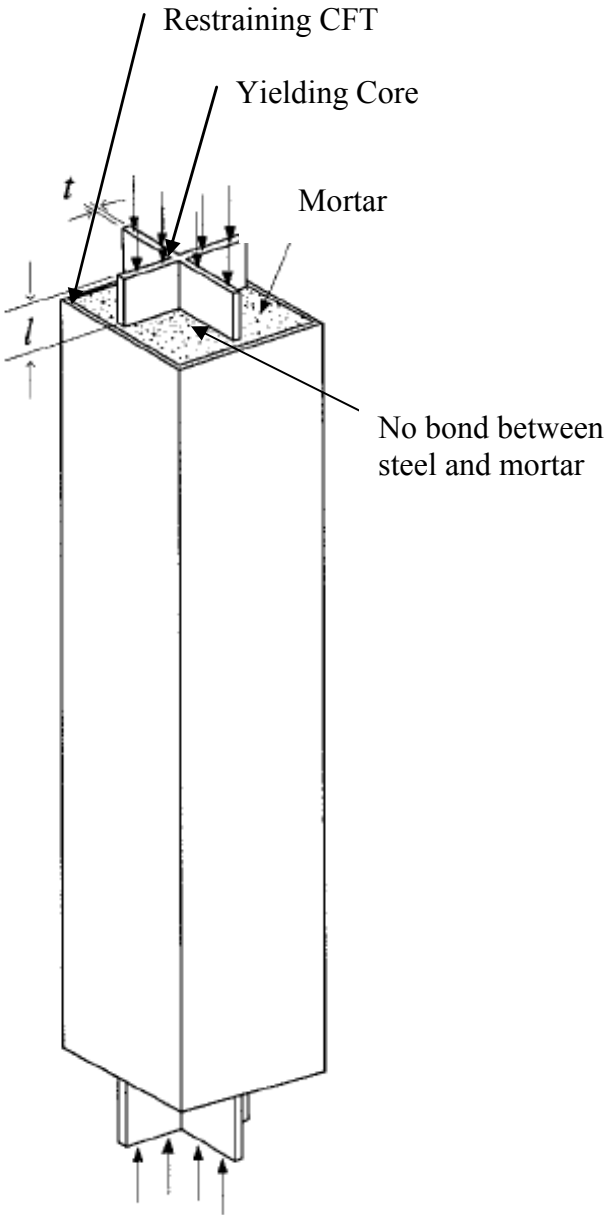

Figure 1.1: Typical BRB [1]

Figure 1.2: Star Seismic BRBs [25]

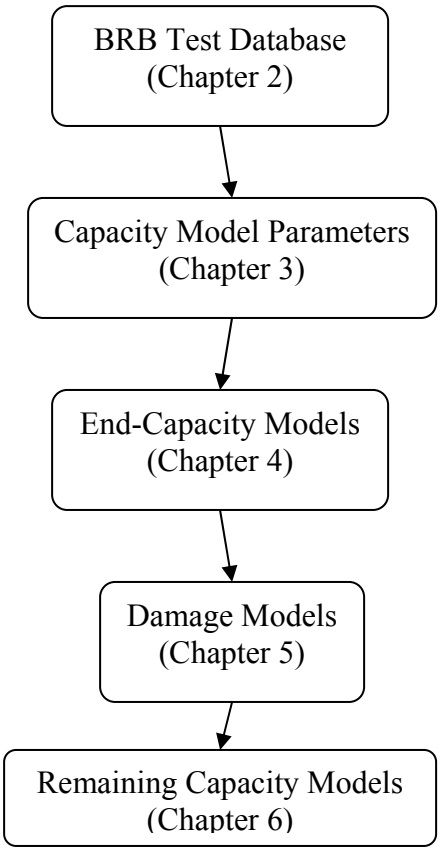

Figure 1.3: Capacity Modeling Overview

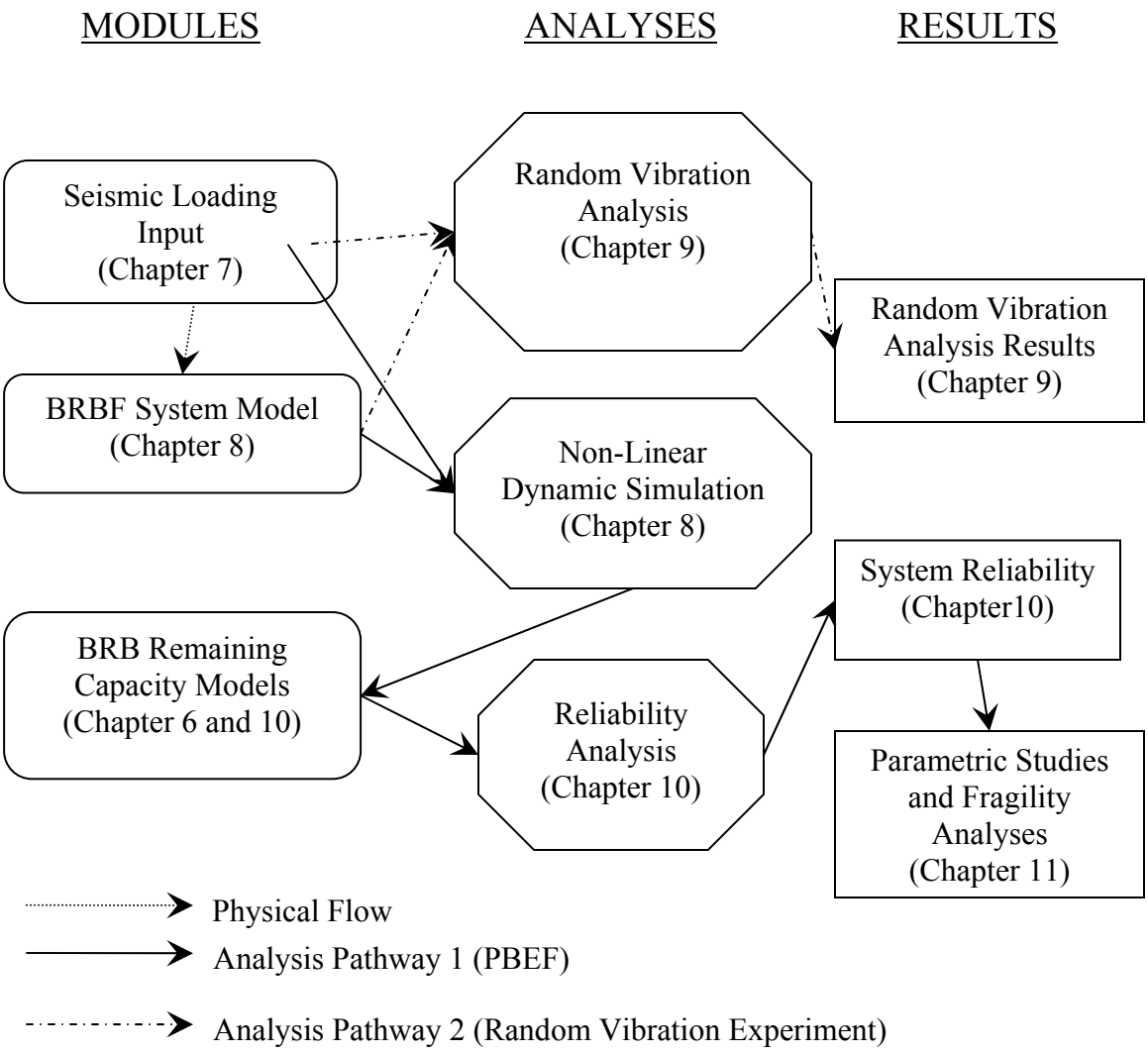

Figure 1.4: Performance-Based Engineering Framework Architecture

Chapter 2

BRB TEST DATABASE

2.1 BRB Components

Figure 2.1 shows the schematic layout of a typical BRB (shown without its restraining structure); it depicts the three primary regions of a brace: the core region, which is designed to yield, the transition region, and the end region, which is the part of the BRB connected to other structural elements. Three types of information were collected in this study to describe BRBs and their behavior: (1) geometric properties, (2) material properties, and (3) the applied deformation histories. The geometric properties of a BRB include its core region shape (rectangular versus cruciform), the core region slenderness (b/t), core region cross-sectional area (A_c), and core region length (L_c). Material properties include the steel yield strength (F_y) and steel ultimate strength (F_u). Finally, the applied deformation history may be described by deformation versus increment data or by cycle-amplitude pairs (see Section 2.3 for deformation classifications).

2.2 BRB Test Database Overview

A BRB test database was compiled through literature review [1-16] of brace tests performed by researchers from around the world with the majority of testing performed in the U.S. and Japan. The database is composed of 76 specimens total, of which 34 failed due to fracture during testing, and 42 did not fail. For each specimen, the test database contains brace geometrical properties, material properties, and the imposed deformation history. In general, the test database does not contain brace axial force data. Table 2.1 summarizes the BRB test database, while Table 2.2 provides a summary of BRB properties and links to the references for BRB testing documentation. Note that BRBs are classified by master identification (ID) numbers in Table 2.2, which are used throughout this research to identify particular BRBs. For complete database information, see, in Appendix A, Table A.1 for complete BRB information and Table A.2 for applied deformation histories.

2.3 Deformation Classifications

In general, deformations are classified as either *gauge length deformation* (Δ_g), or *core deformation* (Δ_c). Gauge length deformation is the deformation occurring across the gauge length (see Figure 2.1) that is measured by sensors during testing. Sensor locations and gauge length vary by BRB test setup. Core deformation is the deformation which occurs across the BRB core region. Table A.2 in Appendix A contains the deformation histories (all in terms of gauge length deformation versus increment) imposed on the BRBs in the database during testing. Two types of histories were imposed on specimens: a regular cyclic history (67 BRBs) and a simulated seismic loading (9 BRBs).

2.4 Chapter 2 Figures

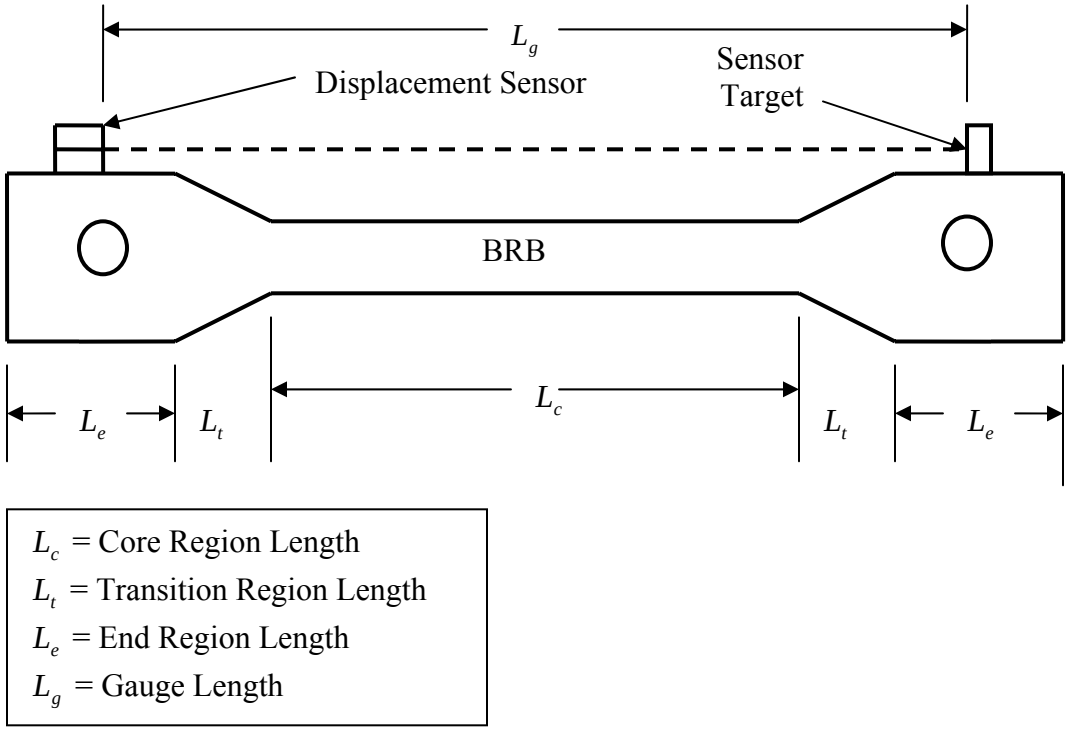

Figure 2.1: Typical BRB Layout

2.5 Chapter 2 Tables

Table 2.1: BRB Test Database Parameters

Parameter	Minimum	Mean	Maximum
b/t	0.15	5.87	11.78
A_c (in^2)	0.63	8.35	28.62
L_c (in)	17.25	96.84	185.9
F_y (ksi)	32.2	42.2	60.7
F_u (ksi)	44.0	61.8	71.4
P_y (kip)	20.4	347.8	1202
Δ_{yc} (in)	0.02	0.14	0.29
Δ_{yt} (in)	0.02	0.17	0.41

Table 2.2: BRB Basic Information

ID Number	Reference	A_c (in^2)	L_c (in)	F_y (ksi)	F_u (ksi)	P_y (kip)	Fracture during Testing?
1	1	4.50	121.70	60.7		273.2	NO
2	1	6.00	117.70	60.7		364.2	YES
3	1	8.00	135.80	60.7		485.6	NO
4	1	11.04	134.30	41.1		453.7	NO
5	1	11.04	134.30	41.1		453.7	NO
6	2	10.00	133.00	38.9	65.0	388.0	YES
7	2	10.00	133.00	38.9	65.0	388.0	YES
8	2	16.00	131.00	44.5	64.6	712.0	YES
9	2	16.00	131.00	44.5	64.6	712.0	YES
10	2	23.13	130.00	38.9	65.0	897.3	YES
11	2	23.13	130.00	38.9	65.0	897.3	YES
12	3	3.80	176.00	42.0	63.2	160.0	YES
13	3	5.96	179.40	42.0	63.2	250.0	YES
14	3	8.34	183.30	42.0	63.2	350.0	NO
15	3	12.66	185.10	39.5	66.2	500.0	NO
16	3	17.85	184.20	42.0	63.2	750.0	NO
17	3	17.87	179.40	42.0	63.2	750.0	NO
18	3	28.53	185.20	42.0	63.2	1198.0	NO
19	3	28.62	181.30	42.0	63.2	1202.0	NO
20	4	16.12	107.09	36.6	61.2	598.0	YES
21	4	19.84	111.46	32.2	48.6	663.2	YES
22	5	1.32	53.35	44.4	62.7	58.4	NO
23	6	4.36	49.25	38.1	61.2	166.4	NO
24	7	4.36	49.25	38.1	61.2	166.4	NO
25	7	1.93	49.25	42.8	64.5	82.7	NO
26	7	2.46	49.25	42.8	64.5	105.0	NO
27	7	2.58	49.25	41.9	63.8	108.1	NO
28	7	3.42	49.25	41.9	63.8	143.4	NO
29	7	4.36	49.25	41.9	63.8	183.0	NO
30	7	3.00	49.25	40.3	61.6	121.2	NO
31	7	3.55	49.25	40.3	61.6	143.2	NO
32	7	4.36	49.25	38.1	61.2	166.4	NO
33	7	2.58	49.25	41.9	63.8	108.1	YES
34	7	3.42	49.25	41.9	63.8	143.4	NO
35	7	3.00	49.25	40.3	61.6	121.2	NO
36	7	4.36	51.18	38.1	62.7	166.8	YES
37	8	2.61	121.65	41.0		107.0	NO
38	8	2.61	121.65	41.0		107.0	NO
39	8	2.62	121.65	41.0		107.2	NO
40	9,10	0.63	17.25	32.6	44.0	20.4	YES
41	9,10	0.63	17.25	32.6	44.0	20.4	YES
42	9,10	0.63	17.25	32.6	44.0	20.4	YES

Table 2.2: BRB Basic Information (continued)

ID Number	Reference	Ac (in^2)	Lc (in)	Fy (ksi)	Fu (ksi)	Py (kip)	Fracture during Testing?
43	9,10	0.63	17.25	32.6	44.0	20.4	YES
44	9,10	0.63	17.25	32.6	44.0	20.4	YES
45	9,10	0.63	17.25	32.6	44.0	20.4	YES
46	9,10	0.63	17.25	32.6	44.0	20.4	YES
47	11	4.00	100.22	46.0	61.0	184.0	YES
48	11	4.00	73.81	46.0	61.0	184.0	YES
49	11	9.00	92.74	42.0	68.0	378.0	NO
50	11	9.00	65.81	42.0	68.0	378.0	YES
51	11	20.00	54.50	42.0	68.0	840.0	NO
52	11	20.00	54.50	42.0	68.0	840.0	NO
53	16	2.17	78.00	46.0		100.0	NO
54	16	2.17	78.00	46.0		100.0	YES
55	16	1.74	65.00	46.0		80.0	YES
56	16	1.74	65.00	46.0		80.0	YES
57	16	1.30	64.00	46.0		60.0	YES
58	16	1.30	64.00	46.0		60.0	YES
59	16	0.65	65.00	46.0		30.0	NO
60	16	0.65	65.00	46.0		30.0	NO
61	12	24.08	185.88	45.6	64.3	1098.0	NO
62	12	24.08	185.88	45.6	64.3	1098.0	NO
63	12	23.56	185.88	42.0	69.3	990.0	NO
64	13	3.68	152.70	41.4		152.1	YES
65	13	3.68	152.70	41.4		152.1	YES
66	13	5.75	134.70	39.9		229.4	YES
67	13	5.75	134.70	39.9		229.4	YES
68	13	11.50	134.70	39.9		458.9	NO
69	13	11.50	134.70	39.9		458.9	NO
70	13	19.52	132.60	39.9		778.8	YES
71	14	2.46	97.76	53.7	71.4	132.0	NO
72	14	2.46	39.41	53.7	71.4	132.0	NO
73	14	2.46	39.41	53.7	71.4	131.9	YES
74	14	2.45	39.41	53.7	71.4	131.5	NO
75	15	27.00	144.50	37.5	70.3	1012.5	NO
76	15	27.00	144.50	37.5	70.3	1012.5	YES

Chapter 3

CAPACITY MODEL PARAMETERS

3.1 Parameters Overview

In order to evaluate the factors affecting BRB CPD capacity and to produce the best BRB CPD capacity models, a wide variety of predictive parameters were investigated. The predictive parameters used in this research (denoted by *h*) can be divided into three groups: (1) brace geometric properties, (2) brace material properties, and (3) descriptors of the imposed deformation history. The following sections describe these parameters and how they are derived.

3.2 Brace Property Parameters

Brace property parameters relate to either material or geometric properties of the BRB. Table 3.1 lists all brace property parameters. While A_c, L_c, ε_{yc}, and F_y data was available for all BRBs in the test database, b/t and F_u data were available for 53 of 76 and 70 of 76 BRB specimens, respectively.

3.3 Deformation History Parameters

Many parameters were created (or defined) to aid in describing the deformation histories imposed on the BRB specimens in hope that these descriptive parameters would be useful in predicting overall CPD capacity. These "deformation history predictive parameters" are summarized in Table 3.2 and are more fully explained in the sections that follow.

The software Matlab® was used to calculate the deformation history parameters, and all Matlab® programming files (which may be opened as text documents) and associated files used to calculate the parameters are presented in Appendix B. A summary of the values of the deformation history parameters for all BRB specimens (results of the Matlab® calculations) is given in Table 3.3. The complete set of values is presented in Table B.1 in Appendix B.

3.3.1 Force-Deformation Model

Since the BRB test database does not contain force data for most specimens, a force-deformation model predicting the yielding of the BRB steel core must be defined. In this research, an elastic-perfectly plastic force-deformation model, as shown in Figure 3.1, is assumed. The x and y axes of the figure represent BRB core deformation and brace axial force, respectively.

The CPD capacity of the BRB test specimens as well as other deformation descriptor predictive parameters were determined by assuming that the steel BRB core behaves according to the force-deformation model shown in Figure 3.1 when subjected to

an imposed deformation history. The CPD was calculated by summing all excursions into the plastic domain (such as excursions 1, 2, and 3 in Figure 3.1) throughout the deformation history.

3.3.2 Ductility Parameters

In general, ductility demand (μ) is defined herein as BRB core deformation at specific point in time (or at a specific increment *i*) in a deformation history normalized by the core deformation at incipient yielding; i.e. $\mu = \frac{\Delta_c}{\Delta_{yc}}$. Cumulative plastic ductility (CPD) demand is the summation of all plastic core deformation ($\sum \Delta_p$) occurring up to a specific deformation increment, normalized by the yield deformation, i.e. $\mu_c = \frac{\sum \Delta_p}{\Delta_{yc}}$.

Ductility demands may be further classified as positive or negative, indicating deformation that causes extension and shortening, respectively. Moreover, the largest absolute ductility demand (considering both positive and negative demands) over a deformation history is defined as $\mu_{\max}$. The maximum positive demand is $(\mu_{pos})_{\max}$, while the largest (or most negative) negative ductility demand is denoted by $(\mu_{neg})_{\max}$.

In a similar fashion to ductility demands, CPD may be classified as positive or negative. Positive CPD ($(\mu_c)_{pos}$) is that plastic deformation that occurs during net core extension (i.e. when $\Delta_c > 0$). Conversely, negative CPD ($(\mu_c)_{neg}$) is that plastic deformation that occurs when the core is shortened (i.e. when $\Delta_c < 0$). Furthermore, CPD may be classified as tensile or compressive, where tensile CPD ($(\mu_c)_{tens}$) is that plastic deformation occurring due to a tensile brace axial force, and compressive CPD ($(\mu_c)_{comp}$) is that plastic deformation occurring due to a compressive axial force. Therefore, in reference to Figure 3.1, positive CPD occurs to the right of the P axis and negative CPD to the left, while tensile CPD occurs above the Δ axis, and negative CPD occurs below it.

Finally, CPD demand may be classified by its value at different points in an applied deformation history. Three such points were considered in this research: CPD demand at $(\mu_{pos})_{\max}$, at $(\mu_{neg})_{\max}$, and at the end of the history (at the location of maximum CPD). The classification of CPD at different points in an applied deformation history may allow for further quantitative characterization of that deformation history.

3.3.3 Plastic Excursions

The plastic excursion (PE) terms in Table 3.2 are related to the PE distribution: count (N_{PE}), mean value (μ_{PE}), standard deviation (σ_{PE}), skewness (υ_{PE}), and coefficient of variation (COV_{PE}). A single PE is defined as the sum of all core deformation (expressed as ductility) occurring consecutively in the plastic domain (see Figure 3.1). A PE begins at the yield point and ends when unloading commences. Many

such single PEs occur during a typical load history, and the aggregation of these single PEs forms the PE distribution.

3.3.4 Rainflow Cycle Counting

Rainflow (RF) distribution terms are related to the RF distribution: count (N_{RF}), mean value (μ_{RF}), standard deviation (σ_{RF}), skewness (υ_{RF}), and coefficient of variation (COV_{RF}). The RF distribution is a distribution of cycle amplitudes (plastic deformation only) calculated from the deformation history using the Rainflow Method [22]. This method converts the irregular deformation history into a cyclic deformation history composed of full and half cycles.

3.4 Chapter 3 Figures

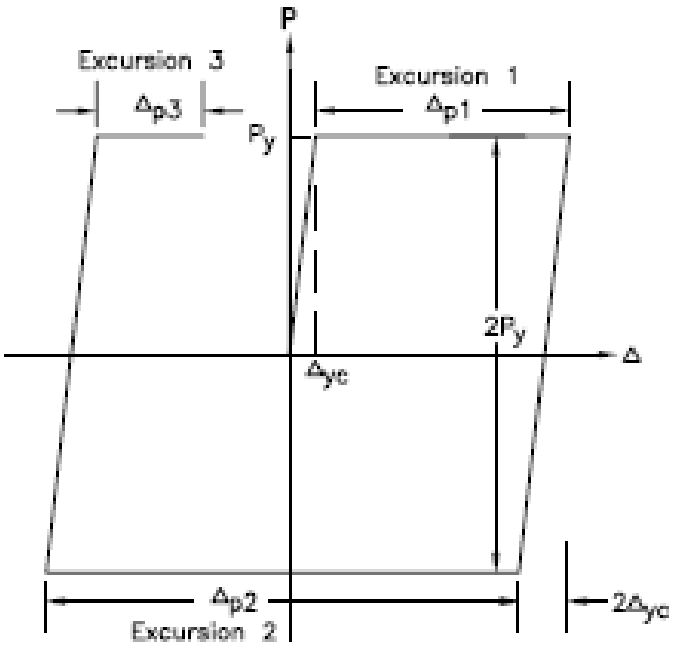

Figure 3.1: BRB Core Force-Deformation Model

3.5 Chapter 3 Tables

Table 3.1: Brace Property Parameters

Constants	Geometric Properties	Material Properties
$h_1 = 1$	$h_3 = A_c / (A_c)_{\max}$	$h_6 = \varepsilon_{yc}$
$h_2 = 2$	$h_4 = L_c / (L_c)_{\max}$	$h_7 = F_u / F_y$
	$h_5 = b / t$	

Table 3.2: Deformation History Parameters

Ductility Demands	CPD Parameters		Plastic Excursion Distribution	Rainflow Distribution
$h_{10} = (\mu_{pos})_{\max}$ $h_{11} = (\mu_{neg})_{\max}$ $h_{12} = \mu_{\max}$	$h_{20} = \mu_c$ $h_{21} = (\mu_c)_{pos}$ $h_{22} = (\mu_c)_{neg}$ $h_{23} = (\mu_c)_{tens}$ $h_{24} = (\mu_c)_{comp}$	at end of history	$h_{40} = N_{PE}$ $h_{41} = \mu_{PE}$ $h_{42} = \sigma_{PE}$ $h_{43} = \upsilon_{PE}$ $h_{44} = COV_{PE}$	$h_{50} = N_{RF}$ $h_{51} = \mu_{RF}$ $h_{52} = \sigma_{RF}$ $h_{53} = \upsilon_{RF}$ $h_{54} = COV_{RF}$
	$h_{25} = \mu_c$ $h_{26} = (\mu_c)_{pos}$ $h_{27} = (\mu_c)_{neg}$ $h_{28} = (\mu_c)_{tens}$ $h_{29} = (\mu_c)_{comp}$	at $(\mu_{pos})_{\max}$		
	$h_{30} = \mu_c$ $h_{31} = (\mu_c)_{pos}$ $h_{32} = (\mu_c)_{neg}$ $h_{33} = (\mu_c)_{tens}$ $h_{34} = (\mu_c)_{comp}$	at $(\mu_{neg})_{\max}$		

Table 3.3: Deformation History Parameter Summary

			Minimum	Maximum	Average
Ductility Demands		$h_{10} = (\mu_{pos})_{\max}$	7.81	54.75	20.21
		$h_{11} = (\mu_{neg})_{\max}$	–41.72	–6.66	–18.74
		$h_{12} = \mu_{\max}$	7.81	54.75	21.09
CPD Parameters	At End of History	$h_{20} = \mu_c$	58.00	4079.27	841.38
		$h_{21} = (\mu_c)_{pos}$	28.50	2461.50	437.35
		$h_{22} = (\mu_c)_{neg}$	29.13	1617.77	404.03
		$h_{23} = (\mu_c)_{tens}$	28.50	2033.38	420.75
		$h_{24} = (\mu_c)_{comp}$	29.50	2045.89	420.63
	at $(\mu_{pos})_{\max}$	$h_{25} = \mu_c$	8.28	2479.31	432.49
		$h_{26} = (\mu_c)_{pos}$	8.28	1189.27	218.52
		$h_{27} = (\mu_c)_{neg}$	0.00	1290.04	213.97
		$h_{28} = (\mu_c)_{tens}$	8.28	1258.28	225.85
		$h_{29} = (\mu_c)_{comp}$	0.00	1221.03	206.64
	at $(\mu_{neg})_{\max}$	$h_{30} = \mu_c$	24.85	1083.95	416.82
		$h_{31} = (\mu_c)_{pos}$	1.20	536.68	216.08
		$h_{32} = (\mu_c)_{neg}$	9.28	547.27	200.74
		$h_{33} = (\mu_c)_{tens}$	8.28	526.62	199.54
		$h_{34} = (\mu_c)_{comp}$	16.57	557.34	217.28

Table 3.3: Deformation History Parameter Summary (continued)

		Minimum	Maximum	Average
Plastic Excursion Distribution	$h_{40} = N_{PE}$	3	250	64
	$h_{41} = \mu_{PE}$	2.60	40.99	14.72
	$h_{42} = \sigma_{PE}$	0.92	26.63	10.12
	$h_{43} = \upsilon_{PE}$	-8.83	2.86	0.43
	$h_{44} = COV_{PE}$	0.06	1.53	0.77
Rainflow Distribution	$h_{50} = N_{RF}$	2	181	42
	$h_{51} = \mu_{RF}$	0.51	16.79	6.82
	$h_{52} = \sigma_{RF}$	0.72	13.21	5.04
	$h_{53} = \upsilon_{RF}$	–6.08	5.47	0.80
	$h_{54} = COV_{RF}$	0.09	3.18	0.99

Chapter 4

CAPACITY MODELING

To study the CPD capacity of BRBs in greater depth, the maximum likelihood estimation (MLE) methodology [35] was employed to construct capacity models based on experimental observations in the literature. The MLE method is a probabilistic regression to find optimal model parameters based on the probabilities that the model would predict the observed data. This chapter provides an overview and outline of the capacity modeling process; shows the modeling results for all trial end-capacity models; identifies those parameters shown to be most important to predicting BRB CPD capacity; and summarizes conclusions and lessons-learned from the capacity modeling process. Chapters that follow elaborate on modeling results for different capacity model forms, i.e. damage models and remaining capacity models.

The procedure for developing BRB CPD capacity models consists of the following four steps: (1) model form definition, (2) model fitting, (3) model reduction, and (4) error analysis.

4.1 Model Form Definition

The general end-capacity model takes the form

$$C = \gamma(\boldsymbol{\theta}, \mathbf{h}) + \sigma\varepsilon \tag{4.1}$$

where C is the predicted ultimate CPD capacity (the total amount of CPD that a BRB can sustain without fracture); $\gamma(\boldsymbol{\theta}, \mathbf{h})$ is the model form; $\boldsymbol{\theta}$ is a vector of model parameters (used to fit the model to test data); $\mathbf{h}$ is a vector of predictive parameters (defined in Chapter 3); σ is the model error magnitude; and ε is the standard normal random variable (zero mean and unit variance). While other model forms exist (such as damage models and remaining capacity models), that given in equation 4.1 is the simplest model form that contains all typical modeling components. In the following chapters, the model form is altered, but all variables remain similarly defined.

4.2 Model Fitting

The MLE method [36] was used to calibrate the model parameters in equation 4.1. The likelihood function $L(\boldsymbol{\theta}, \sigma)$ is proportional to the probability that the capacity model in equation 4.1 agrees with the test results for given $\boldsymbol{\theta}$. The residual, the difference between the predicted capacity and test values, is defined as

$$r = C_{test} - \gamma(\boldsymbol{\theta}, \mathbf{h}) = \sigma\varepsilon \tag{4.2}$$

where C_{test} is the capacity from test results. The likelihood function is defined such that it is proportional to the probability that the capacity model *exactly* matches the test results for failure data and predicts a value *greater* than that from test results for non-failure

data. This is logical, as for non-failure specimens, the CPD values at the end of the test are not the specimens' ultimate capacities, and the model should predict greater values than the end-of-test values. Thus the likelihood function is given as

$$L(\boldsymbol{\theta},\sigma) \propto \prod_{\text{failure data}} P(\varepsilon = r_i / \sigma) \times \prod_{\text{non-failure data}} P(\varepsilon > r_i / \sigma) \tag{4.3}$$

Since the residual is a function of the standard normal random variable ε, the likelihood function is calculated as

$$L(\boldsymbol{\theta},\sigma) \propto \prod_{\text{failure data}} \varphi(r_i / \sigma) / \sigma \times \prod_{\text{non-failure data}} \Phi(-r_i / \sigma) \tag{4.4}$$

in which $\varphi(\cdot)$ and $\Phi(\cdot)$, respectively, denote the probability density function and cumulative distribution function of the standard normal distribution.

In this research, instead of obtaining the mean values of the parameters in the posterior distribution by a Bayesian method [35], the values of parameters $\boldsymbol{\theta}$ and σ are determined as those that maximize the likelihood function. These "maximum likelihood estimators" give a good approximation to the posterior mean values by Bayesian method, as it is well known that, under some mild conditions, the difference between the maximum likelihood estimator and the posterior mean asymptotically approaches zero as the number of observations grow [35]. To implement the MLE method, an iterative non-linear minimization algorithm from Matlab® was used which determined the values of $\boldsymbol{\theta}$ and σ that maximized the value of equation 4.4. See Appendix C for details of the Matlab® codes used in this chapter for capacity modeling.

The negative of the inverse of the Hessian of the log-likelihood function, $-\left[\nabla\nabla \ln\left(L(\boldsymbol{\theta},\sigma)\right)\right]^{-1}$, evaluated at the maximum-likelihood estimator (values of $\boldsymbol{\theta}$ and σ which maximize the likelihood function) asymptotically approaches the posterior covariance matrix [35]. Values from this covariance matrix were used to approximate the COV of the parameters $\boldsymbol{\theta}$ and σ. While determining the mean and COV of the posterior distribution using the MLE method and the Hessian is an approximation, it is accurate enough and is much more efficient than performing numerical integration. Thus, these approximate methods were used in this research.

4.3 Model Reduction

Following the capacity model fitting, model reduction was performed. In this process, predictive parameters in **h** were removed in an iterative fashion such that the number of predictor terms was minimized with model error (which is proportional to σ) maintained at a level judged to be reasonably low. Three model reduction schemes were used to accomplish this. The first is reduction using the coefficient of variation (COV) of the model parameters $\boldsymbol{\theta}$ to decide which predictive parameters to remove. The COV of a specific model parameter θ_i indicates the relative importance of the predictor parameter h_i associated with that model parameter. Higher values of COV indicate lower importance in predicting the capacity. Thus, in a given iteration, the predictor term with

the largest COV was removed. The reduced model was then re-fit to the test data for the next iteration.

The second reduction scheme may be termed as the "look forward" method. In this method, an initial capacity model was created, and then evaluated by individually removing each predictor term h_i. For each case, the reduced model was refit to test data, and the error of the reduced model (measured by the MLE of σ) was found. The reduced model (created by removing one predictor term from the initial model) with the lowest MLE value of σ was chosen as the initial capacity model for the next reduction step. This process was repeated until a sufficient number of predictor terms were removed or the predictor terms could not be removed any more without significant increase in σ.

The third reduction scheme was simply a trial and error method, wherein the results from methods 1 and 2 above were used to obtain insight into the relative importance and influence of each predictor term. Intuition was used to find the most accurate, yet simplest model.

4.4 Error Analysis

Error analysis was performed for each capacity model to ascertain the precision of the model using the test data. The distribution of $Z = C_{predict} / C_{test}$ was constructed using all specimens in the test database *that failed*, where $C_{predict}$ is the predicted capacity from the capacity model, and C_{test} is the measured capacity from testing. A mean value of *Z* is usually greater than 1 because the model is constructed using both failure and non-failure data and thus tends to over-predict the capacity for failure specimens. The COV of *Z* was used as an indicator of the precision of a particular model.

4.5 End-Capacity Modeling Results

In this section, the capacity model fitting results for end-capacity models are summarized. Table 4.1 provides an overview of results, and table contents are defined as follows: $\gamma(\boldsymbol{\theta}, \mathbf{h})$ is the model form used in the capacity model; **h** is the list of predictive parameters used in the model (see Table 3.1 and Table 3.2 for definitions); "Full Model" is the initial model constructed before any model reduction is performed; "Optimal Model" is the model identified through the model reduction process as being the best balance between model size and precision; n_h is the number of predictive terms in the model; μ_Z is the mean value of the *Z* distribution discussed in Section 4.4 ; and COV_Z is the coefficient of variation of the *Z* distribution.

Comparisons between test results and model predictions for Optimal Model 1, Optimal Model 2, Optimal Model 3, Model 4a, Model 4b, and Optimal Model 5 are shown in Figure 4.1 through Figure 4.6. In each figure, the model prediction is shown as a solid line, while test results for failure specimens and non-failure specimens are shown as X's and O's, respectively. The equations for the predicted model capacity, $C_{predict}$, and the model error, σ, are given for the models in Table 4.2 through Table 4.7. In general, those models with higher error show more scatter of the test values around the model curve. Moreover, the model prediction, in general, tends to go through the middle of failure data

and slightly above non-failure data. This is logical, as the model should predict values higher than the test values for non-failure specimens.

The first model created was Model 1, which includes a large set of predictive parameters (25 to start). The purpose of this model was to consider all possible predictive parameters. Through model reduction, the number of parameters in the model was reduced to 10 without any increase in model error. It may be concluded that those parameters removed during the reduction process have little influence on BRB CPD capacity. Model 2 and Model 3 may be considered a PE-based model and a RF-based model, respectively. Looking at Optimal Model 2 and Optimal Model 3, it is apparent that Model 3 performs better, because it is more precise with fewer terms than Model 2; thus it may be said that RF distribution predictive parameters more aptly characterize the imposed deformation history than PE distribution parameters. Model 4a and Model 4b contain only brace property predictive parameters (and no information about the imposed deformation histories). They performed very poorly, which indicates that predictive parameters that describe the imposed deformation history are clearly important in predicting the CPD capacity.

In Model 5, the brace property and RF distribution parameters (those parameters found to be most important) were used in a nonlinear model form, which led to what appeared to be excellent results. Optimal Model 5 contains only 4 predictive parameters, and its distribution of $Z = C_{predict} / C_{measure}$ has a mean and COV of 1.02 and 0.03, respectively. The equation for Optimal Model 5 is given below

$$C = \varepsilon_{yc}^{-0.234} \mu_{\max}^{-0.037} N_{RF}^{1.00} \mu_{RF}^{0.992} \tag{4.5}$$

Since the performance of Optimal Model 5 is extraordinary, the details of its formulation were investigated closely. It was found that Optimal Model 5 is actually an ineffective model because it inadvertently contains the final CPD capacity from test results in its formulation, thus giving it the ability to very accurately predict the CPD capacity. Figure 4.7 explains how this happened. One RF cycle (as shown in Figure 4.8) produces CPD equal to 4 times the cycle amplitude. Thus the number of Rainflow cycles (N_{RF}) times the mean amplitude of the cycles (μ_{RF}) equals ¼ of the CPD capacity. Through the capacity modeling process, the values of the θ parameters that were the exponents of the terms ε_{yc} and $\mu_{\max}$ were calibrated such that $\varepsilon_{yc}^{\theta_6} \mu_{\max}^{\theta_{12}} \approx 4$. Thus when the two components of equation 4.5 are multiplied together, the result is a value very close to the CPD capacity for the majority of the BRB specimens.

Since Optimal Model 5 is ineffective, the best model (the smallest yet most accurate) identified from the capacity modeling process is Optimal Model 3, given by the following equation:

$$C = 33.61 \cdot \left(\mu_{pos}\right)_{\max} + 0.15 \cdot \left(\mu_{neg}\right)_{\max} + 23.96 \cdot N_{RF} - 758.6 \cdot \upsilon_{RF} \tag{4.6}$$

The COV of the distribution of Z for this model is 0.26, which may be considered average precision for use in practical engineering problems. While the model precision is acceptable, the coefficients in the model also are not all logical; the first two

coefficients are positive, and this indicates that increases in $(\mu_{pos})_{\max}$ and $(\mu_{neg})_{\max}$ result in increases in CPD capacity. It is not logical that increases in maximum ductility demand result in larger capacities. This occurs because of the nature of fitting the capacity model to the test results. Those braces with higher ductility demands also were tested to higher CPD capacities, and this is reflected in the capacity model fit. The coefficient of υ_{RF}, however, is logical. It indicates that BRBs subjected to deformation histories characterized by a Rainflow distribution with high positive skew have lower CPD capacities than those with low skew. This is logical, as high skew values indicates that a few, large cycles were imposed to the BRB, whereas low skew indicates that the imposed cycles were more uniform. This behavior agrees with the observations of Carden [9] and Fahnestock [16].

4.6 End-Capacity Modeling Conclusions

In conclusion, through the process of parameter exploration, model creation, and model reduction using the MLE method techniques, it may be said that:

1) A variety of predictive parameters were explored. These include BRB material properties, BRB geometric properties, and parameters which characterize the imposed deformation histories. A limited number of parameters related to BRB geometric and material properties were explored because of the limited amount of information provided in the BRB test database. However, a wide range of deformation history predictive parameters were created and used, including parameters relating to ductility demands, CPD demands, plastic excursion counting, and Rainflow cycle counting.

2) Of the parameters investigated, it was found that deformation history predictive parameters were more important and contributed more substantially to model accuracy than BRB property parameters. Those models without deformation history predictive parameters (Model 4a and Model 4b) performed very poorly.

3) Although the Rainflow deformation history predictive parameters and the plastic excursion predictive parameters attempt to characterize the same behavior (size and shape of the imposed plastic deformation demand distribution), the Rainflow parameters were found to perform better than the plastic excursion parameters.

4) Overall, no high-fidelity model capable of predicting the end-CPD capacity of BRBs was found. The best model that behaved correctly was identified as Optimal Model 3, which had a COV of 0.26. Optimal Model 5, while very precise, was determined to be ineffective because of the issues discussed in Section 4.5. Perhaps given more information about the BRBs themselves (such as ultimate strains, etc.), more accurate models could be formulated.

5) When using deformation history predictive parameters, the end-capacity model may lead to counter-intuitive results that are artifacts of the distribution of the parameters in the test database and are not representative of behavior. For

example, it is thought that those BRBs subjected to higher ultimate demands, i.e. higher μ_{max}, should have relatively lower CPD capacity. However, the capacity model, as formulated in terms of predicting end capacity, indicates that larger ultimate demands cause larger CPD capacity. This appears to occur because those specimens with larger ultimate demands simply tended to be tested to higher CPD capacities, but this in general does not mean that higher ultimate demands lead to relatively higher CPD capacities.

6) It is possible to error, with the end-capacity formulation, and include in the predictive terms the value that the model seeks to predict. This occurred in Optimal Model 5 as explained in Section 4.5.

4.7 Chapter 4 Figures

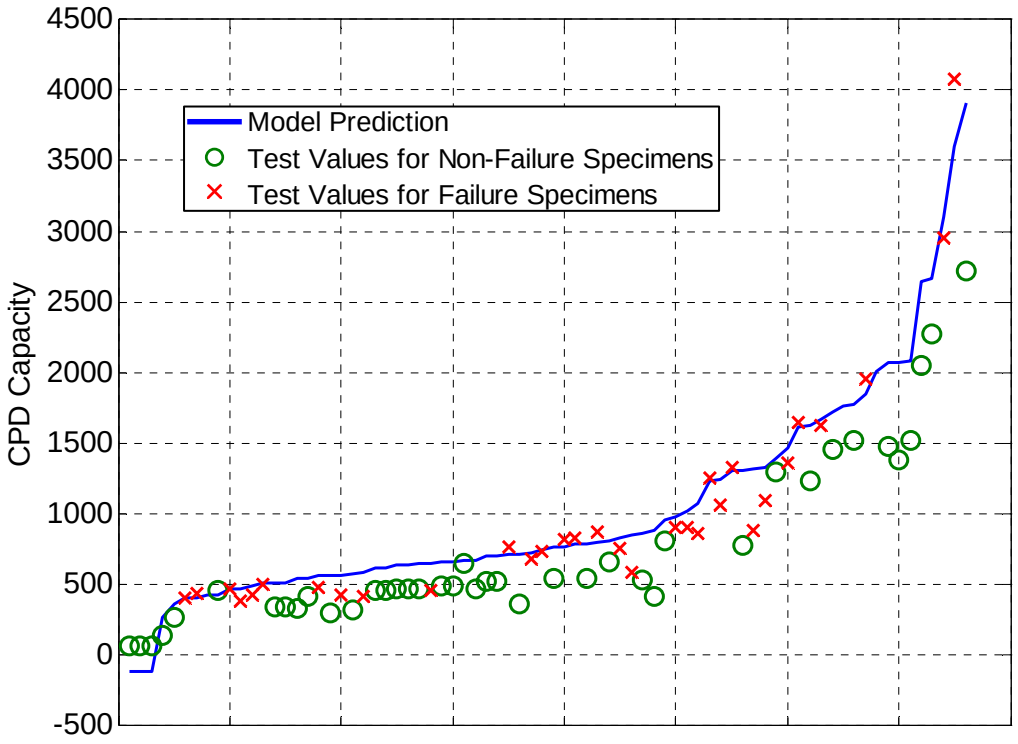

Figure 4.1: Comparison between Model and Test Results for Optimal Model 1

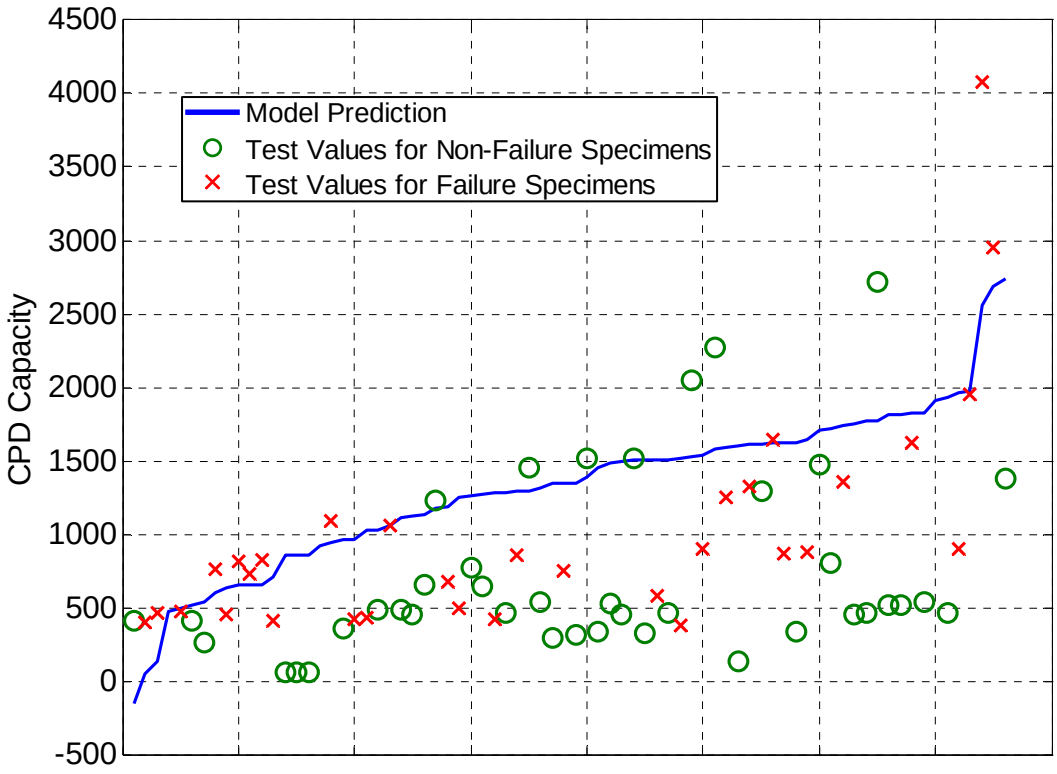

Figure 4.2: Comparison between Model and Test Results for Optimal Model 2

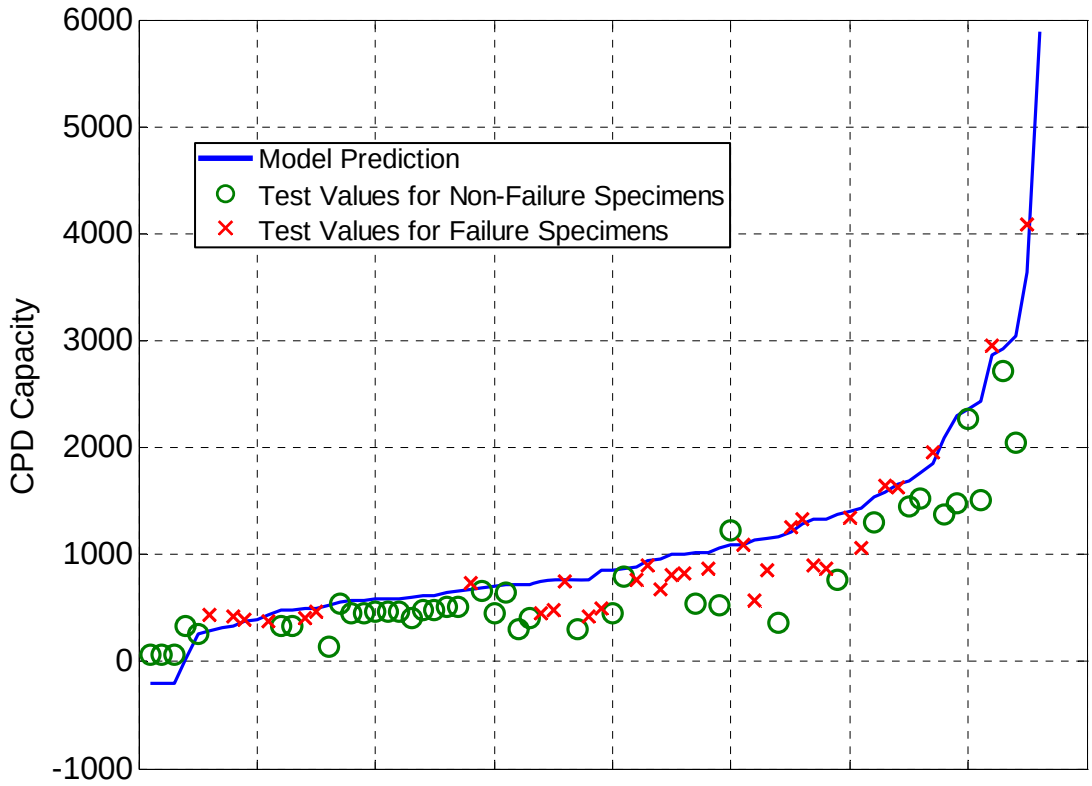

Figure 4.3: Comparison between Model and Test Results for Optimal Model 3

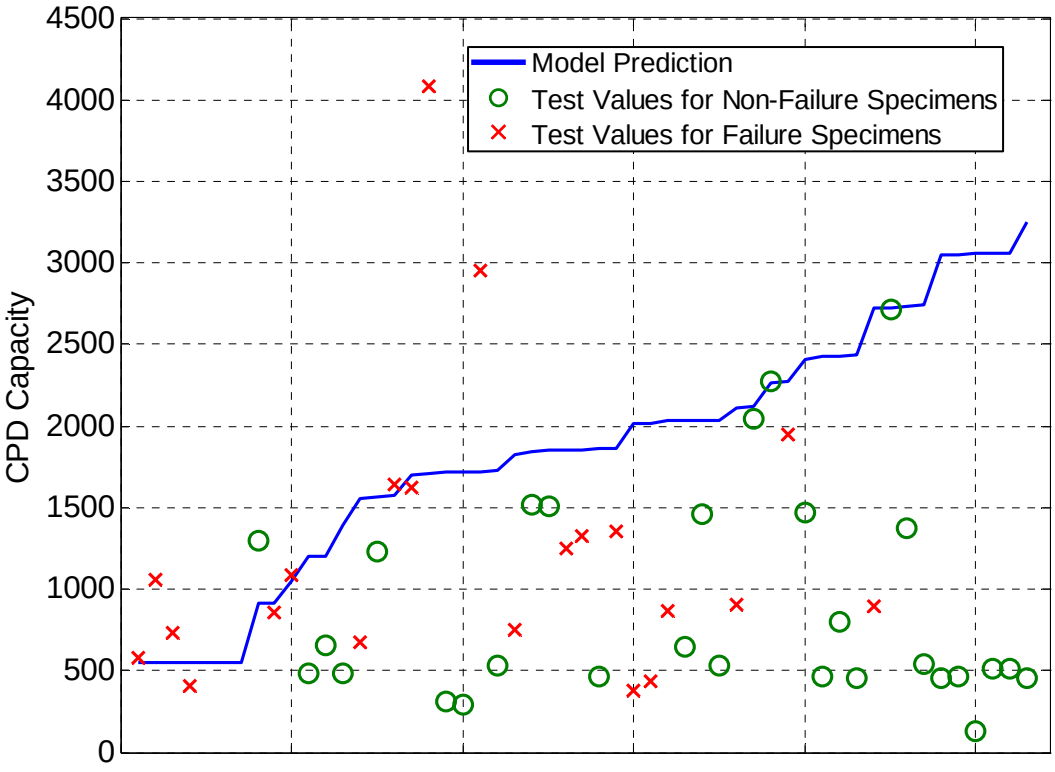

Figure 4.4: Comparison between Model and Test Results for Model 4a

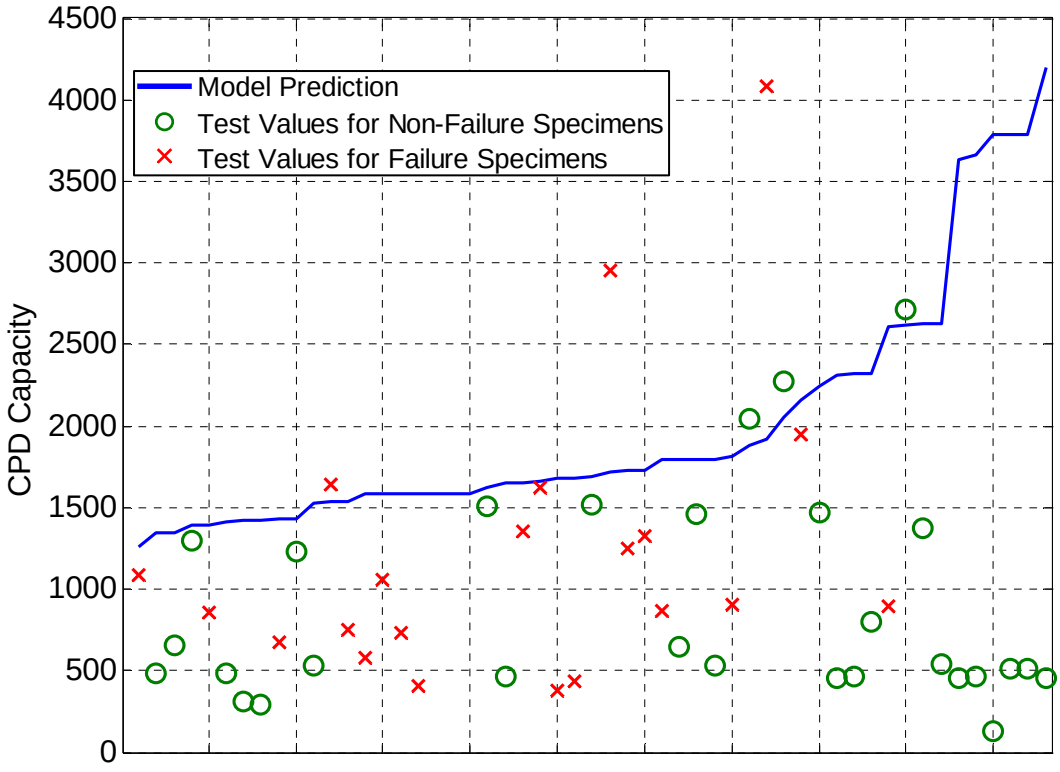

Figure 4.5: Comparison between Model and Test Results for Model 4b

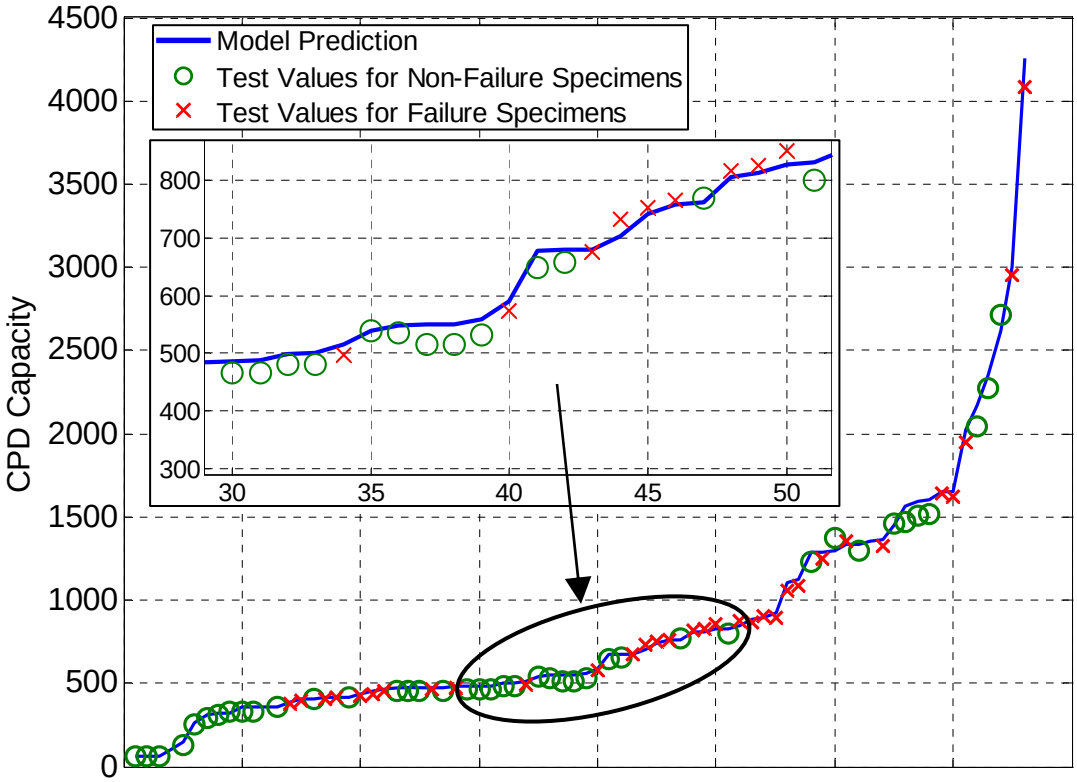

Figure 4.6: Comparison between Model and Test Results for Optimal Model 5

$$C = \varepsilon_{yc}^{-0.234} \mu_{\max}^{-0.037} N_{RF}^{1.00} \mu_{RF}^{0.992}$$

≈ 4
For all BRBs in the database

$$\approx N_{RF} \mu_{RF} = \frac{\mu_c}{4}$$

Figure 4.7: Explanation for Optimal Model 5

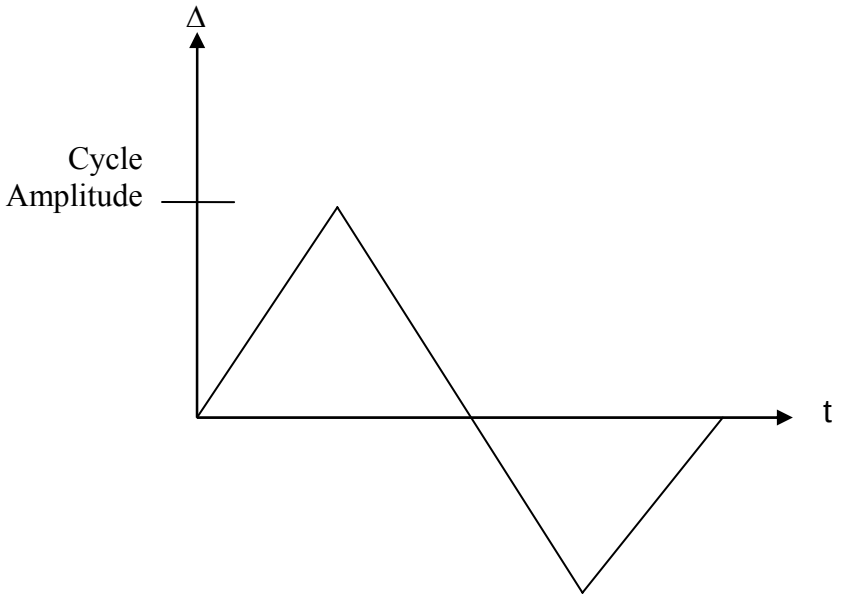

Figure 4.8: One Rainflow Cycle

4.8 Chapter 4 Tables

Table 4.1: End-Capacity Modeling Results

Model	$\gamma(\theta,\mathbf{h})$	Full Model				Optimal Model		
		h	n_h	μ_Z	COV_Z	n_h	μ_Z	COV_Z
1	$\gamma = \sum_{i=1}^{n_h} h_i \theta_i$	1,3-6,10-11,25-34,40,41,43,44,50,51,53,54	25	1.11	0.17	10	1.10	0.16
2	$\gamma = \sum_{i=1}^{n_h} h_i \theta_i$	1,3-6,10-11,40-43	11	1.14	0.22	8	1.49	0.56
3	$\gamma = \sum_{i=1}^{n_h} h_i \theta_i$	1,3-6,10,11,50,51,53,54	11	1.12	0.26	4	1.20	0.26
4a	$\gamma = \sum_{i=1}^{n_h} h_i \theta_i$	1,3-7	6	1.74	0.75			
4b	$\gamma = \prod_{i=1}^{n_h} h_i^{\theta_i}$	1,3-7	6	1.95	0.57			
5	$\gamma = \prod_{i=1}^{n_h} h_i^{\theta_i}$	2-4,6,7,12,50-53	11	1.01	0.02	4	1.02	0.03

Table 4.2: End Capacity Optimal Model 1 Equation and Model Error

$\gamma = \sum_{i=1}^{n_h} h_i \theta_i$	$\sigma =$ 158.5									
i	3	26	28	29	30	32	40	41	44	54
θ_i	136.7	2.120	5.792	-7.720	-1.463	1.637	15.73	44.07	-261.9	-355.8

Table 4.3: End Capacity Optimal Model 2 Equation and Model Error

$\gamma = \sum_{i=1}^{n_h} h_i \theta_i$	$\sigma =$ 581.8							
i	1	3	4	5	6	10	11	41
θ_i	85.92	101.4	124.6	106.9	0.153	34.91	46.62	45.80

Table 4.4: End Capacity Optimal Model 3 Equation and Model Error

$\gamma = \sum_{i=1}^{n_h} h_i \theta_i$	$\sigma =$ 242.7			
i	10	11	50	53
θ_i	33.61	0.1508	23.96	-758.6

Table 4.5: End Capacity Model 4a Equation and Model Error

$\gamma = \sum_{i=1}^{n_h} h_i \theta_i$	$\sigma =$ 1041					
i	1	3	4	5	6	7
θ_i	39.09	16.82	22.17	265.0	1.056	59.56

Table 4.6: End Capacity Model 4b Equation and Model Error

$\gamma = \prod_{i=1}^{n_h} h_i^{\theta_i}$	$\sigma =$ 1004					
i	1	3	4	5	6	7
θ_i	0	0.5528	0.0201	3.2549	-1.085	0.2895

Table 4.7: End Capacity Optimal Model 5 Equation and Model Error

$\gamma = \prod_{i=1}^{n_h} h_i^{\theta_i}$			$\sigma =$	22.18
i	6	12	50	51
θ_i	-0.234	-0.037	1.00	0.992

Chapter 5

BRB DAMAGE MODELS

5.1 Basic Damage Model

As noted previously, prior research identified the influence that large maximum ductility demands may have on the CPD capacity of BRBs. To investigate this from a different perspective, a damage model based on that created by Park and Ang [24] was considered.

The Park and Ang damage index is defined as

$$D = \frac{\delta_M}{\delta_u} + \frac{\beta_{PA}}{Q_y \delta_u} \int dE \tag{5.1}$$

where δ_M is the maximum deformation that occurs due to seismic loading; δ_u is the ultimate deformation capacity when subjected to a monotonic loading; Q_y is the yield strength; $\int dE$ is the total absorbed hysteric energy, and β_{PA} is a non-negative term that serves as a model parameter. With the assumption of elastic-plastic force-deformation response, this can be re-written for a BRB as

$$D = \frac{1}{\mu_{ult}} [\mu_{\max} + \beta_D \mu_c] \tag{5.2}$$

where *D* is the damage index, for which a value equal to one corresponds to failure, and values less than one indicate non-failure. The damage index may be computed at any point in a loading history (not necessarily at the failure point only). μ_{ult} is the ultimate ductility capacity, which is assumed to be equal to the value of ductility at the ultimate tensile strain of the steel. This is given by $\mu_{ult} = \varepsilon_{uc} / \varepsilon_{yc}$, where ε_{uc} is the ultimate tensile strain of the core, assumed to be 35% for all specimens; $\mu_{\max}$ is the value of maximum ductility demand (defined earlier) up to the point in the deformation history at which the damage index is determined; μ_c is the CPD at the point in the deformation history at which the damage index is determined; and β_D is a deterministic model parameter that controls the relative amount of damage attributed to maximum deformation versus cumulative deformation.

In this research, a damage model for BRBs was developed by finding the value of β_D in equation 5.2 that sets the mean value of the distribution of *D* for all BRB failure specimens at the end of their deformation histories (the point of failure) to be 1. This yielded $\beta_D = 0.23$. Using this value of β_D in equation 5.2, the distribution of D at the end of the deformation histories for all failure specimens was constructed. It is shown in

Figure 5.1. The mean value of the D distribution is indeed 1, as the value of β_D was calibrated based upon this fact. The COV of the D distribution is 0.61, with minimum and maximum distribution values of 0.36 and 3.1, respectively. The damage index distribution for non-failure specimens at the end of their histories is shown in Figure 5.2. Here the mean of the distribution is 0.81, much less than one, as expected, because the specimens did not fail, and the COV is 0.84. As the COV of the failure and non-failure specimen damage index distributions indicate, the basic damage model is relatively imprecise.

5.2 Augmented Damage Model

To improve the performance of the basic damage model given by equation 5.2, it was augmented with the capacity models presented in Chapter 4. The basic form of the augmented model was

$$D = \frac{1}{\mu_{ult}}[\mu_{\max} + \beta_D \mu_c] \times \gamma(\boldsymbol{\theta}, \mathbf{h}) + \sigma\varepsilon \tag{5.3}$$

where, as before, $\gamma(\boldsymbol{\theta}, \mathbf{h})$ is the capacity model form, and $\sigma\varepsilon$ constitutes the model error. Capacity model fitting utilizing the MLE method was used to determine the model parameters $\boldsymbol{\theta}$ and σ as described previously, where, in this case, the likelihood function was constructed to be proportional to probability that, at the end of their deformation histories, $D = 1$ for all failure specimens and $D < 1$ for all non-failure specimens. Thus the likelihood function is given as

$$L(\boldsymbol{\theta}, \sigma) \propto \prod_{\text{failure data}} \frac{1}{\sigma} \varphi\left(\frac{1-D}{\sigma}\right) \times \prod_{\text{non-failure data}} \Phi\left(\frac{1-D}{\sigma}\right) \tag{5.4}$$

where, as before, $\varphi(\cdot)$ and $\Phi(\cdot)$, respectively, denote the probability density function and cumulative distribution function of the standard normal distribution.

The first capacity model form used was that of Optimal Model 5. While Optimal Model 5 is flawed, as discussed in Section 4.5, it was used to test the concept of damage model augmentation. MLE method parameter estimation was performed, and the final predictive damage model is given by

$$D = \frac{1}{\mu_{ult}}[\mu_{\max} + 0.23\mu_c] \times \left[\varepsilon_{yc}^{\ -0.735} \mu_{\max}^{\ -0.049} N_{RF}^{\ -0.863} \mu_{RF}^{\ -0.851}\right] \tag{5.5}$$

The damage index distributions for specimens at the end of their deformation histories are plotted in Figure 5.3 and Figure 5.4, where the former portrays the distribution for failure specimens, and the latter portrays the distribution for non-failure specimens. The augmented damage model damage index distribution for all *failure* specimens has a mean and COV of 0.97 and 0.04, respectively, and the damage index distribution for the *non-failure* specimens has a mean and COV of 0.96 and 0.06, respectively. As expected, the precision of the augmented damage model is high, due to the spurious reasons described in Section 4.5. Thus, it may be concluded that the concept

of damage model augmentation and parameter estimation is sound, though certainly Optimal Model 5 cannot be used for the augmentation.

Other capacity model forms, including those shown in Table 4.1, were investigated. Unfortunately, during this investigation process, it was determined that the behavior over time of the augmented damage model was incorrect. To portray this, consider the value of the damage index from the damage model augmented with Optimal Model 5 versus deformation increment. This is shown, for BRB specimen ID 1, in Figure 5.5. The top portion of Figure 5.5 shows the value of the augmentation (i.e. $\left[\varepsilon_{yc}^{-0.735}\mu_{\max}^{-0.049}N_{RF}^{-0.863}\mu_{RF}^{-0.851}\right]$) as a function of deformation increment (or time); the bottom portion shows the value of the complete augmented damage model and the basic damage model versus deformation increment. The basic damage model behaves correctly, increasing monotonically from a value of zero at the beginning of the history to a value of approximately 0.6 at the end of the history. Unfortunately, the behavior of the complete augmented damage model versus deformation increment is incorrect, decreasing from infinity at the beginning of the history, when in fact it should be increasing monotonically.

To solve this problem, augmented damage model forms other than that given by equation 5.3 were investigated. This process lead to the development of remaining capacity (RC) models, which appear to solve the behavior-over-time problem. Because of this, further damage model investigation was not performed; instead, RC models were developed, as described in Chapter 6.

5.3 Damage Modeling Conclusions

In general, the basic damage model described in Section 5.1 behaves well, increasing monotonically from zero at the beginning of each history; however, it does not predict the damage index values at the ends of deformation histories precisely. The basic damage model, while imprecise, may be applied in an engineering design context, given that its behavior is correct, so long as its poor precision is taken into account when using it. Augmentation of the damage models, while increasing their precision, causes the damage index behavior over time to be incorrect – it does not increase monotonically from zero. While trying to solve this problem using augmented damage models, the concept of remaining capacity models was developed, and so further investigation regarding augmented damage models was not performed.

5.4 Chapter 5 Figures

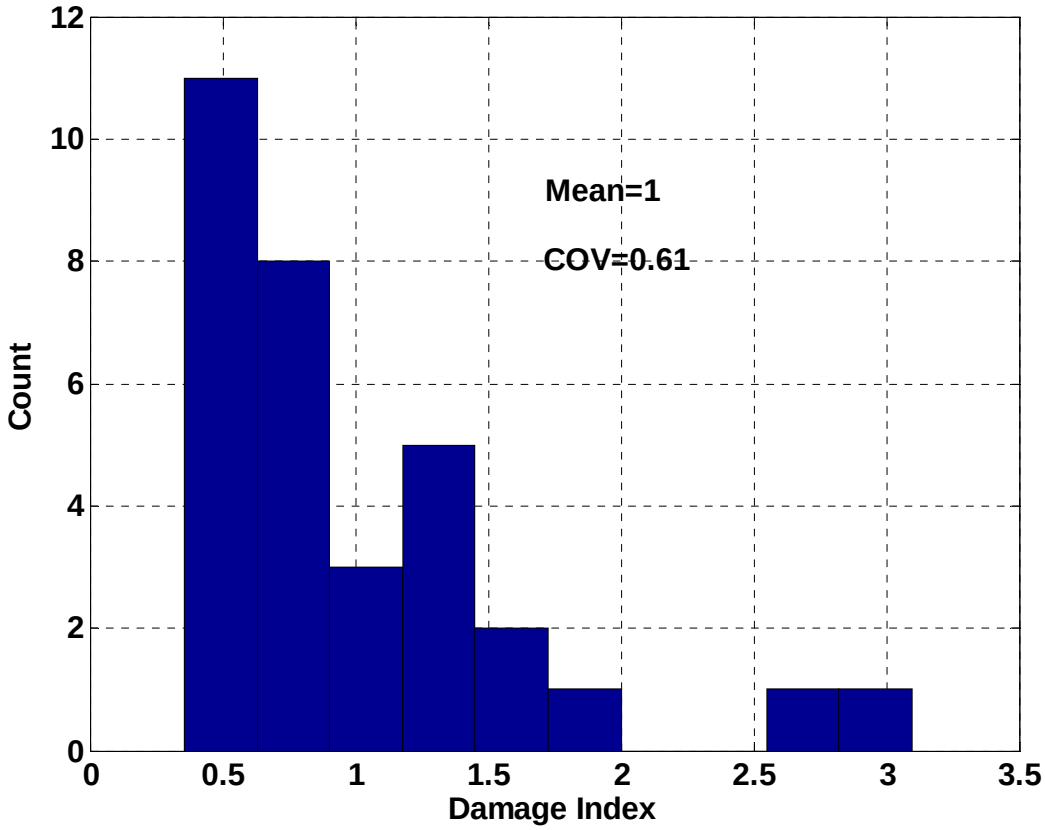

Figure 5.1: Basic Damage Model Damage Index Distribution of all Failure Specimens

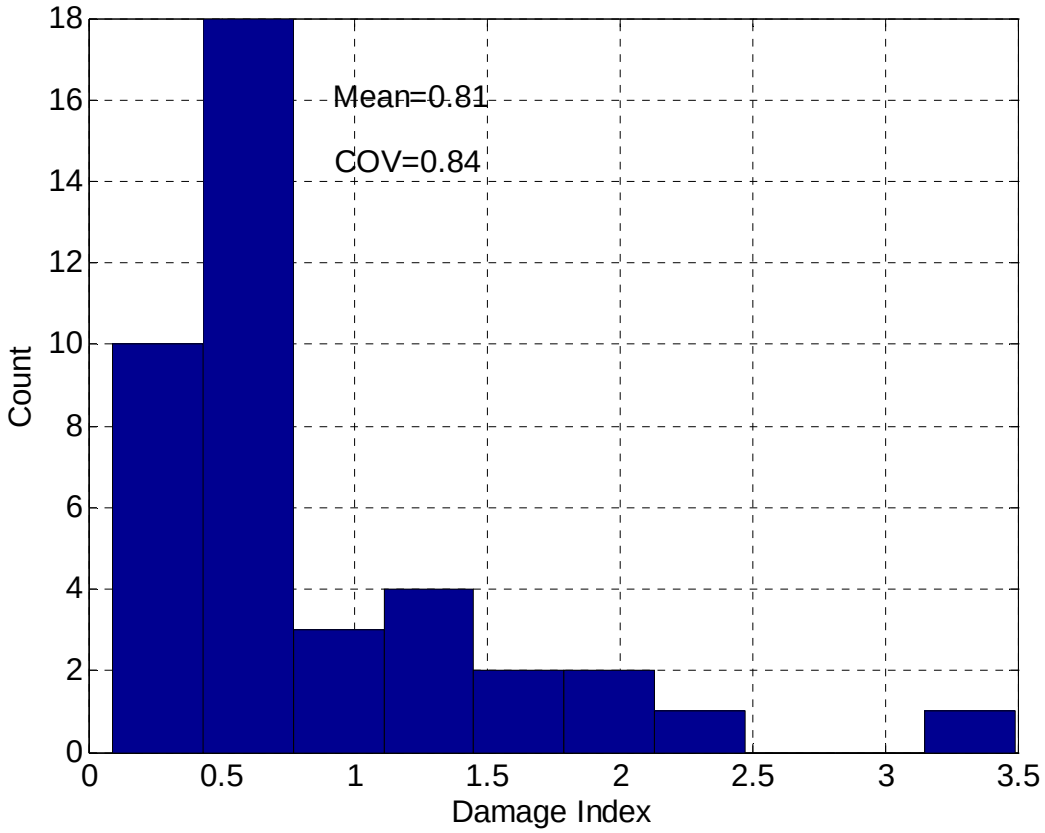

Figure 5.2: Basic Damage Model Damage Index Distribution for all Non-failure Specimens

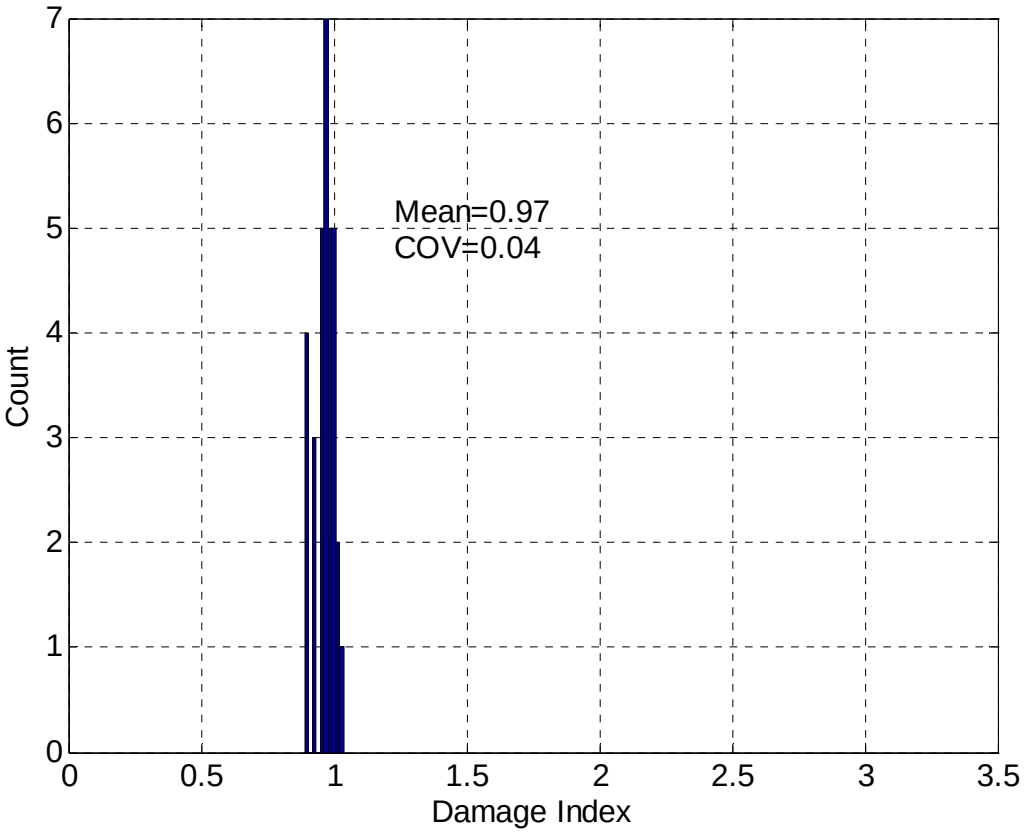

Figure 5.3: Augmented Damage Model Damage Index Distribution for all Failure Specimens

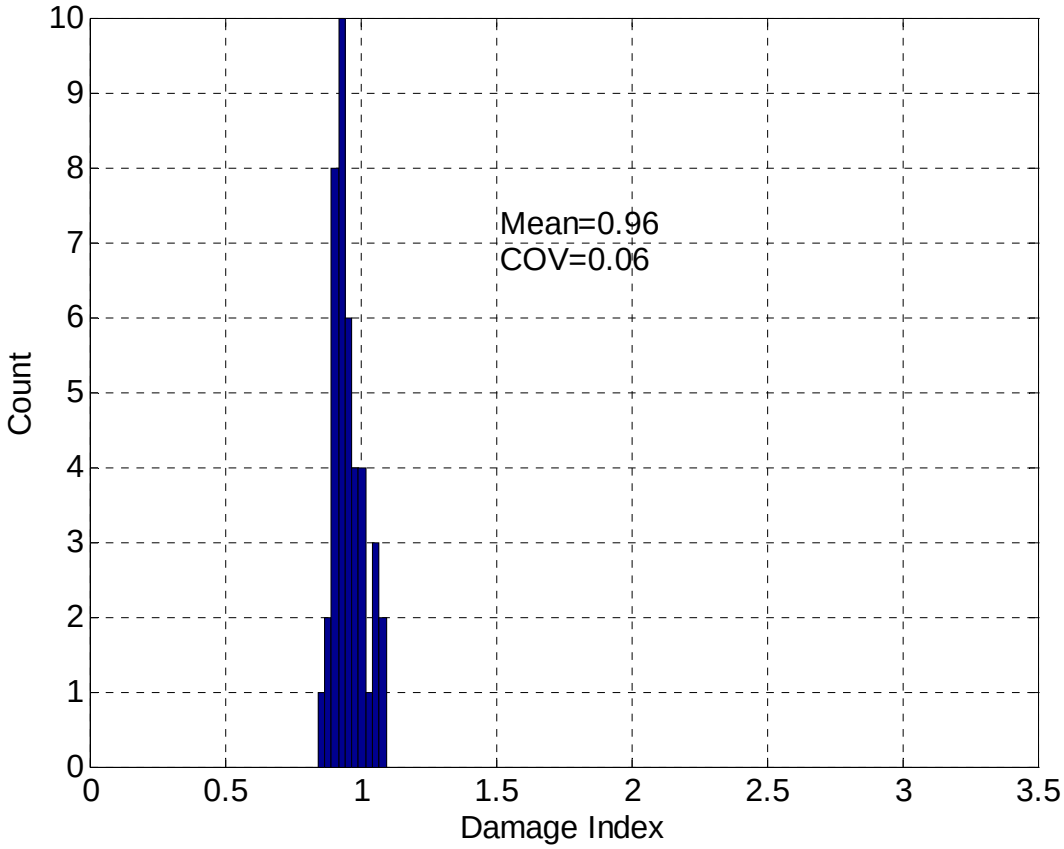

Figure 5.4: Augmented Damage Model Damage Index Distribution for all Non-failure Specimens

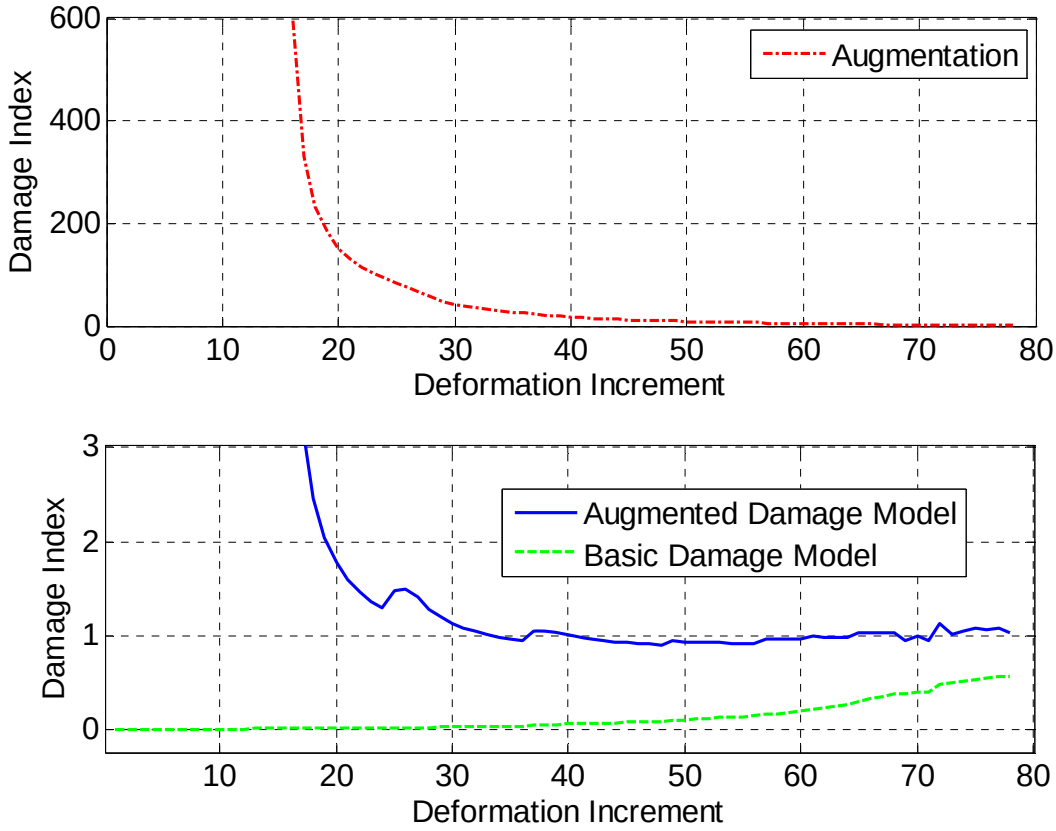

Figure 5.5: Damage Index Plot versus Deformation Increment for BRB Specimen 1

Chapter 6

REMAINING CAPACITY MODELS

6.1 Formulation

In an attempt to overcome the disadvantages of the end-capacity and damage models described above, remaining capacity models were developed. The basic form of the remaining capacity models is given by

$$RC = TC - UC \tag{6.1}$$

where RC is the remaining capacity; TC is the total capacity (the capacity of the brace in an undamaged state); and UC is the used capacity (all in terms of CPD). TC may be thought of as the total amount of damage that the brace may absorb without failure. It does not vary with time or the applied deformation history. By contrast, UC is the amount of damage absorbed (or capacity utilized); it varies with the applied deformation history. Thus RC varies with the applied deformation history, from a value of TC at the beginning of the applied deformation history to a value of 0 when the brace fractures.

To solve the fundamental problem of the augmented damage models (i.e. the behavior-over-time problem), the form of the predictive parameters and model parameters used to construct the TC and UC terms were calibrated such that the RC model decreased monotonically with the imposed deformation history. The basic RC model form is as follows:

$$RC = TC - UC = \prod h_i^{\theta_i} - \sum h_j \theta_j \tag{6.2}$$

The form of equation 6.2 is a combination of the end-capacity models and damage models. The total capacity component, i.e. $TC = \prod h_i^{\theta_i}$, is an end-capacity-type formulation that utilizes only static predictive parameters (those that do not change with the imposed deformation). Conversely, the used capacity component, i.e. $UC = \sum h_j \theta_j$, is a damage-evolution-type model and utilizes deformation history predictive parameters (those that vary with the imposed deformation). Values of the model parameters θ_j in the UC component are restricted to ensure that UC increases monotonically, such that RC decreases monotonically.

The subset of predictive parameters described in Chapter 3 that was identified as most informative (as discussed in Section 4.6) was considered for use in the RC model. The parameters are listed in Table 6.1.

All parameters listed in Table 6.1 are described in Chapter 3 except for μ_{ult} and $\mu_{\max loc}$. μ_{ult} is described in Section 5.1, and $\mu_{\max loc}$ is defined as $\mu_{\max loc} = \frac{\mu_c @ \mu_{\max}}{\mu_c @ end}$, i.e.

the value of μ_c that occurs at the location of $\mu_{\max}$ divided by the value of μ_c at the end of the deformation history. Thus $\mu_{\max loc}$ may be thought of as the relative location of the maximum ductility demand in the deformation history in terms of CPD. This parameter was created to potentially characterize the effects of the location of maximum ductility demands on the CPD capacity.

6.2 Model Fitting

The MLE method, as outlined in Chapter 4, was used to calibrate the model parameters using the complete model form:

$$RC = TC - UC = \prod h_i^{\theta_i} - \sum h_j \theta_j + \sigma\varepsilon \tag{6.3}$$

As before, the model parameters $\boldsymbol{\theta}$ and σ were calibrated to maximize the likelihood function, which, for the remaining capacity models, is given by

$$L(\boldsymbol{\theta},\sigma) \propto \prod_{i=1}^{n_{specimens}} \left\{ \prod_{j=1}^{n_{increments}} P\left[\left(RC_{predict}\right)_{i,j} = \left(RC_{measure}\right)_{i,j} \right] \right\} \tag{6.4}$$

in which $\left(RC_{predict}\right)_{i,j}$ is the predicted remaining capacity given by equation 6.2 for BRB specimen *i* at deformation increment *j*; similarly, $\left(RC_{measure}\right)_{i,j}$ is the measured remaining capacity from testing for BRB specimen *i* at deformation increment *j*, which is given as

$$\left(RC_{measure}\right)_{i,j} = \left(\mu_c\right)_{i,end} - \left(\mu_c\right)_{i,j} \tag{6.5}$$

where $\left(\mu_c\right)_{i,end}$ is the CPD demand from testing for BRB specimen *i* at the end of testing, i.e. the total CPD demand, and $\left(\mu_c\right)_{i,j}$ is the CPD demand from testing for BRB specimen *i* at deformation increment *j*, i.e. all plastic deformation (in terms of ductility) accumulated from the start of the imposed deformation history up to point *j*.

The likelihood function was calculated only for failure specimens that also had ultimate tensile stress data available; thus $n_{specimens} = 21$. In addition, the number of increments used in the MLE method was 9, i.e. $n_{increments} = 9$. These increments were chosen such that they were spaced evenly in the domain of remaining capacity (i.e. when plotting RC on the y-axis versus CPD on the x-axis, the increments were spaced evenly on the y-axis but not uniformly on the x-axis). As a result, the likelihood function was constructed such that it was maximized when the predicted remaining capacity matches the measured remaining capacity at 9 points along the deformation history, beginning and end points inclusive.

6.3 Model Precision Quantification

Since the *RC* models were fit to test data at various intervals in the deformation histories (and not just at the beginning and/or end points), it was very difficult to quantify

the overall model precision. The metric used to do this was the distribution of $\left(RC_{predict}\right)_{failure,end}$, which is the distribution of predicted remaining capacities at the end of the imposed deformation histories for failure specimens. The mean of this distribution is denoted by $\mu_{RCpredict}$ and measures the model accuracy; the standard deviation of the distribution is denoted by $\sigma_{RCpredict}$ and measures the model precision. Similar metrics could be derived for different points in the deformation history, but the distribution at the end of the history is most informative.

6.4 Remaining Capacity Model Results

Various RC models were investigated that included the terms in Table 6.1 in a variety of combinations. Through trial and error, two best models were identified, RC 1 and RC 2. Modeling results are presented in Table 6.2 and Table 6.3, which list, for each model, the equation for predicted RC, values of σ, model accuracy, and model precision.

Figure 6.1 and Figure 6.3 show the comparison of the predicted remaining capacity versus the measured remaining capacity over the entire deformation histories as predicted by model RC1 and RC2, respectively. The figures include predicted capacities for both failure and non-failure specimens, and only BRBs with $\frac{F_u}{F_y}$ data are included. In the figure, the measured remaining capacity is represented by the mean plus and minus one standard deviation envelope of the distribution of measured remaining capacities (for failure specimens only).

Figure 6.2 and Figure 6.4 show the distribution of predicted remaining capacities at the end of the deformation histories as predicted by RC1 and RC2, respectively. Again, the distribution includes only those specimens which failed and had $\frac{F_u}{F_y}$ data.

It is difficult to ascertain the model performance for a single BRB specimen from Figure 6.1 and Figure 6.3. Thus, in Figure 6.5 and Figure 6.6, the *best* and *worst* (as determined through visual inspection), respectively, comparison of predicted to remaining capacities is shown for RC 1. Similarly, Figure 6.7 and Figure 6.8 show the best and worst comparison, respectively, for RC 2. In general, the comparisons for most BRBs for both RC models were somewhere between the best and worst comparisons but tended toward the best (for plots for all specimens, see Appendix C).

The following conclusions apply to models RC 1 and RC 2:

1) For both models, the behavior of the predicted remaining capacity over the deformation history (i.e. the shape of the plots) is monotonically decreasing, which is good.

2) The majority of the predicted values fall within the measured distribution envelopes for both models.

3) The RC 1 model is more accurate and precise than RC 2, because $\mu_{RCpredict}$ is nearer to 0 for RC 1 than RC 2, and because $\sigma_{RCpredict}$ is smaller for RC 1 than RC 2.

4) RC-2, in general, overestimates remaining capacity, as $\mu_{RCpredict}$ is significantly greater than 0.

5) Both models RC 1 and RC 2 are significantly more precise than the model RC Avg, which is a model based on quantifying the average brace remaining capacity and which uses no additional predictor terms. Thus, the use of RC models is warranted instead of using just the average brace capacity from tests.

While the behavior of the model seems logical, the values of some model parameters θ were further investigated: The model parameters associated with $\frac{A_c}{(A_c)_{\max}}$ and $\frac{L_c}{(L_c)_{\max}}$ are both positive, indicating that as the core length and area become larger, the CPD capacity of the BRB increases. This is logical, as larger BRBs should have higher capacity. In addition, the model parameter associated with the core area is larger than that associated with the core length, indicating that the area has a greater impact on CPD capacity than length. This is also logical, as CPD is deformation normalized by the core length, which probably limits the influence of the core length on capacity. The model parameters associated with the core yield strain are both negative, indicating that as the yield strain increases, CPD capacity decreases. As yield strain is proportional to the yield stress, this is logical, as BRBs with higher yield strength may tend to have lower ductility capacity. Finally, the model parameters associated with the ratio of ultimate to yield stress are of different signs for RC 1 and RC 2. RC 1 has a positive value, which means that as the ratio increases, the CPD capacity increases. This is logical, as braces with higher ratios of ultimate to yield stress tend to have higher ductility. Oddly, the coefficient for the RC 2 model is negative, indicating the opposite. Further discussion relating to TC parameters is presented in Section 11.3.4.

While RC 1 appears to be a better model than RC 2 in all respects, the inclusion of the $\mu_{\max loc}$ term in RC 1 presents problems. The overall effect of the $\mu_{\max loc}^{-0.9883}$ term is that BRBs subjected to seismic loading with relatively high early demands (a smaller value of $\mu_{\max loc}$) are predicted to have larger CPD capacity. Conversely, BRBs subjected to seismic loading with relatively late high demands (a larger value of $\mu_{\max loc}$) are predicted to have lower CPD capacity. This conflicts with the observations made by Carden [9] and Fahnestock [16], and causes issues with using the RC model in the PBEF framework (as discussed in Section 11.3.4). The negative value of the model parameter associated with $\mu_{\max loc}$ (i.e. its exponent) was determined by fitting the model to test data. Most BRB tests utilized a regular or irregular cyclic imposed deformation history, which is dissimilar to a simulated seismic imposed deformation history. The effects of these histories caused the fit to produce a negative model parameter. Actual BRB behavior, as

observed based on simulated seismic loadings, is likely much different than the behavior implied by the cyclic loading results.

In addition to the problem discussed above, there is another problem with the $\mu_{\max loc}$ term – it is dependent on the applied deformation, and is calculated based on knowing the entire deformation history. As other terms in the TC component of the RC model are not deformation-dependent and can be determined from BRB properties, $\mu_{\max loc}$ does not fit well in the TC component, and prevents TC from being calculated without knowing the applied deformation history.

To avoid the problems discussed above, the RC 2 model was developed without the use of the $\mu_{\max loc}$. While this model is less accurate and precise than the RC 1 model, it does behave correctly and produces reasonable results.

6.5 Remaining Capacity Model Conclusions

RC models were developed to solve the problems associated with the end-capacity and damage models developed previously. As such, they are a combination of the end-capacity and damage model formulations. A variety of model forms were investigated, and model parameters were calibrated by fitting to test data using the MLE method. Two best models, RC 1 and RC 2, were identified. While both models behave correctly (i.e. produce monotonically decreasing results), RC 1 is both more accurate and precise than RC 2; however, it has issues with its use due to the inclusion of the $\mu_{\max loc}$ term. In general, given the great variability in the types of BRBs and the loads imposed on them, and given the small number of BRBs available to which the model is fitted, these RC models do a good job of predicting the remaining capacity of the BRBs.

6.6 Chapter 6 Figures

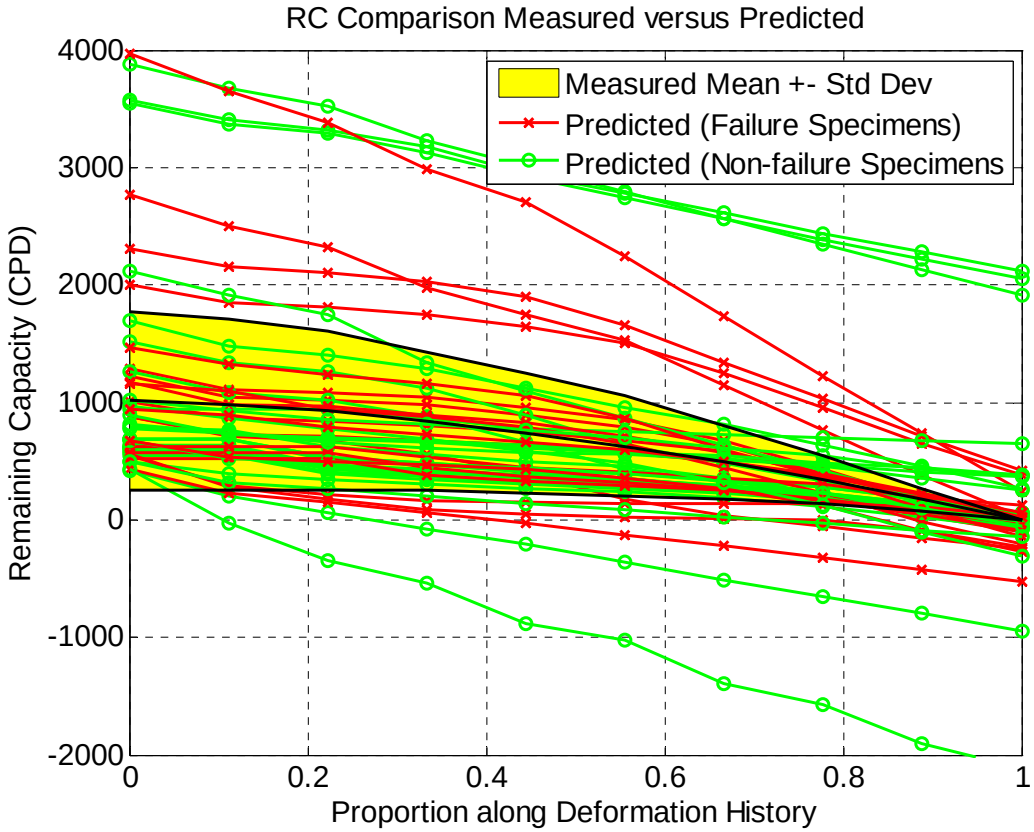

Figure 6.1: Predicted versus Measured RC Comparison for RC 1 Model

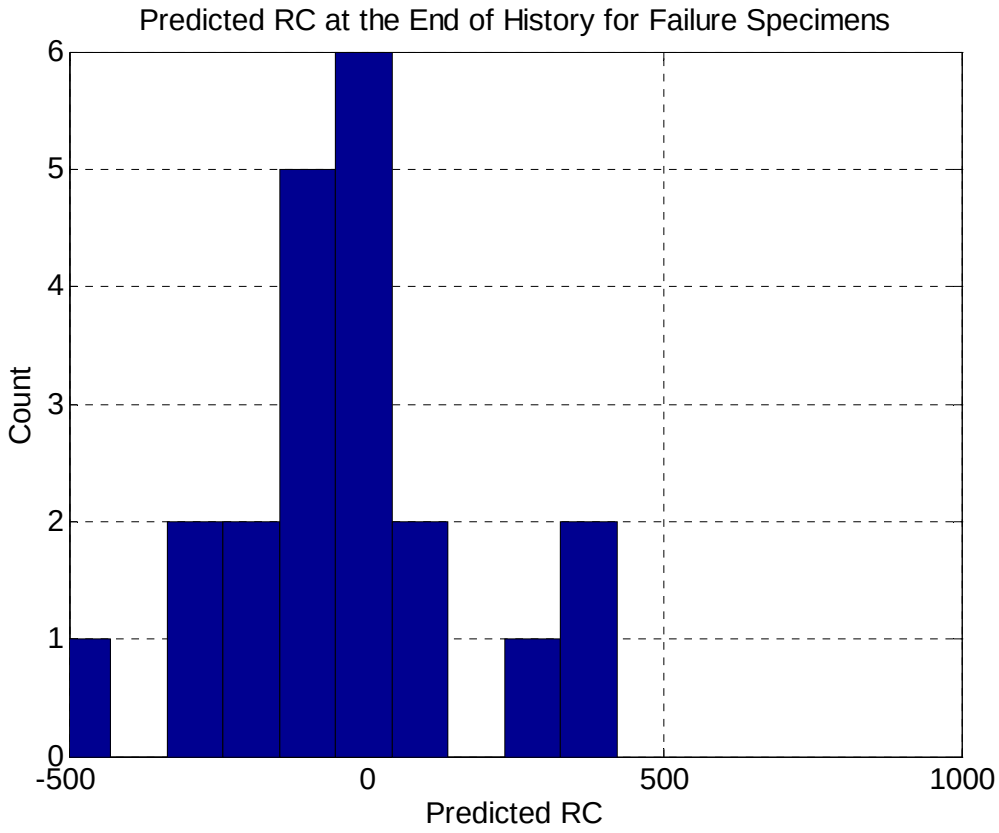

Figure 6.2: Predicted RC Distribution at End of History for RC 1 Model (Failure Specimens Only)

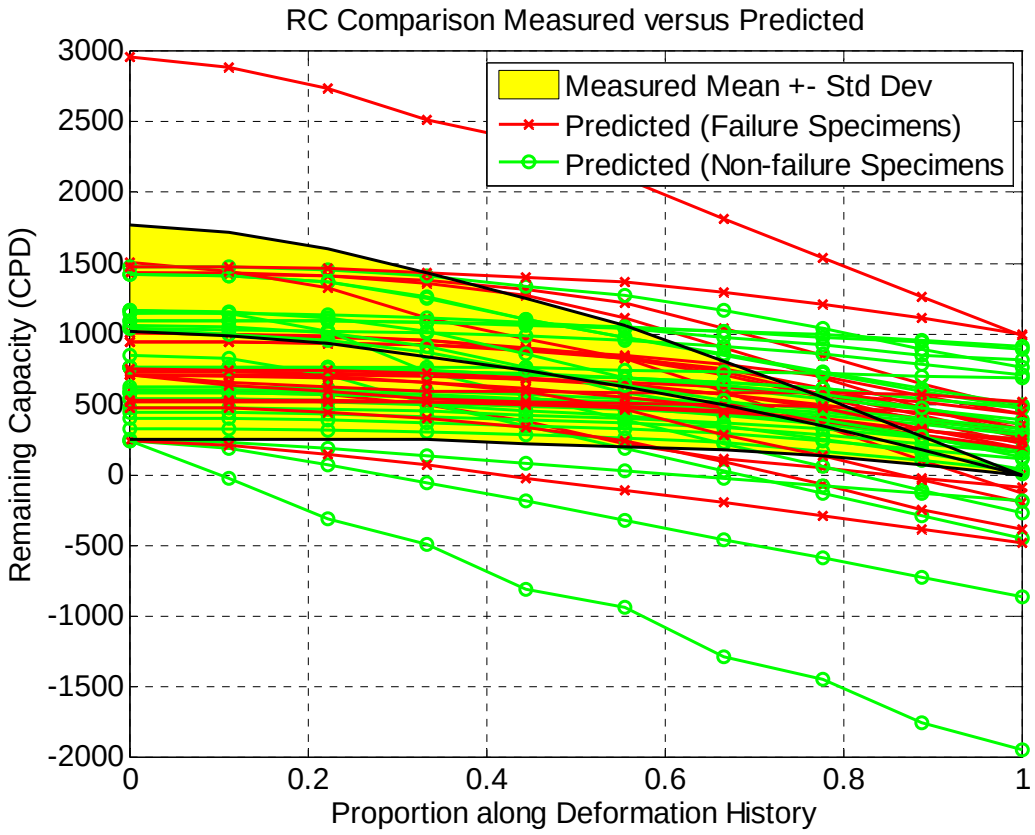

Figure 6.3: Predicted versus Measured RC Comparison for RC 2 Model

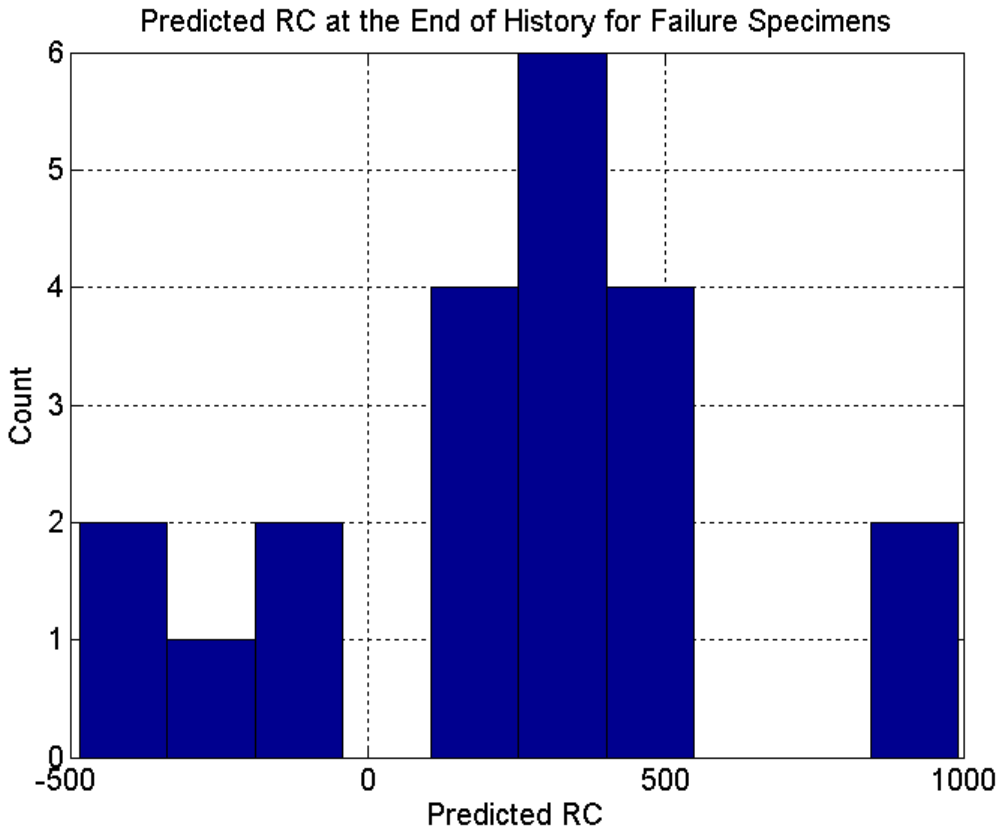

Figure 6.4: Predicted RC Distribution at End of History for RC 2 Model (Failure Specimens Only)

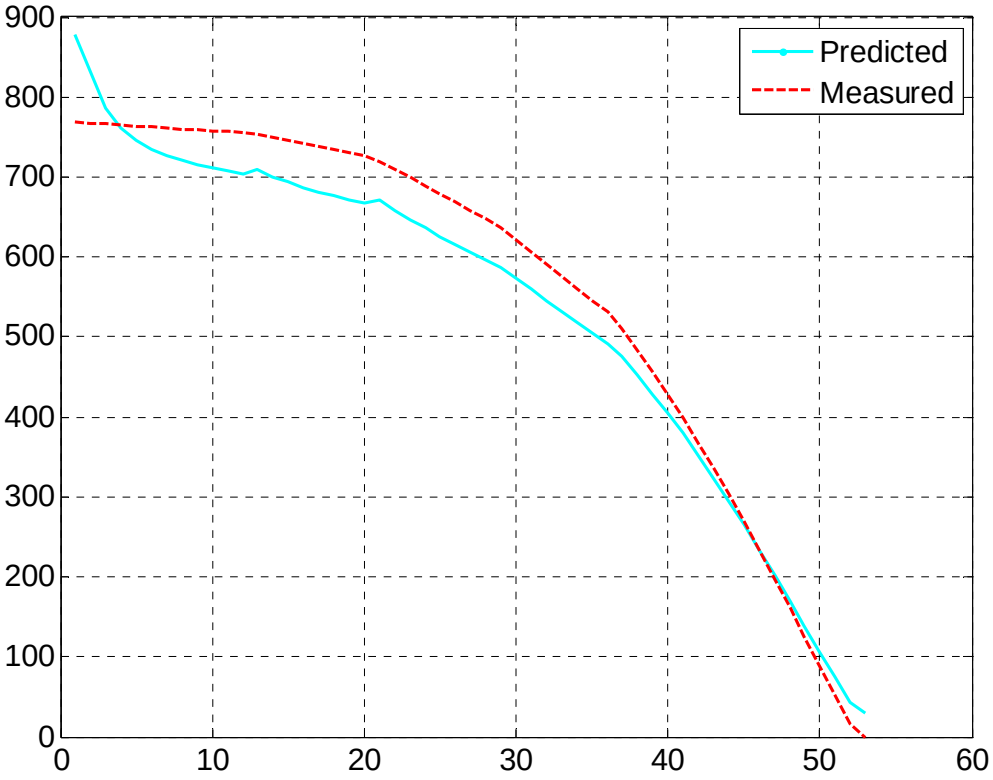

Figure 6.5: Best Remaining Capacity Comparison for RC 1

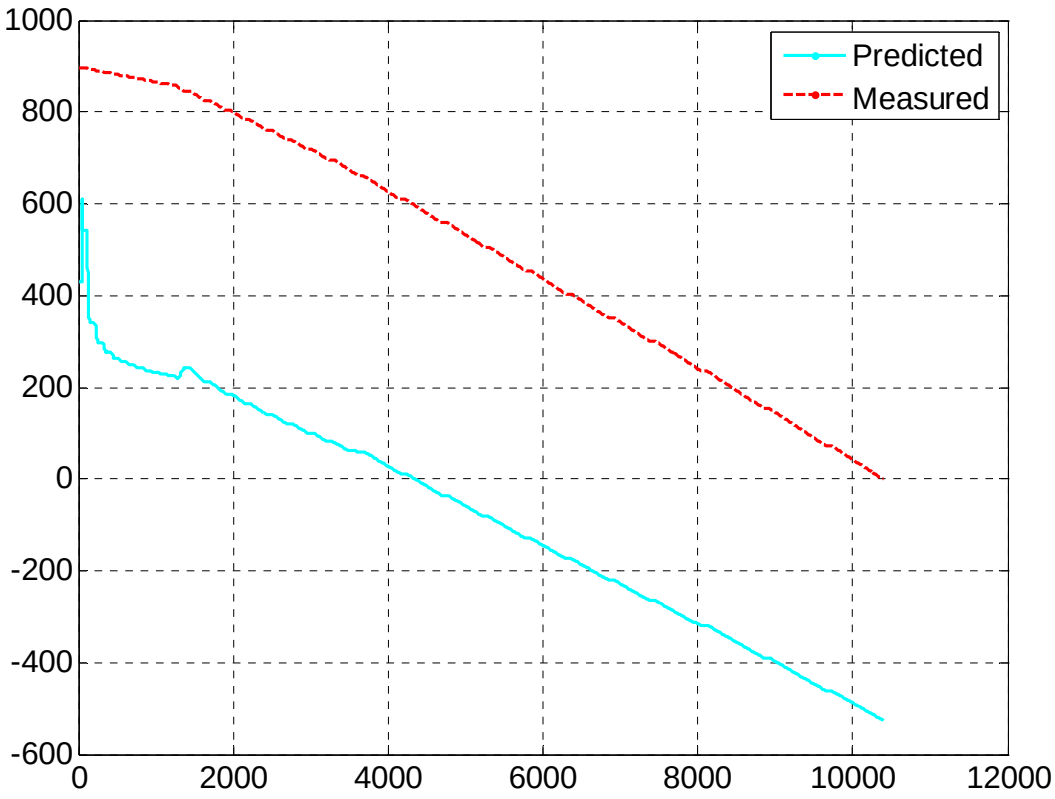

Figure 6.6: Worst Remaining Capacity Comparison for RC 1

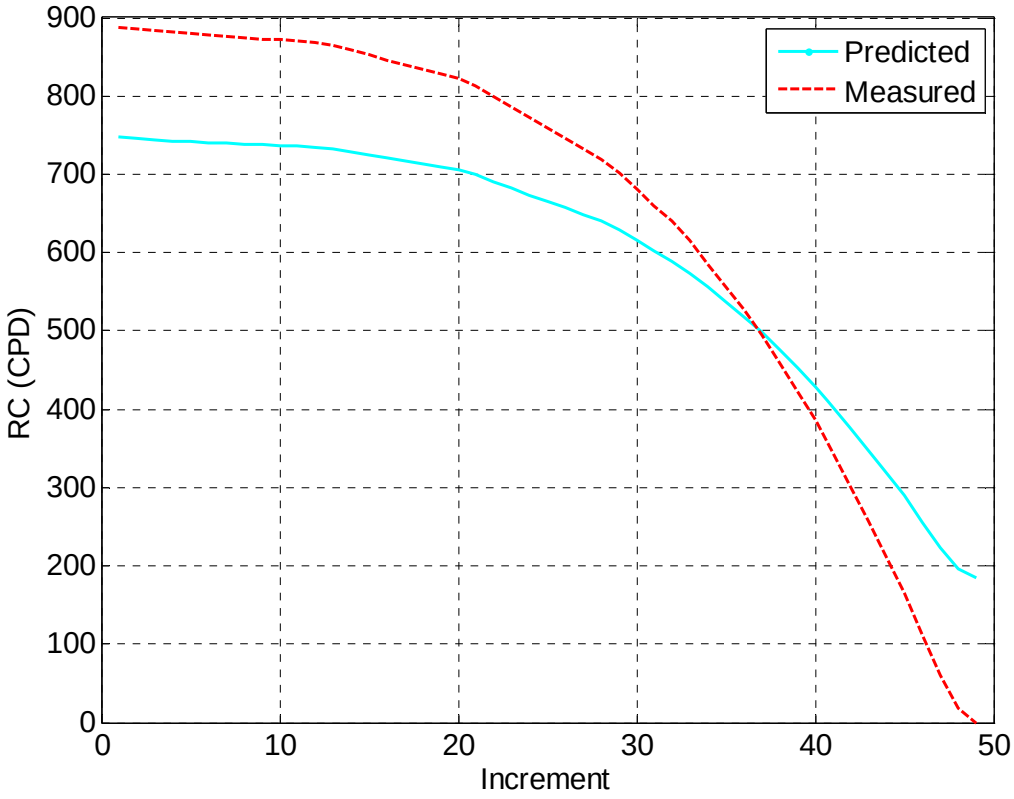

Figure 6.7: Best Remaining Capacity Comparison for RC 2

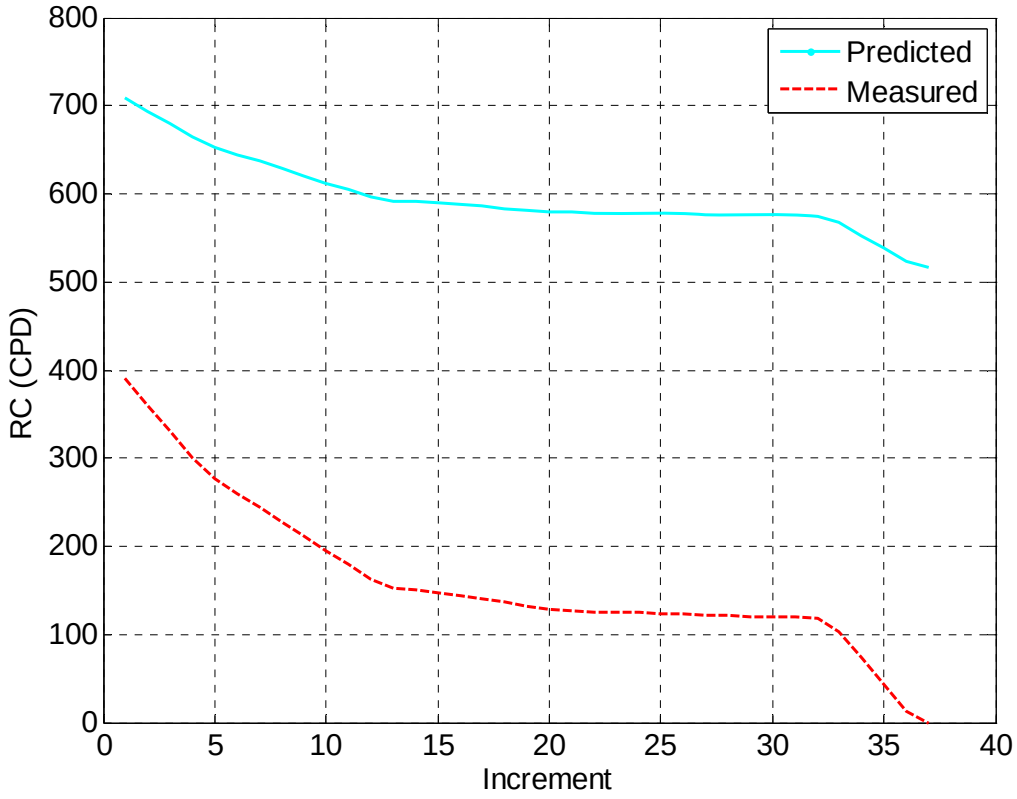

Figure 6.8: Worst Remaining Capacity Comparison for RC 2

6.7 Chapter 6 Tables

Table 6.1: Predictive Parameters Used in Remaining Capacity Models

TC **Component Terms**	*UC* **Component Terms**
$h_2 = 2$	$h_{12} = \mu_{\max}$
$h_3 = A_c / (A_c)_{\max}$	$h_{20} = \mu_c$
$h_4 = L_c / (L_c)_{\max}$	$h_{50} = N_{RF}$
$h_6 = \varepsilon_{yc}$	$h_{51} = \mu_{RF}$
$h_7 = F_u / F_y$	μ_{ult}
$\mu_{\max loc}$	

Table 6.2: Remaining Capacity Modeling Equations

Model	Equation
RC 1	$RC = 2^{-3.434} \cdot \left(\frac{A_c}{(A_c)_{\max}}\right)^{0.2019} \cdot \left(\frac{L_c}{(L_c)_{\max}}\right)^{0.0466} \cdot \varepsilon_{yc}^{-1.319} \cdot \left(\frac{F_u}{F_y}\right)^{0.2181} \cdot \mu_{\max loc}^{-0.9883}$ $-0.8677\mu_c + 185.8\frac{\mu_{\max}}{\mu_c}$
RC 2	$R = 2^{-21.20} \cdot \left(\frac{A_c}{(A_c)_{\max}}\right)^{0.425} \cdot \left(\frac{L_c}{(L_c)_{\max}}\right)^{0.044} \cdot \varepsilon_{yc}^{-3.45} \cdot \left(\frac{F_u}{F_y}\right)^{-1.46} -152.9\frac{\mu_c}{\mu_{ult}} - 1.12$
RC Avg	$R = 2^{10.27} - \mu_c$

Table 6.3: Remaining Capacity Modeling Accuracy and Precision

Model	Value of σ	$\mu_{RCpredict}$	$\sigma_{RCpredcit}$
RC 1	193	-30	217
RC 2	434	243	368
RC Avg	870	0	891

Chapter 7

PBEF INPUT MODULES

7.1 Overview

The origin of Analysis Path 1 (shown in Figure 1.4) is the input modules, the purpose of which are to create randomly-generated acceleration time histories (sequences of acceleration-time pairs) that will be applied as base acceleration values to the BRBF system model. Acceleration time histories are generated based on input power spectral density (PSD) functions. Two types of input PSD models were used in this research; the first utilized an input white noise (WN) PSD function, and acceleration histories were filtered using a Kanai-Tajimi filter before being applied to the BRBF model. The second was based on an input PSD calibrated such that the acceleration time histories produced resulted in a 5%-damped elastic spectrum that matched a target spectrum. For both input types, resulting acceleration time history values were multiplied by a modulation function to account for non-stationarity inherent in seismic loadings. Details of each formulation are presented in the following sections.

7.2 Input Module 1: Filtered White Noise

7.2.1 Overview

The analytical flow of Input Module 1 is illustrated in Figure 7.1. The steps of input generation are as follows:

1) A random acceleration time history $a_{base}(t)$ is generated based on a WN PSD.

2) The base acceleration time history is filtered using a Kanai-Tajimi filter; this is performed by using $a_{base}(t)$ as input acceleration values for a base-excited single-degree of freedom (SDOF) system; the resulting absolute acceleration of the SDOF system is $\left(\ddot{z}_g(t)\right)_{KT}$.

3) $\left(\ddot{z}_g(t)\right)_{KT}$ is multiplied in time by a modulating function $\Psi(t)$ to produce a non-stationary acceleration time history $\ddot{z}_g(t)$ that is used as input to the BRBF system model.

The components are described in detail in the following sections.

7.2.2 Step 1: Input WN PSD Function

The base PSD used in the WN PSD block is shown in Figure 7.2. The parameter Φ_0 is the value of the constant PSD and can be calibrated to produce varying levels of output acceleration.

Using the spectral representation method [36] one can generate stationary Gaussian random time histories that are compatible with a given PSD $\Phi(\varpi)$ by

$$a_{base}(t) = 2\sum_{i}^{n} \sqrt{\Phi(\varpi_i) \cdot \Delta\varpi} \cdot \cos(\varpi_i t + \theta_i) \tag{7.1}$$

where $a_{base}(t)$ is the randomly generated acceleration history; $\Phi(\varpi_i)$ is the value of the input acceleration PSD function at $\varpi = \varpi_i$; $\Delta\varpi = \varpi_{i+1} - \varpi_i$; and $\theta_i = U(0,2\pi)$ is a random phase angle that conforms to a uniform distribution bounded 0 to 2π. The vector of frequencies ϖ is chosen to cover the range of frequencies of interest. The algorithm for generating acceleration histories using equation 7.1 proceeds as follows:

1) For each value of *i*,
   a. generate θ_i using a random number generator;
   b. select ϖ_i from the vector of frequencies of interest ϖ; and
   c. calculate $\Phi(\varpi_i)$ using the input PSD (in the case of Input Module 1, the input PSD $\Phi(\varpi) = \Phi_0$).
2) Calculate $a_{base}(t)_i = 2\sqrt{\Phi(\varpi_i) \cdot \Delta\varpi} \cdot \cos(\varpi_i t + \theta_i)$.
3) Sum $a_{base}(t)_i$ over all *i*.

Output acceleration time histories $a_{base}(t)$ are then fed into the SDOF system representing the Kanai-Tajimi filter.

7.2.3 Step 2: Kanai-Tajimi Filter

The Kanai-Tajimi filter [29, 30] is simply an SDOF oscillator used to represent the filtering affect of the site on which a structure is located. The equation of motion for the SDOF oscillator is

$$\ddot{x}_{KT}(t) + 2\varpi_g \zeta_g \dot{x}_{KT}(t) + \varpi^2{}_g x_{KT}(t) = -a_{base}(t) \tag{7.2}$$

where $x_{KT}(t)$, $\dot{x}_{KT}(t)$, and $\ddot{x}_{KT}(t)$ are the relative displacement, velocity, and acceleration of the oscillator, respectively; and $a_{base}(t)$ is the acceleration from the WN PSD. The output from the filter is the absolute acceleration, which is given by

$$\left(\ddot{z}_g(t)\right)_{KT} = \ddot{x}_{KT}(t) + a_{base}(t) = -2\varpi_g \zeta_g \dot{x}_{KT}(t) - \varpi^2{}_g x_{KT}(t) \tag{7.3}$$

The filter parameters ω_g and ξ_g may be considered to represent characteristic frequency and damping, respectively, of the site on which the structure is located. For example, $\omega_g = 5\pi$ and $\xi_g = 0.6$ are considered to be representative of firm soil conditions [29, 30]. These values were used as base values in this research.

Alternatively, one can integrate Step 1 and Step 2 by generating random histories directly from the PSD of the Kanai-Tajimi filtered white noise using the spectral representation method [31].

7.2.4 Step 3: Modulation Function

A Kanai-Tajimi-filtered white noise is a stationary process. Earthquake ground acceleration processes, however, are generally recognized as being non-stationary. To create a non-stationary input process, the filtered white noise process $\left(\ddot{z}_g(t)\right)_{KT}$ is modulated by a deterministic function of time, $\Psi(t)$, as follows:

$$\ddot{z}_g(t) = \left(\ddot{z}_g(t)\right)_{KT} \cdot \Psi(t) \tag{7.4}$$

where $\ddot{z}_g(t)$ is the resulting modulated acceleration time history.

Clough and Penzien [31] offer the follow modulating function to represent the non-stationarity typical in seismic ground acceleration processes:

$$\Psi(t) = \gamma_1 \cdot t \cdot e^{-\gamma_2 t} \tag{7.5}$$

According to [31], statistical studies of accelerograms during the San Fernando, California earthquake have shown that constants γ_1 and γ_2 can be assigned values of 0.45 and 1/6, respectively. Similar to the values of ω_g and ξ_g in the previous section, these values of γ_1 and γ_2 were considered typical for this research. Using these values, the modulating function $\Psi(t)$ is plotted in Figure 7.3.

7.3 Input Module 2: Target Spectrum

7.3.1 Overview

The analytical flow of Input Module 2 is illustrated in Figure 7.4. The steps of input generation are as follows:

1) A random acceleration time history $a_{base}(t)$ is generated based on the input PSD function $\Phi(\varpi)$ using equation 7.1.

2) $a_{base}(t)$ is multiplied in time by a modulating function $\Psi(t)$ to produce a non-stationary acceleration time history $\ddot{z}_g(t)$, which is used as input to the BRBF system model.

3) The 5%-damping elastic acceleration spectrum $S_a(T)$ is calculated for $\ddot{z}_g(t)$.

4) $S_a(T)$ is compared to the target elastic spectrum $\left(S_a(T)\right)_{target}$.

5) The input PSD $\Phi(\varpi)$ is calibrated such that $S_a(T)$ matches $\left(S_a(T)\right)_{target}$ within a tolerance.

6) Once the input PSD is calibrated, it is used repeatedly in steps 1 and 2 above to generate acceleration time histories for input to the BRBF system model.

Target elastic spectrums and calibration of the input PSD function are described in detail below.

7.3.2 Target Elastic Spectrums

The basic shape of the target elastic spectrums was defined per Chapter 11 in *SEI/ASCE 7-05* [32]; it is shown in Figure 7.5. To define the parameters of the spectrum, a high-seismic location in southern California was chosen, and it was assumed that the location was site class B per *SEI/ASCE 7-05* (rock with soil shear wave velocity between 2,500 and 5,000 feet per second). The parameters were then calculated based on the guidelines in the standard.

Two target spectrums were used in this research; the first was a spectrum that conformed to a design basis earthquake (DBE), and the second was a spectrum that conformed to a maximum considered earthquake (MCE), where DBE and MCE levels were defined per *SEI/ASCE 7-05*. The spectrums are similar, except that $S_a(T)$ for the MCE level is 1.5 times that of the DBE level. Table 7.1 defines the parameters for the DBE and MCE target spectrums used in this research.

7.3.3 Calibration of the Input PSD Function

The input PSD $\Phi(\varpi)$ was calibrated such that the actual 5%-damping elastic spectrum as determined using a standard SDOF oscillator matched the target spectrum. The following algorithm was used to accomplish this (note that this calculation is performed at all selected discrete values of T_i over the domain of the PSD function):

1) Determine the actual elastic spectrum $\left(S_a(T_i)\right)_j$ using a standard SDOF oscillator (5% damping).

2) Compare the actual and target spectrums and calculate a multiplier M_j as follows:

$$M_j(T_i) = \frac{\left(S_a(T_i)\right)_{target}}{\left(S_a(T_i)\right)_j} \tag{7.6}$$

3) Apply the multiplier to the input PSD to generate a new PSD, as follows:

$$\Phi_{j+1}(T_i) = M_j(T_i) \cdot \Phi_j(T_i) \tag{7.7}$$

4) Repeat steps 1 to 5 until the change in the old PSD to the new PSD is less than a tolerance value, which was set to 1% in this research.

5) As the last step in this process, the value of the input PSD at $T = 0$ may need to be altered, because the process tends to result in very high first values of the input PSD. To solve this, the first value of the input PSD was always set equal to the second value. This eliminated the "spike" in the PSD function at $T = 0$.

The calibrated input PSD was then used repeatedly to generate time histories that conformed to the target spectrums. Calibration needed to be performed only once for a given target spectrum. In some cases, manual manipulation of the input PSD was required to ensure that the actual elastic spectrum matched the target, particularly near T_S. After this manipulation, though, the actual and target spectrums matched well (see Figure 7.6 for an example of how well the spectrums matched). Figure 7.7 and Figure 7.8 show the calibrated PSD functions for the DBE and MCE target spectrums, respectively.

7.4 Chapter 7 Figures

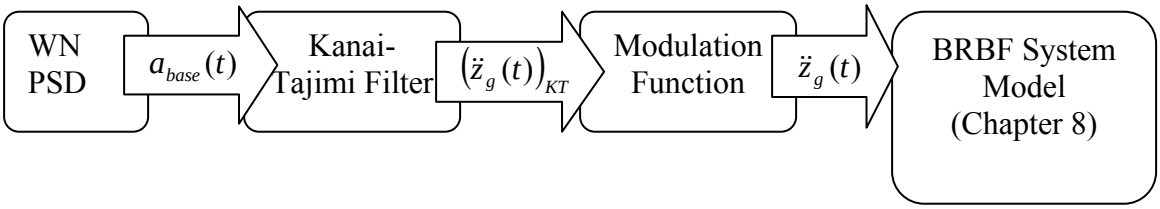

Figure 7.1: Input Module 1

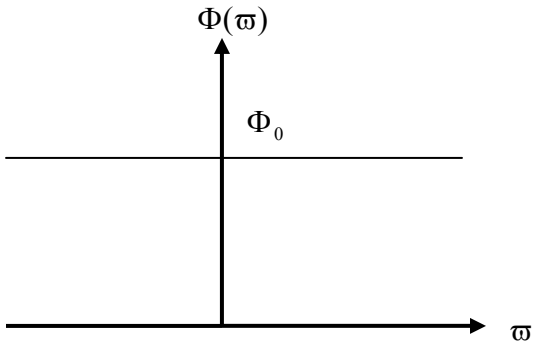

Figure 7.2: Input PSD Function for Input Module 1

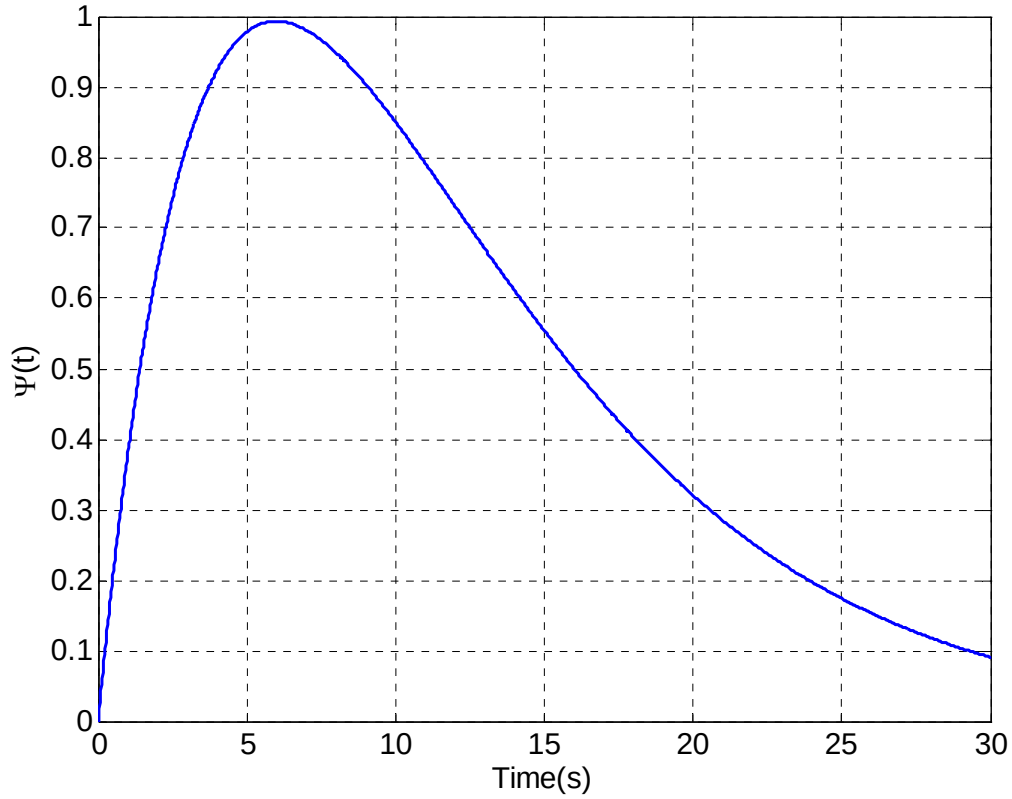

Figure 7.3: Modulation Function

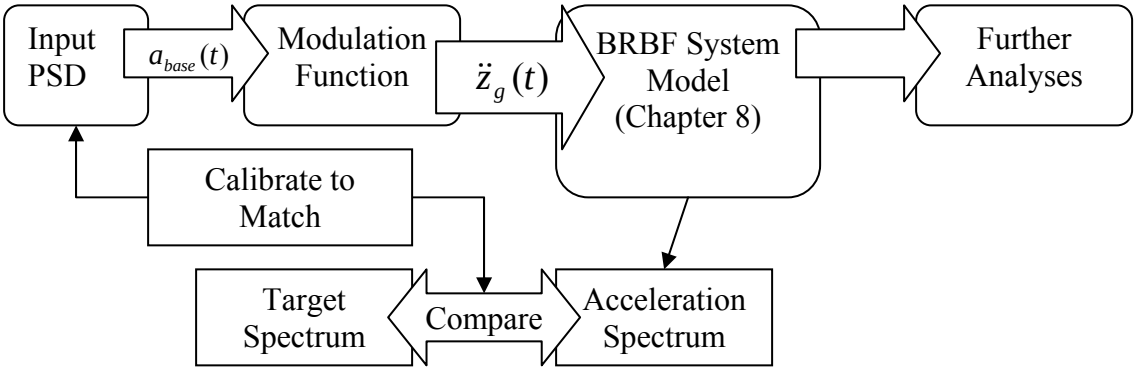

Figure 7.4: Input Module 2

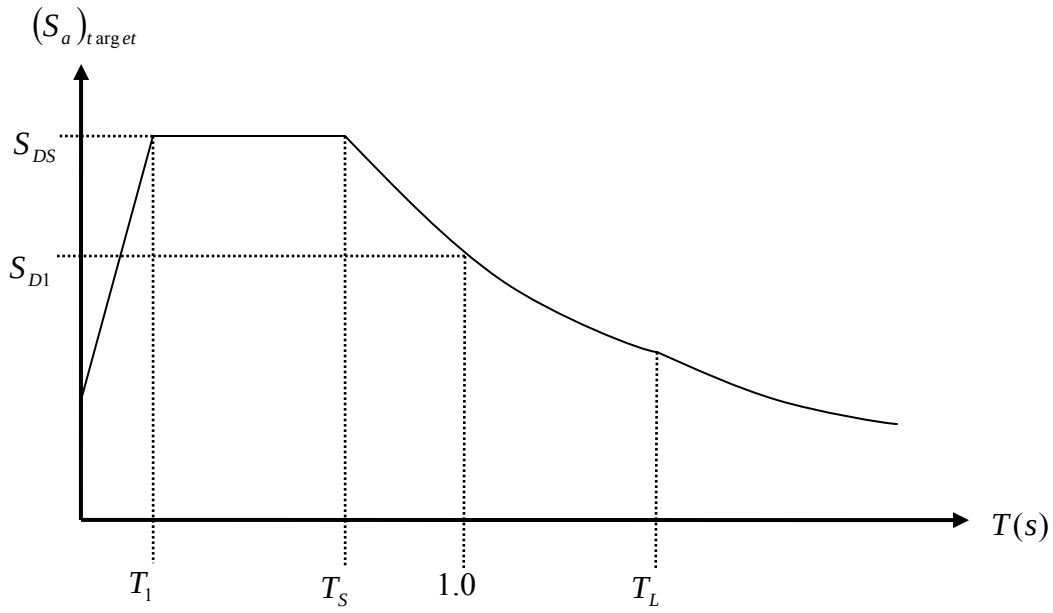

Figure 7.5: Target Spectrum Shape and Parameters

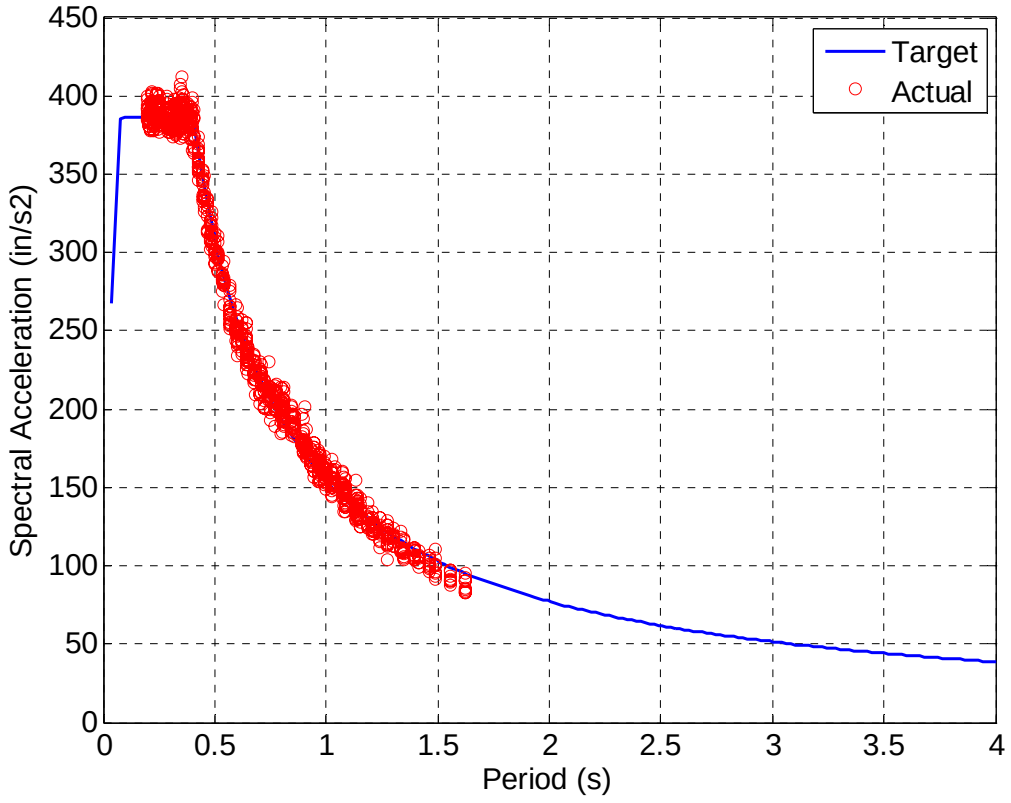

Figure 7.6: Comparison between Actual and Target Spectrums for DBE Level (1000 comparison points)

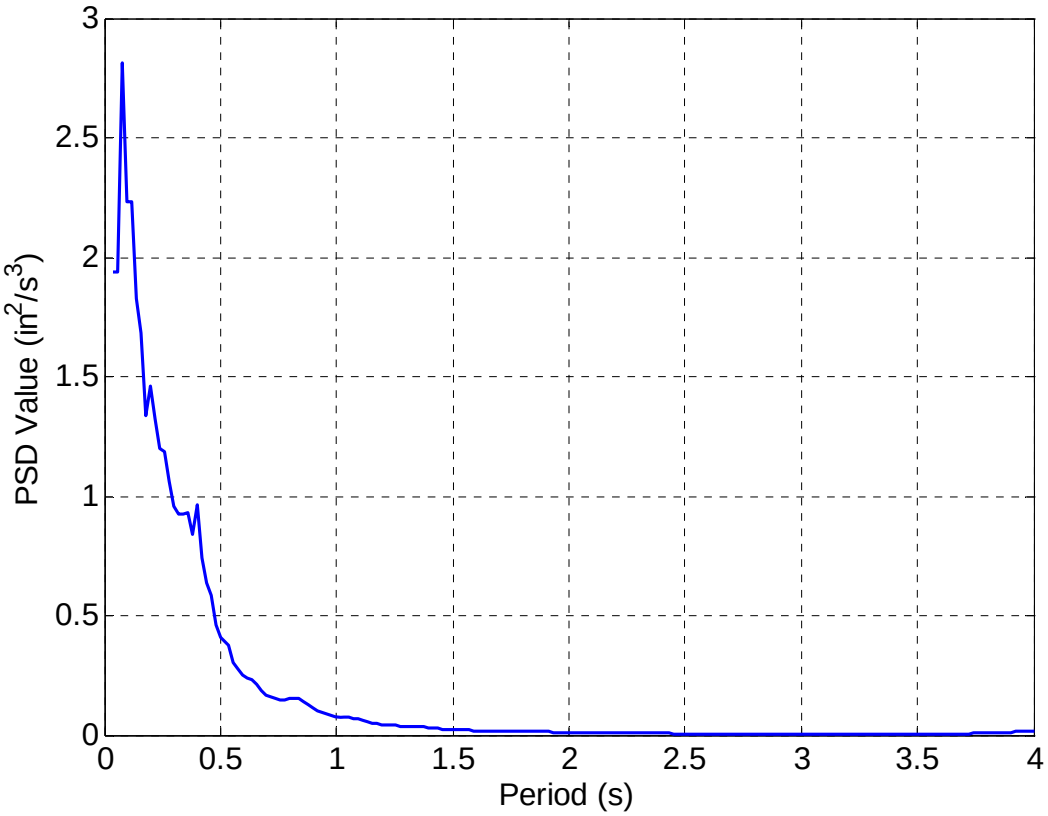

Figure 7.7: Calibrated Input PSD for DBE Target Spectrum

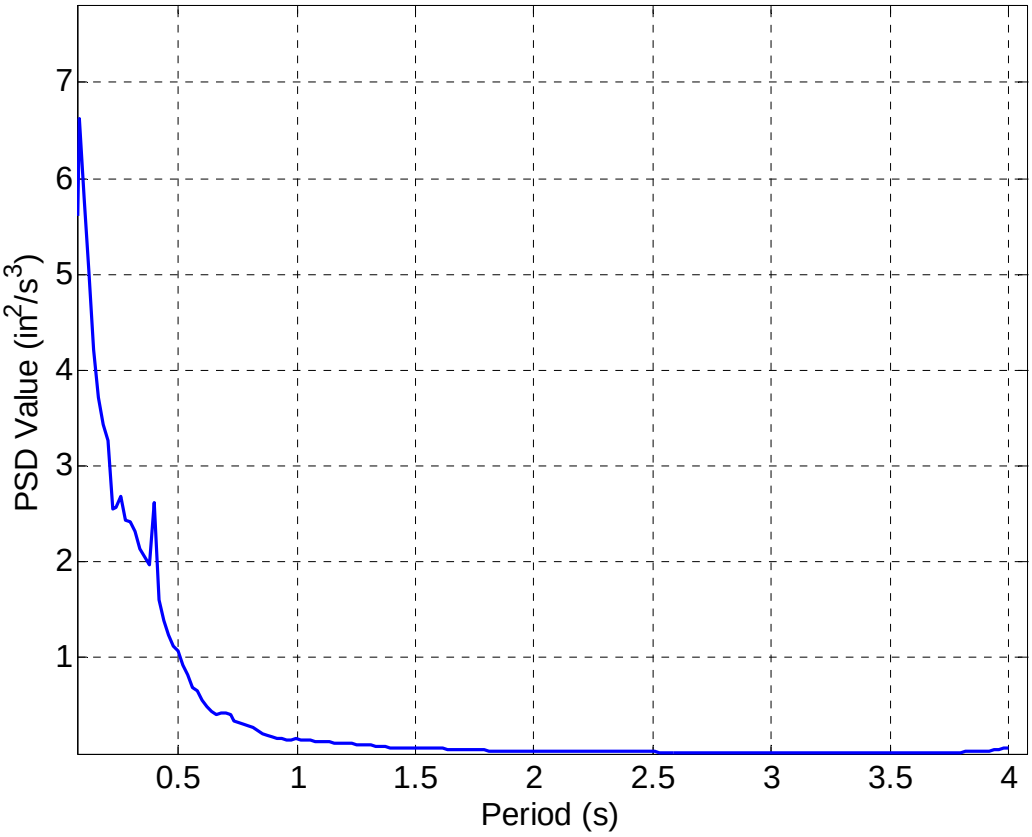

Figure 7.8: Calibrated Input PSD for MCE Target Spectrum

7.5 Chapter 7 Tables

Table 7.1: Parameters for Target Spectrums

Parameter	DBE Spectrum	MCE Spectrum
S_{DS}	1.0 g	1.5 g
S_1	.40 g	.60 g
T_1	.08 s	.08 s
T_S	.40 s	.40 s
T_L	8.0 s	8.0 s

Chapter 8

BRBF SYSTEM MODEL AND SIMULATION

8.1 Overview

The models for the BRBF system and BRB are described in this chapter in addition to the methods of nonlinear dynamic analysis used. Section 8.2 describes the physical structural model of the BRBF system; Section 8.3 describes the mathematical models for the BRBF system and BRB; Section 8.4 describes the nonlinear dynamic analysis; and Section 8.5 outlines the deformation calculations performed to calculate the predictor parameters defined in Section 3.3.

8.2 Physical Model of Structural System

A prototype structural system was selected based on average values from the BRB test database. It is shown in Figure 8.1. The connections between the beams and columns are assumed to be pinned; therefore, the section sizes of beams and columns are not important, as all lateral stiffness for the system is imparted by the BRB (under small deformations). The structural system was assumed to have a single lumped mass m associated with it. While BRBs typically consist of 5 regions, as delineated in Figure 2.1, a simplified BRB structural model was used in this research where the BRB was modeled as consisting of three regions: the core yielding region and two non-core regions (the non-core regions are sections of the brace with a larger cross-sectional area than the core region that do not yield during loading). Pertinent BRB and BRBF properties are identified in Table 8.1 .

8.3 Mathematical Models

A mathematical model of the system was derived from the physical structural model and is given in Figure 8.2. Parameters of the mathematical model are defined in Table 8.2.

The equation of motion (EOM) for the system was derived assuming no coupling of the structure and the ground (i.e. the ground serves only as a filter). It is given below.

$$\ddot{x} + 2\xi_0\omega_0\dot{x} + \frac{P}{m}\cos 45 = -\ddot{z}_g \tag{8.1}$$

where ξ_0 is the modal damping ratio of the structure; $\varpi_0 = \sqrt{\frac{K_{wp}\cos^2(45)}{m}}$ is the elastic natural frequency of the structure; P is the BRB axial force; and K_{wp} is the elastic stiffness of the BRB between the work points (WPs), which is given by

$$K_{WP} = \frac{1}{\frac{L_c}{A_c E} + 2\frac{L_{nc}}{A_{nc} E}} \tag{8.2}$$

A Bouc-Wen (BW) model was used to model the hysteric response of the BRB (see [38] for a general summary on Bouc-Wen class models). Per [1], BRB axial force is given by

$$P = \alpha K_{wp} u + (1-\alpha) K_{wp} u_y z \tag{8.3}$$

where α is the ratio of post-yield to pre-yield stiffness; u is the displacement of the WPs in the direction of the BRB (hereafter referred to as BRB WP deformation); and z is an evolutionary variable controlled by the following differential equation (from [1])

$$u_y \dot{z} + \gamma_{BW} |\dot{u}| z |z|^{n-1} + \beta_{BW} \dot{u} |z|^n - \dot{u} = 0 \tag{8.4}$$

where u_y is the BRB WP deformation at initial yielding of the BRB; $u_y = \frac{P_y}{K_{wp}}$; γ_{BW} and β_{BW} are model parameters that affect the shape of the hysteric curve; and n is a model parameter that affects the smoothness of the transition from pre-yield to post-yield behavior.

The BW model parameters for the BRB were taken from Black et al. [1], who performed tests on multiple BRBs and calibrated the BW model parameters such that the hysteric behavior predicted by the BW model matched the test specimen behavior. Chosen standard BW model parameters are given by Table 8.3. Note that u_y in the BW model was increased artificially by 25% from the value calculated using BRB properties. This is because Black et al. [1] observed that this change resulted in better agreement between predicted and test behavior.

The final form of the EOM is determined by substituting equation 8.3 into equation 8.1 and by noting that $x = \frac{u}{\cos 45}$ and setting $n = 1$:

$$\ddot{x} + 2\xi_0 \omega_0 \dot{x} + \frac{\cos 45}{m}[\alpha K_{wp} x \cos 45 + (1-\alpha) K_{wp} u_y z] + \ddot{z}_g = 0 \tag{8.5}$$

$$u_y \dot{z} + \gamma_{BW} |\dot{x} \cos 45| z + \beta_{BW} \dot{x} \cos 45 |z| - \dot{x} \cos 45 = 0 \tag{8.6}$$

8.4 Nonlinear Dynamic Analysis

Nonlinear dynamic analysis was performed based on equation 8.5 and 8.6 using the Simulink® toolbox of Matlab®. The Simulink® toolbox is a tool for performing linear and non-linear simulation, and it uses calculation flow schematics (i.e. box and arrow schematics) to represent the analysis. The Simulink® model for the BRBF system is shown in Figure 8.3.

The analysis model is aptly described by dividing it into the following sections or components:

- Input modules
- BRBF system model
- Outputs
- Integration methods
- Anti-aliasing (AA) filters
- Controlling Matlab® code

Each component or section is described in the sections that follow.

8.4.1 Input Modules

A close-up view of the input module component of the Simulink® model is shown in Figure 8.4. The flow of Input Module 1 is explained as follows:

1) A random time history is generated using the Band-Limited White Noise block.

2) This time history is passed through the AA filter (AA Filter 5 box in the figure).

3) The time history is passed through a SDOF system representing the KT filter (using the K-T Filter box).

4) The modulation function component generates the modulation function $\Psi(t)$ per Section 7.2.4.

5) The time history from Step 3 is multiplied by the modulation function from Step 4.

6) The modulated time history is passed to the BRB system model.

The flow of Input Module 2 (target spectrum) is much simpler. A random time history is generated using equation 7.1 and the algorithm in Section 7.2.2 and multiplied by $\Psi(t)$. This random time history is loaded into the Simulink® model and then passed to the BRBF system model.

8.4.2 BRBF System Model

A close-up view of the BRBF system model is presented in Figure 8.5. The EOM block is shown in Figure 8.6. This block is a differential equation editor block in Simulink®, which allows for the solution of nonlinear EOM; however, the EOM must be transformed from second order to first order. The second order system of equations is given by $\mathbf{f}(\mathbf{x},\mathbf{u}) = \mathbf{0}$, where $\mathbf{f}(\mathbf{x},\mathbf{u})$ is the left-hand side of the system given by equations 8.5 and 8.6; $\mathbf{x} = \begin{bmatrix} x & \dot{x} & z \end{bmatrix}^T$; and $\mathbf{u} = \ddot{z}_g$. The equivalent first-order system of equations, $\frac{d\mathbf{x}}{dt} = \mathbf{0}$, is given by

$$\frac{d\mathbf{x}}{dt} = \begin{bmatrix} \mathbf{x}(2) \\ \left(2\xi_0\omega_0 \cdot \mathbf{x}(2) + \frac{\cos 45}{m}[\alpha K_{wp} \cdot \mathbf{x}(1) \cdot \cos 45 + (1-\alpha)K_{wp}u_y \cdot \mathbf{x}(3)] + \mathbf{u}(1)\right) \\ -\frac{\left(\gamma_{BW}\left|\mathbf{x} \cdot (2)\cos 45\right| \cdot \mathbf{x}(3) + \beta_{BW}\mathbf{x}(2)\cos 45\left|\mathbf{x}(3)\right| - \mathbf{x}(2) \cdot \cos 45\right)}{u_y} \end{bmatrix} = \begin{bmatrix} 0 \\ 0 \\ 0 \end{bmatrix} \tag{8.7}$$

The system of equations given by 8.7 is entered into the differential equation editor block.

8.4.3 Outputs

A close-up view of the output component is shown in Figure 8.7. The output blocks produce the following variables in the Matlab® workspace:

- *x0* is the system relative displacement x.
- *xd0* is the system relative velocity $\dot{x}$.
- *xadd0* is the mass absolute acceleration $\ddot{x}_a$.
- *z0* is the evolutionary variable form the BW model z.

These variables are further used in the Matlab® workspace to calculate BRB core deformation and to calculate capacity model predictor parameters (as defined in Section 3.3).

8.4.4 Integration Method

A Dormand-Prince ordinary differential equation solver algorithm [39] was used to perform time-step integration of the controlling EOM in the EOM block. A variable time step was used for time-step integration where the time step was varied by Simulink® based on the dynamical response of the system. While a variable time step was used for integration, a fixed time step was used to sample values from the integration (such as input values and output values). This time step was selected to be 10 times smaller than the natural frequency of the system. Parametric studies showed that this ratio was adequate for the level of precision required in the BRB deformation calculations.

8.4.5 Anti-aliasing Filters

Because the time-step used for integration was much smaller than the sampling frequency, anti-aliasing (AA) filters were used in multiple places in the Simulink® model to avoid aliasing effects (which are generally described in [40]). If connected to the input signal, only one AA filter was required. However, if not connected to the input signal, AA filters were required wherever output values were sampled. The AA filters used in Simulink® represented 8-pole digital filters; the cutoff frequency was set at 98% of the Nyquist frequency.

8.4.6 Controlling Matlab Code

A separate Matlab® code was created to control the entire simulation process, including input generation, simulation using Simulink®, extraction of output values, and calculation of BRB core deformation parameters. This code is presented in Appendix D. The same code was also used to perform reliability calculations and to perform parametric studies (as described in Chapter 10 and 11).

8.5 BRB Deformation Calculations

BRB core deformation was calculated based on the output values of x and z from the Simulink® model using the following equation:

$$u_c = u - \frac{2P}{K_{nc}} = u - \frac{2}{K_{nc}}\left[\alpha K_{wp} u + (1-\alpha) K_{wp} u_y z\right] \tag{8.8}$$

where u is the BRB work-point deformation given by $u = x\cos 45$.

The BRB core deformation history $u_c(t)$ was used as outlined in Section 3.3 to determine deformation descriptor predictor parameters such as μ_c, $\mu_{\max}$, and $\mu_{\max loc}$.

8.6 Chapter 8 Figures

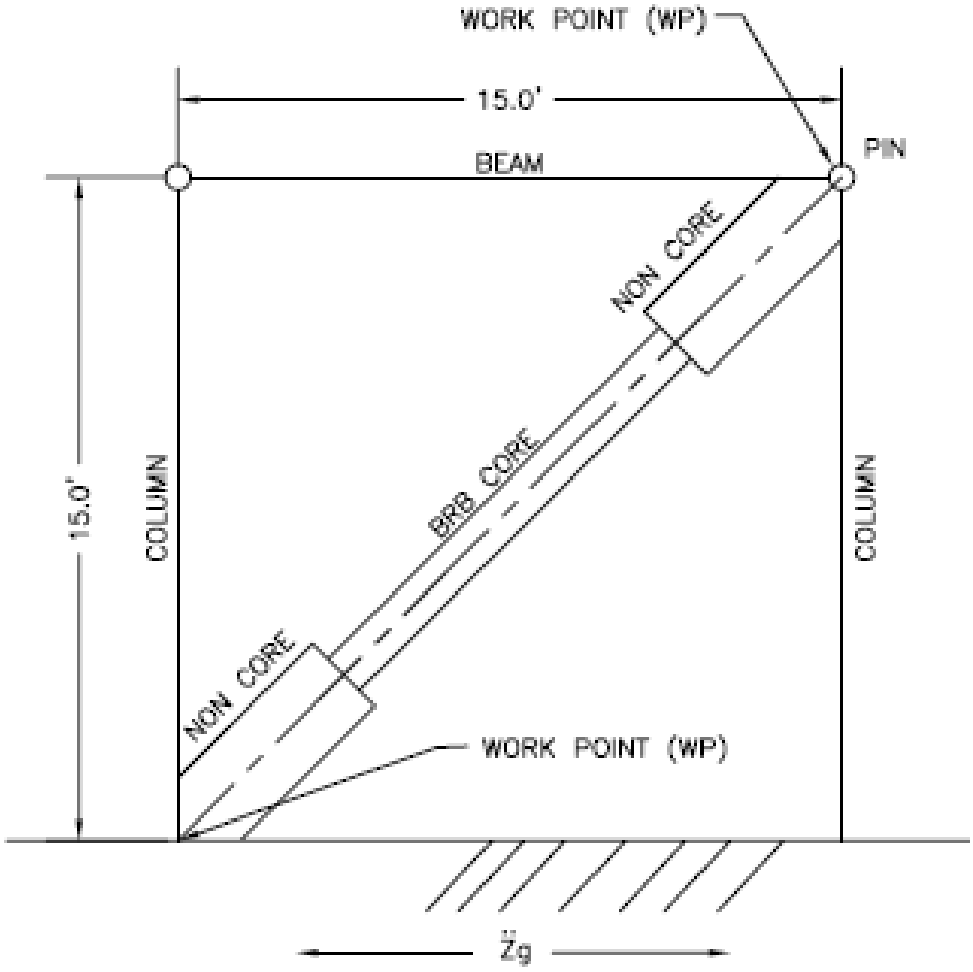

Figure 8.1: Structural System Physical Model

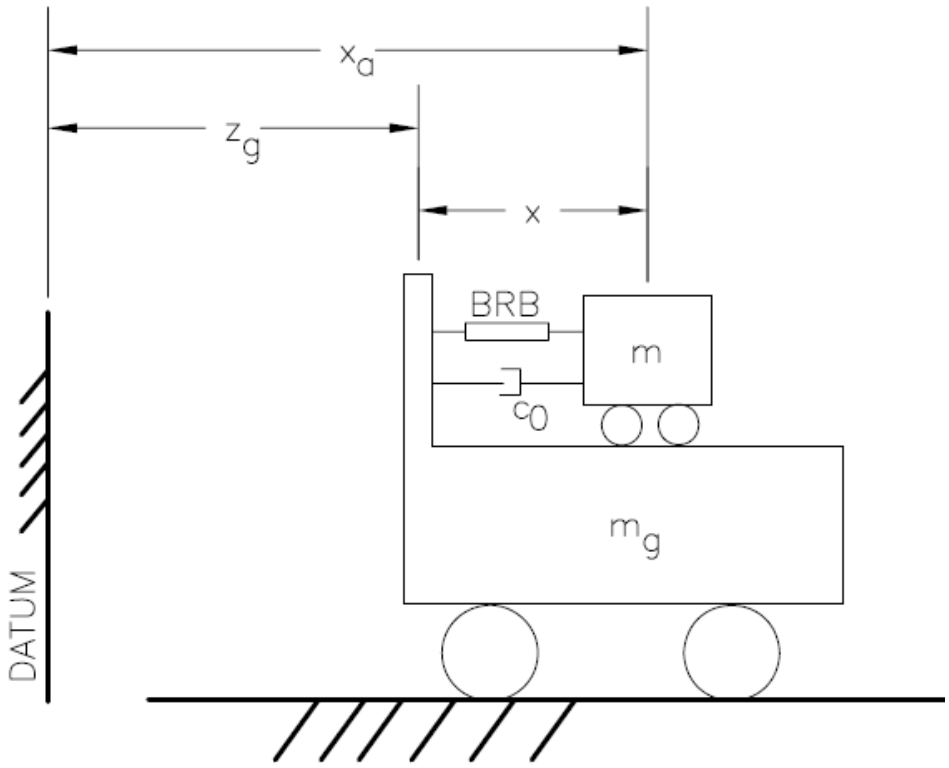

Figure 8.2: BRBF System Mathematical Model

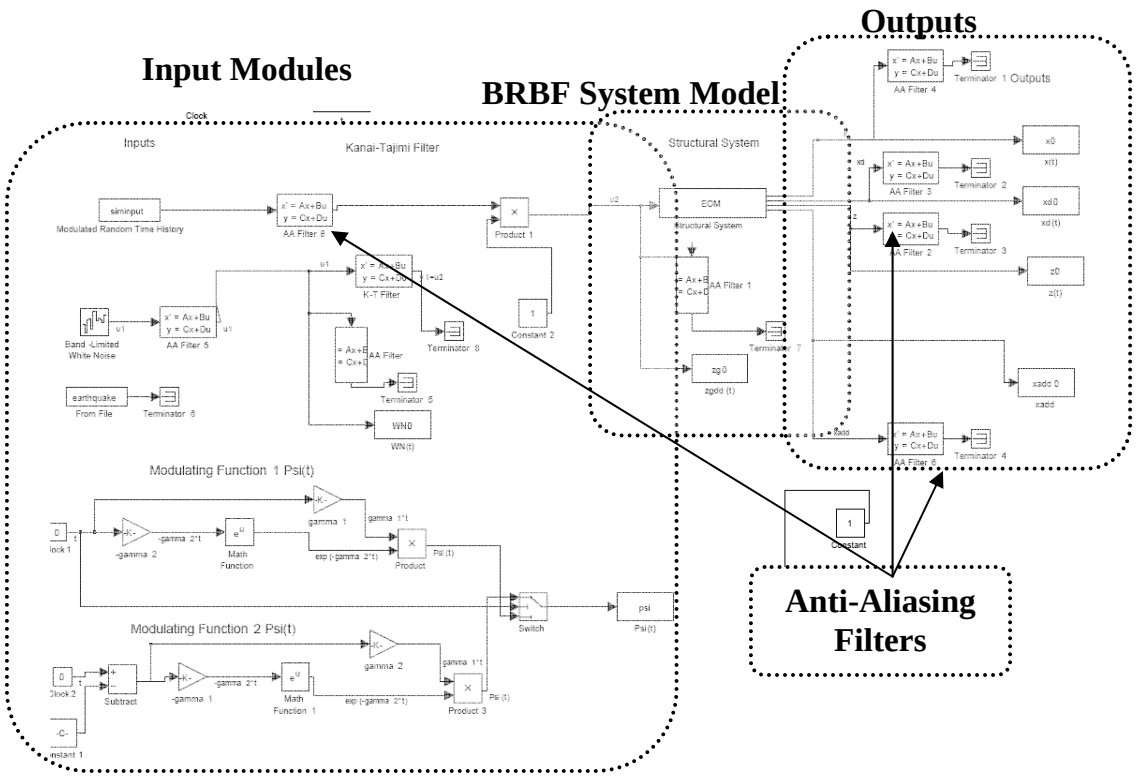

Figure 8.3: Simulink® Model

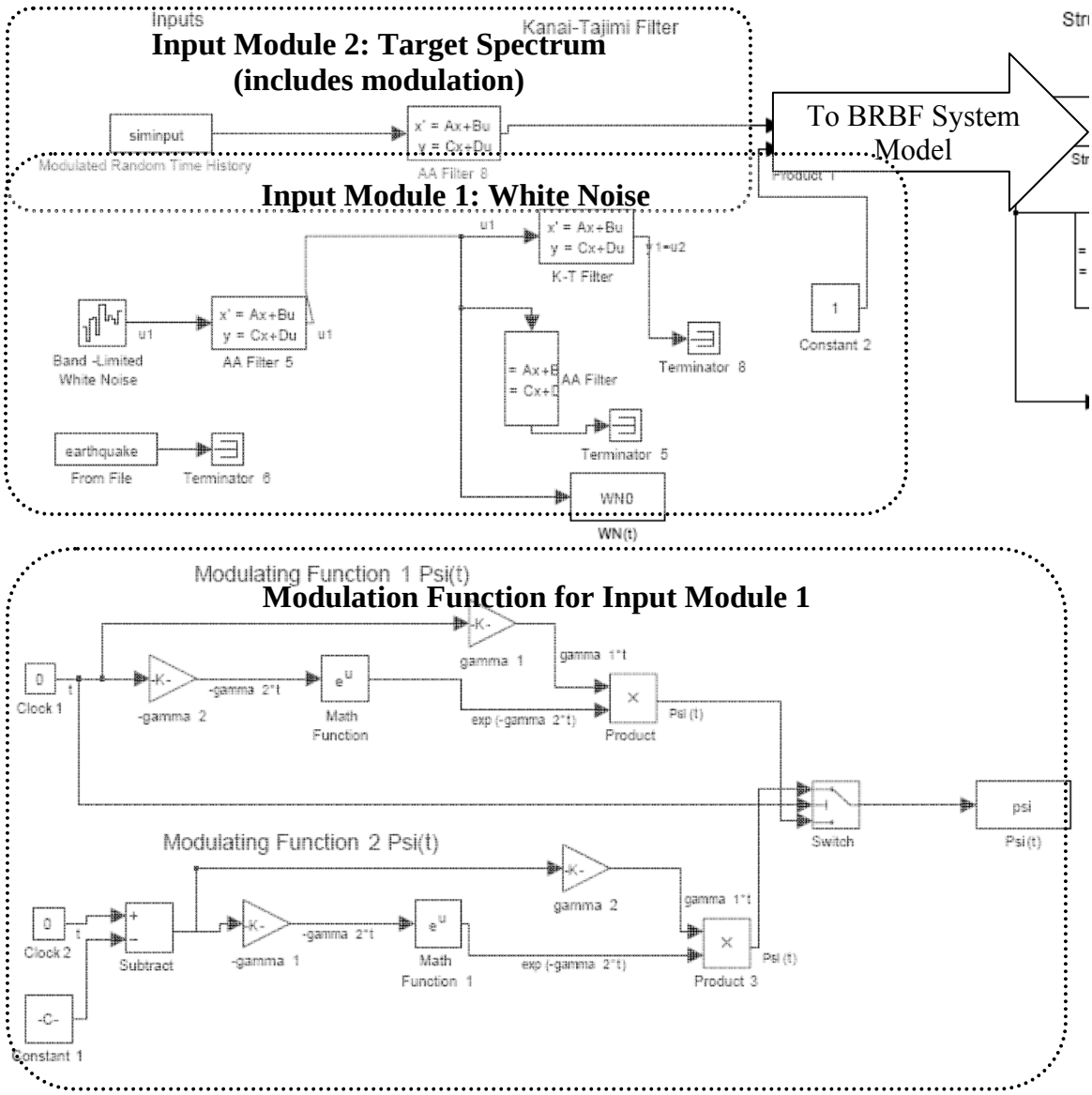

Figure 8.4: Input Modules in Simulink®

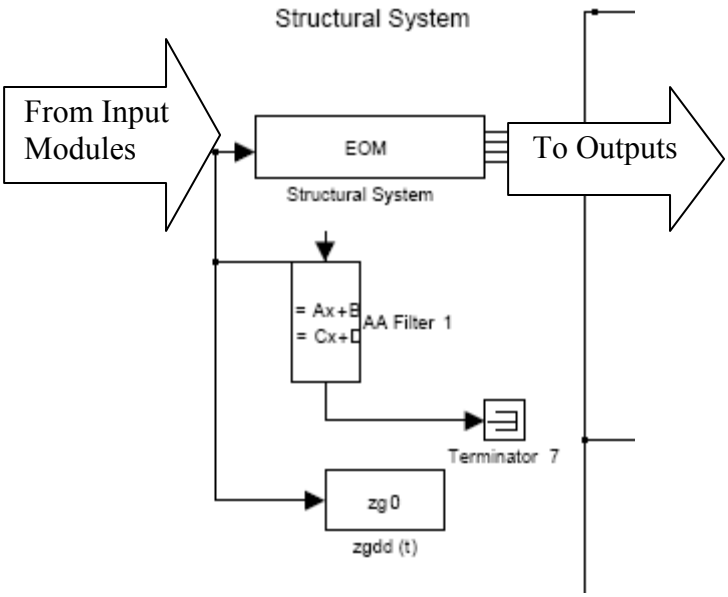

Figure 8.5: BRBF System Model in Simulink®

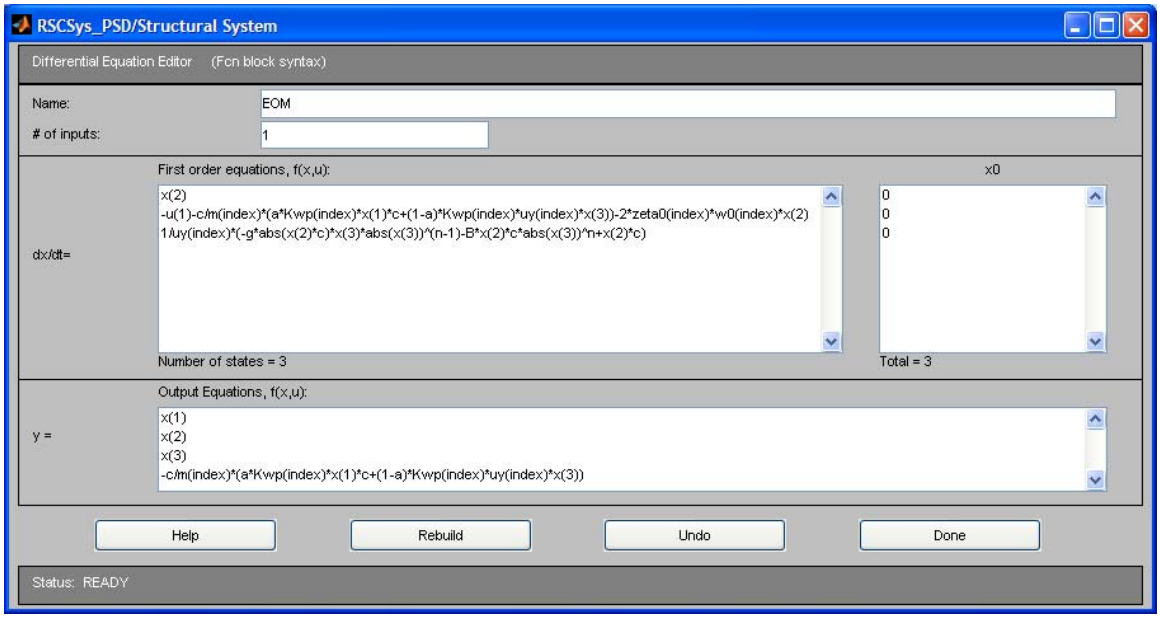

Figure 8.6: BRBF System (EOM) Block

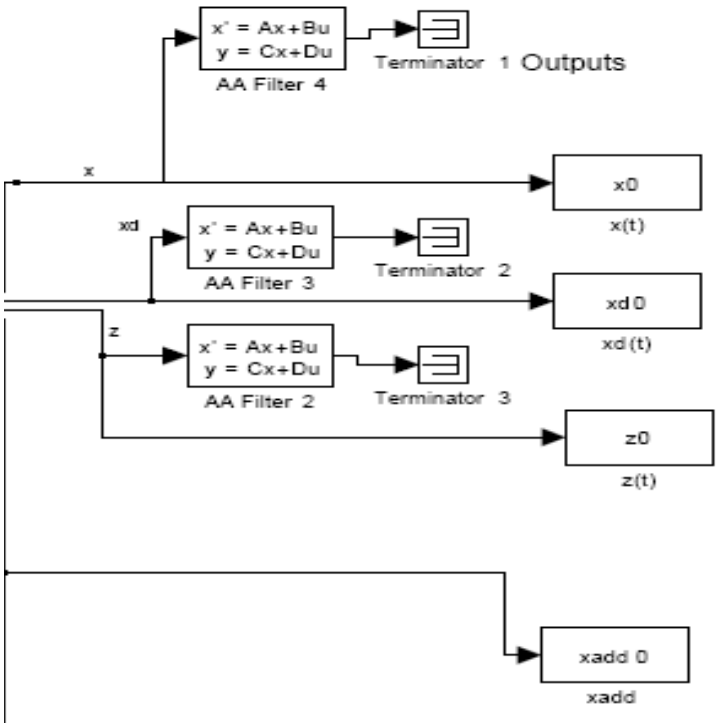

Figure 8.7: Simulink® Outputs Component

8.7 Chapter 8 Tables

Table 8.1: BRB and BRBF Physical Structural Model Parameter Definitions

Parameter	Variable
Core Area	A_c
Core Length	L_c
Non-Core Area	A_{nc}
Non-Core Length	L_{nc}
Core Yield Force	P_y
Elastic Modulus	E
Structure Mass	m

Table 8.2: Mathematical Model Definitions

Variable	Parameter
$\ddot{z}_g(t)$	Ground Acceleration (from Input Modules)
$x(t)$	Relative Displacement of Mass
$\ddot{x}_a(t)$	Absolute Acceleration of Mass
m	System Mass
m_g	Ground
c_0	Damping Coefficient of System

Table 8.3: Bouc-Wen Model Parameters

α	γ_{BW}	β_{BW}	n
0.025	0.45	0.55	1

Chapter 9

RANDOM VIBRATION ANALYSIS

9.1 Overview

A random vibration analysis was performed (which is depicted as Analysis Pathway 2 in Figure 1.4) to determine the mean and variance of the BRB core deformation process such that probabilistic distributions of the deformation history predictive parameters described in Chapter 3 could be evaluated. This was accomplished by performing random vibration analysis using the **BRBF system model**, where the non-linear equations of motion (EOM) given by equations 8.5 and 8.6 were linearized using the equivalent linearization method (ELM) [28, 38]. Using the random vibration analysis tools, the effects of seismic loading, BRB, and BRBF properties on the mean and variance of the BRB core deformation process were determined. Thus the effects of the seismic loading, BRB, and BRBF properties on BRB demands and system reliability were quantified, and this provided information about which parameters are important for consideration in the PBEF.

First, in Section 9.2, the linearization of the system EOM is outlined; second, in Section 9.3 the methods of random vibration analysis are described; next, in Section 9.4, results from the random vibration analysis are summarized, including considerations for the PBEF framework; and finally, summary and conclusions are presented in Section 9.5.

9.2 Linearization of the System

In order to obtain information on the mean and variance of the core deformation process $\mu_c(t)$, random vibration analysis must be performed. The ELM was used because it is considered a random vibration method that has the highest potential for practical use due to its applicability to a wide class of problems and efficiency. It requires linearization of the EOM given by equations 7.2, 7.3, 7.4, 8.5 and 8.6, which are repeated here for convenience.

$$\ddot{x}_{KT}(t) + 2\varpi_g \zeta_g \dot{x}_{KT}(t) + \varpi^2{}_g x_{KT}(t) = -a_{base}(t) \tag{7.2}$$

$$\left(\ddot{z}_g(t)\right)_{KT} = \ddot{x}_{KT}(t) + a_{base}(t) = -2\varpi_g \zeta_g \dot{x}_{KT}(t) - \varpi^2{}_g x_{KT}(t) \tag{7.3}$$

$$\ddot{z}_g(t) = \left(\ddot{z}_g(t)\right)_{KT} * \Psi(t) \tag{7.4}$$

$$\ddot{x} + 2\xi_0 \omega_0 \dot{x} + \frac{\cos 45}{m}[\alpha K_{wp} x \cos 45 + (1-\alpha) K_{wp} u_y z] + \ddot{z}_g = 0 \tag{8.5}$$

$$u_y \dot{z} + \gamma_{BW} |\dot{x} \cos 45| z + \beta_{BW} \dot{x} \cos 45 |z| - \dot{x} \cos 45 = 0 \tag{8.6}$$

Combining equations 7.3 and 7.4 and substituting them into the equation 8.5 yields:

$$\begin{aligned}
&\ddot{x}_{KT} + 2\varpi_g \zeta_g \dot{x}_{KT} + \varpi^2{}_g x_{KT} = -a_{base}(t) \\
&\ddot{x} + 2\xi_0 \omega_0 \dot{x} + \frac{\cos 45}{m}[\alpha K_{wp} x \cos 45 + (1-\alpha) K_{wp} u_y z] - 2\varpi_g \zeta_g \dot{x}_{KT} \Psi(t) - \varpi^2{}_g x_{KT} \Psi(t) = 0 \\
&u_y \dot{z} + \gamma_{BW} |\dot{x} \cos 45| z + \beta_{BW} \dot{x} \cos 45 |z| - \dot{u} = 0
\end{aligned} \tag{9.1}$$

The linearization of the above EOM was performed as follows [28]. First, if the EOM are arranged in the form $\mathbf{g}(\mathbf{x}, \dot{\mathbf{x}}, \ddot{\mathbf{x}}) = \mathbf{f}$, where **g** is the left hand side of equation 9.1; **f** is the right hand side of equation 9.1; and $\mathbf{x} = \begin{bmatrix} x_{KT} & x & z \end{bmatrix}^T$; then an equivalent linear system is given by

$$\mathbf{M}\ddot{\mathbf{x}} + \mathbf{C}\dot{\mathbf{x}} + \mathbf{K}\mathbf{x} = \mathbf{f} \tag{9.2}$$

where

$$M_{ij} = \mathrm{E}\left[\frac{\delta g_i}{\delta \ddot{x}_j}\right];\ C_{ij} = \mathrm{E}\left[\frac{\delta g_i}{\delta \dot{x}_j}\right];\ \text{and}\ K_{ij} = \mathrm{E}\left[\frac{\delta g_i}{\delta x_j}\right]. \tag{9.3}$$

This formulation minimizes the mean square error (the difference between nonlinear and equivalent linear systems) [41]. The coefficients M_{ij} , C_{ij} , and K_{ij} are all deterministically determined except that

$$C_{32} = -\gamma_{BW} \cdot \mathrm{E}\left[z \frac{\delta |\dot{x}|}{\delta \dot{x}} \right] + \beta_{BW} \cdot \mathrm{E}[|z|] - 1 \tag{9.4}$$

$$K_{33} = \cos 45 \left\{ \gamma_{BW} \cdot \mathrm{E}[|\dot{x}|] + \beta_{BW} \cdot \mathrm{E}\left[\dot{x} \frac{\delta |z|}{\delta z} \right] \right\} \tag{9.5}$$

As the input white noise process $a_{base}(t)$ is Gaussian and the structural system is now linearized, it follows that $\dot{x}$ and z are now jointly Gaussian. Thus the two coefficients C_{32} and K_{33} can be determined in terms of the second moments of $\dot{x}$ and z as

$$C_{32} = \sqrt{\frac{2}{\pi}} \left\{ \left[\gamma_{BW} \frac{\mathrm{E}[\dot{x}z]}{\sigma_{\dot{x}}} + \beta_{BW} \sigma_z \right] \right\} - 1 \tag{9.6}$$

$$K_{33} = \sqrt{\frac{2}{\pi}} \cos 45 \left\{ \gamma_{BW} \sigma_{\dot{x}} + \beta_{BW} \frac{\mathrm{E}[\dot{x}z]}{\sigma_z} \right\} \tag{9.7}$$

The complete system of equations is now linear and can be used to perform a dynamic analysis given the second moments of $\dot{x}$ and z.

9.3 Random Vibration Analysis

After linearizing the EOM using the ELM, random vibration analysis was performed to determine the covariance matrix of the response variables in $\mathbf{x}$. First, the EOM given by equations 9.2, 9.3, 9.6, and 9.7 were converted to the state-space form:

$$\dot{\mathbf{y}} = \mathbf{G}\mathbf{y} + \mathbf{f} \tag{9.8}$$

where $\mathbf{y} = \begin{bmatrix} x_{KT} & \dot{x}_{KT} & x & \dot{x} & z \end{bmatrix}^T$; $\mathbf{f} = \begin{bmatrix} 0 & -a_{base}(t) & 0 & 0 & 0 \end{bmatrix}^T$; and

$$\mathbf{G} = \begin{bmatrix} 0 & 1 & 0 & 0 & 0 \\ -\omega_g{}^2 & -2\xi_g\omega_g & 0 & 0 & 0 \\ 0 & 0 & 0 & 1 & 0 \\ \omega_g{}^2\Psi(t) & 2\xi_g\omega_g\Psi(t) & \dfrac{-(\cos 45)^2\alpha K_{wp}}{m} & -2\xi_0\omega_0 & -\dfrac{\cos 45(1-\alpha)K_{wp}u_y}{m} \\ 0 & 0 & 0 & \dfrac{C_{32}}{u_y} & \dfrac{K_{33}}{u_y} \end{bmatrix}$$

Random vibration analysis was performed using two methods: (1) the stationary Lyapunov equation (in which $\Psi(t)$ was taken to always be 1), and (2) the time-varying Lyapunov equation (in which $\Psi(t) = \gamma_1 t e^{-\gamma_2 t}$). Both formulations of the Lyapunov equation assume that all processes $\mathbf{y}(t)$ are zero mean. The stationary Lyapunov equation is given by

$$\mathbf{0} = \mathbf{G}\mathbf{S} + \mathbf{S}\mathbf{G}^T + \mathbf{B} \tag{9.9}$$

where $\mathbf{S} = \mathrm{E}\left[\mathbf{y}\mathbf{y}^T\right]$ and $\mathbf{B} = \mathrm{E}\left[\mathbf{f}\mathbf{f}^T\right] = \begin{bmatrix} 0 & 0 & 0 & 0 & 0 \\ 0 & 2\pi\Phi_0 & 0 & 0 & 0 \\ 0 & 0 & 0 & 0 & 0 \\ 0 & 0 & 0 & 0 & 0 \\ 0 & 0 & 0 & 0 & 0 \end{bmatrix}$.

To solve this equation, an iterative solution procedure was used. The steps of this procedure were as follows:

1) Guess initial values of $\mathrm{E}[\dot{x}z]$, $\sigma_{\dot{x}}$, and σ_z. To start, these values were based on results from an analysis of the linearized system (i.e. using initial stiffness values). However, some modification of these values (using trial and error) was required to cause the solution procedure to converge.

2) Calculate the new covariance matrix **S** using the "lyap" command in Matlab®, which solves equation 9.9 for **S**. This command transforms the **G** matrix to the complex Schur form, computes the solution of the resulting triangular system, and transforms this solution back [42]. (See Matlab® code in the Appendix D for more details.)

3) Extract values of $\mathrm{E}[\dot{x}z]$, $\sigma_{\dot{x}}$, and σ_z from **S.**

4) Repeat Steps 2 and 3 until the changes in **S** from one step to the next become negligible.

The general time-varying Lyapunov equation is given by

$$\frac{d}{dt}\mathbf{S} = \mathbf{GS} + \mathbf{SG}^T + \mathbf{B} \tag{9.10}$$

For the time varying solution, the "ODE45" command in Matlab® was used to perform time-step integration of equation 9.10 to solve for $\mathbf{S}(t)$. This command uses an explicit Runge-Kutta formula, the Dormand-Prince pair [39], to perform the integration. (See Appendix D for the corresponding Matlab® code.) It required only an initial covariance matrix **S** at time t = 0. The time-step integration was performed for a duration of 30s.

9.3.1 BRB Core Deformation

The main goal of the random vibration analysis was to determine the mean and variance of the BRB core deformation process. In general, the core deformation is given by

$$u_c = u - \frac{2P}{K_t} = u - \frac{2}{K_t}\left[\alpha K_{wp} u + (1-\alpha) K_{wp} u_y z\right] \tag{9.11}$$

Using equation 9.11, the variance of u_c, which is assumed to be zero mean, is

$$\mathrm{E}[u_c u_c] = \left[1 - \frac{2\alpha K_{wp}}{K_t}\right]^2 \cdot \mathrm{E}[u^2] - 2\left[1 - \frac{2\alpha K_{wp}}{K_t}\right]\left[\frac{2(1-\alpha)K_{wp}u_y}{K_t}\right] \cdot \mathrm{E}[uz] + \left[\frac{2(1-\alpha)K_{wp}u_y}{K_t}\right]^2 \cdot \mathrm{E}[z^2] \tag{9.12}$$

Using the ELM, either Lyapunov equation solution can be used to determine the statistical moments in equation 9.12 efficiently.

9.3.2 Monte Carlo Simulation

As the ELM method is an approximation to the full nonlinear EOM, it inherently contains error. To assess the accuracy of the ELM method, Monte Carlo simulation was performed to validate the solutions obtained using the ELM. This was accomplished using the Simulink® feature in Matlab®. (See Appendix D for the Matlab® code and Simulink® system diagram.) Input Module 1 was used to generate random ground-acceleration time histories using the white noise input PSD (with magnitude Φ_0), and each process realization was 30s in length. Other BRB and BRBF properties used in the analysis are described in Section 9.4.1. The BRB core deformation process $u_c(t)$ was determined using equation 9.11.

The mean and variance processes of **y** were estimated in an ensemble sense − the sample mean and variance of the realization values of multiple response time histories were determined at each discrete point in time.

9.4 Random Vibration Analysis Results

9.4.1 Properties used in Analysis

BRB, Bouc-Wen model, BRBF, and Input Process properties used in the random vibration analysis are summarized in Table 9.1, Table 9.2, Table 9.3, and Table 9.4, respectively. BRB properties were taken as average values from the BRB test database (see Appendix A for the database).

Bouc-Wen model properties were taken from Black et al. [1] as described in Section 8.3, except that the brace work point yield deformation was determined as

$$u_y = 1.25 \cdot \frac{P_y}{K_{wp}} = 0.348\,\text{in} \tag{9.13}$$

Recall that the yield displacement was increased by 25% over the value from BRB properties based on the suggestion by [1].

The system mass was determined by using the DBE target spectrum defined in Section 7.3.2; the design spectral acceleration S_a was chosen as the peak value of the spectrum, which was 1 g. A typical response modification coefficient, R, for BRBFs of 8 (based on guidance given in [32]) was used in conjunction with the brace yield force P_y to determine the system mass as follows:

$$m = \frac{R \cdot P_y}{S_a} = \frac{(8)(350\,\text{kip})}{32.2\,\frac{\text{ft}}{\text{s}^2}} = 87.0\,\frac{\text{kip}\cdot\text{s}^2}{\text{ft}} \tag{9.14}$$

The work point stiffness was calculated using equation 8.2, and the natural frequency was calculated using $\varpi_0 = \sqrt{\frac{K_{wp}\cos^2 45}{m}}$. The damping ratio was chosen to be 0.05.

In regards to input process properties, a filtered (Kanai-Tajimi) WN input was used in all random vibration analyses; ϖ_g and ξ_g are defined as in Section 7.2.3, and modulation function parameters $\Psi(t)$, γ_1, and γ_2 are defined as in Section 7.2.4. The magnitude Φ_0 of the white noise PSD was determined by scaling it such that, for a linear SDOF system subjected to a *non-filtered* (i.e. no KT filter) white noise of intensity $2\pi\Phi_0$, the mass absolute acceleration was equal to the design spectral acceleration S_a defined above. The purpose of this process was to determine an appropriate value for the input WN magnitude to correspond to the design spectral acceleration response. A non-filtered WN input was used in this case *only* instead of a filtered input simply for convenience, and was sufficient to determine an appropriate value of Φ_0. This was accomplished by constructing an SDOF system with a natural frequency equal to the elastic natural frequency of the BRBF system (ω_0) and with a damping ratio equal to that of the BRBF system (ξ_0). Again, the Matlab® toolbox Simulink® was used to generate time histories $a_{base}(t)$ and calculate the linear structure responses $\ddot{x}_a(t)$. The maximum value in each time history was recorded and averaged over all simulations to produce the mean maximum response $(\ddot{x}_a)_{\max}$. This process was repeated with different values of Φ_0 until $(\ddot{x}_a)_{\max} = S_a$. Simulation time length was 100 seconds, and 5 simulations were performed for each trial value of Φ_0. The value of Φ_0 corresponding to $(\ddot{x}_a)_{\max} = S_a$ was determined to be $\Phi_0 = 43.0\frac{\text{in}^2}{\text{s}^3}$.

9.4.2 Mean and Variance of Core Deformation Process

In this section, the distribution of the BRB core deformation process $u_c(t)$ is presented as calculated using the (1) ELM time varying Lyapunov solution, (2) ELM stationary Lyapunov solution, and (3) Monte Carlo simulation. The distribution of $u_c(t)$ is depicted by plotting its mean, mean + standard deviation, and mean – standard deviation. Result figures represent the following cases:

- Figure 9.1: Linear system subjected to a stationary WN input process. ($\Psi(t) = 1$, and the system is made linear-elastic by setting $\alpha = 1$.)
- Figure 9.2: Original nonlinear system subjected to a stationary WN input ($\Psi(t) = 1$ and $\alpha = 0.025$)
- Figure 9.3: Original nonlinear system subjected to a non-stationary WN input process ($\Psi(t) = \gamma_1 te^{-\gamma_2 t}$ and $\alpha = 0.025$)

Note that, for the Monte Carlo simulations, the number of process realizations used in ensemble calculations is denoted by n_{sim} in the figures.

Through comparison of the behavior shown by each solution method in each of the three cases above, the following conclusions were made:

1) The overall performance of the ELM, both the time-varying and stationary solution, is good, because it generally matches the simulation results throughout the time records.

2) The zero mean assumption for response variables is confirmed.

3) For the ELM non-stationary case (Figure 9.3), the stationary Lyapunov solution is not capable of producing the correct non-stationary results, as expected.

4) The variance of the BRB core deformation is greater for the nonlinear system as compared to the linear system. This is logical, as the behavior of the nonlinear system is likely more uncertain because the behavior of the BRB is a function of its past behavior.

While simulation results may not be considered exact, as the number of realizations is increased (say from 200 to 1000), the smoothness of the simulation response should increase. This can be observed by comparing the simulation results from Figure 9.2 and Figure 9.3 (200 simulations used) to the results in Figure 9.1 (500 simulations). The size of the oscillations in the simulation results is smaller for the case where 500 simulations were used. Using a larger number of simulations should cause the simulation and ELM results to match more closely.

9.4.3 Response Variable Normality

One assumption of the ELM is that the distribution of the nonlinear response variables is close to normal. To investigate this assumption, the Kolmogorov-Smirnov (KS) parameter [43] was calculated for the distribution of $u_c(t)$ at each point in time. (Note: The response variable *x* also exhibited the behavior described below.) This was performed for the nonlinear system subjected to the non-stationary white noise input. The KS test parameter here is defined as the maximum difference between the empirical cumulative distribution function (CDF) of $u_c(t_i)$ from the simulation and a CDF for a normal distribution with a mean of zero and a standard deviation of $\sigma_{u_c}(t_i)$; the time-varying Lyapunov equation solution was used to determine $\sigma_{u_c}(t_i)$. The KS test parameter is plotted versus time in Figure 9.4, and the normal probability plot of $u_c(20s)$ is presented in Figure 9.5.

The distribution depicted in Figure 9.5 is close to normal, but does show some significant skew toward the negative tail. This distribution may be considered typical for a KS parameter value around 0.07. Thus, from Figure 9.4, it may be said that the BRB core deformation process $u_c(t)$ is close to normal except for early in the time history (during the transient response).

While the response variables $x(t)$, $u(t)$, and $u_c(t)$ have close-to-normal distributions, the distribution of $z(t)$ (as calculated using Monte Carlo simulation) is clearly non-normal (see the normal probability plot of $z(20s)$ in Figure 9.6). The ELM assumes that $\dot{x}(t)$ and $z(t)$ are jointly normal for the *equivalent linear system*. As the Monte Carlo simulation is based on the unaltered nonlinear EOM, the process $z(t)$ as calculated from it may be different than that calculated using the equivalent linear system. There is no means by which to produce the distributions for $z(t)$ using the equivalent linear system, as the Lyapunov equations only give the covariance matrix of the response variables, and divulge no information about what type of distributions the responses follow.

9.4.4 Considerations for PBEF Framework

The methods developed for the random vibration analysis and the results were useful during the reliability analyses and parametric studies described in Chapter 10 and Chapter 11. For example, in order to determine which parameters needed to be considered in the analyses, the developed methods were used to investigate the effects of seismic loading, BRB, and BRBF system properties on the mean and variance of $u_c(t)$. Since the mean of $u_c(t)$ is zero and the variance is proportional to the imposed BRB deformation demands (as characterized by deformation descriptor terms such as μ_c and μ_{max}), the effect of BRB and BRBF properties on the variance is more important. The efficient ELM stationary Lyapunov solution was used to quickly calculate the variance (or standard deviation) of $u_c(t)$. Figure 9.7 and Figure 9.8 present example results that characterize the standard deviation of $u_c(t)$ versus values of KT filter damping ratio and core stiffness, respectively (all BRB, Bouc-Wen, BRB, and input process properties were the same as defined in Table 9.1, Table 9.2, Table 9.3, and Table 9.4 except for those varied in the specific cases.).

From Figure 9.7, it is clear that lowering the filter damping ratio increases the variance of the response variables. Therefore, site soil conditions do affect structure response noticeably, and it is important to accurately classify site characteristics. From Figure 9.8, it is apparent that increasing BRB stiffness (core stiffness in this case; transition region stiffness was set at 4 times core stiffness) reduces both interstory drift and BRB WP deformation; however, it increases floor acceleration. Thus, to design a BRBF effectively, the relative importance of each response variable would have to be quantified for a specific design situation, and the BRBF would need to be designed accordingly.

These observations and similar observations for other BRB, BRBF, and seismic loading properties helped determine which parameters to investigate in the parametric studies and fragility analyses described in Chapter 11. These tools were used to study the relative influence of various properties on the variance of the core deformation process. For example, it was determined that the influences of the ratio of non-core to core area and non-core to core length were much less than the influences of the core area and length on the BRB core deformation process. Further study of the parameter effects on

the core deformation process (in terms of system reliability effects) are discussed in Section 11.2

9.5 Random Vibration Analysis Summary and Conclusions

The equivalent linearization method (ELM) was used to perform random vibration analysis on an SDOF BRBF subjected to seismic forces. Initially, a prototype BRBF was developed based on average values from the BRB test database and based on design seismic forces from *SEI/ASCE 7-05* [32]. A Bouc-Wen model was used to model BRB hysteric behavior, and input ground accelerations were modeled as a filtered white noise excitation (using a Kanai-Tajimi filter); the excitations were modulated to account for non-stationary of earthquake ground motions.

Next, the ELM was employed to linearize the equations of motion, and two linear vibration analysis methods, the stationary Lyapunov equation and the non-stationary Lyapunov equation, were used to find the variance of the BRB core deformation process. In addition, Monte Carlo simulation was performed using the full non-linear EOM. It was found that results from both ELM methods match the Monte Carlo simulation results well. In addition, the distribution of $u_c(t)$ was shown to be close to normal except for during the transient response of the system.

The methods and results of the random vibration analysis were used to inform the reliability analyses and parametric studies described in Chapter 11. Specifically, the effects of BRB and BRBF properties on the mean and variance of the core deformation process were investigated. Since the variance of the core deformation process was more important than the mean, the variation of the standard deviation response with respect to BRB and BRBF properties was more close investigated.

9.6 Chapter 9 Figures

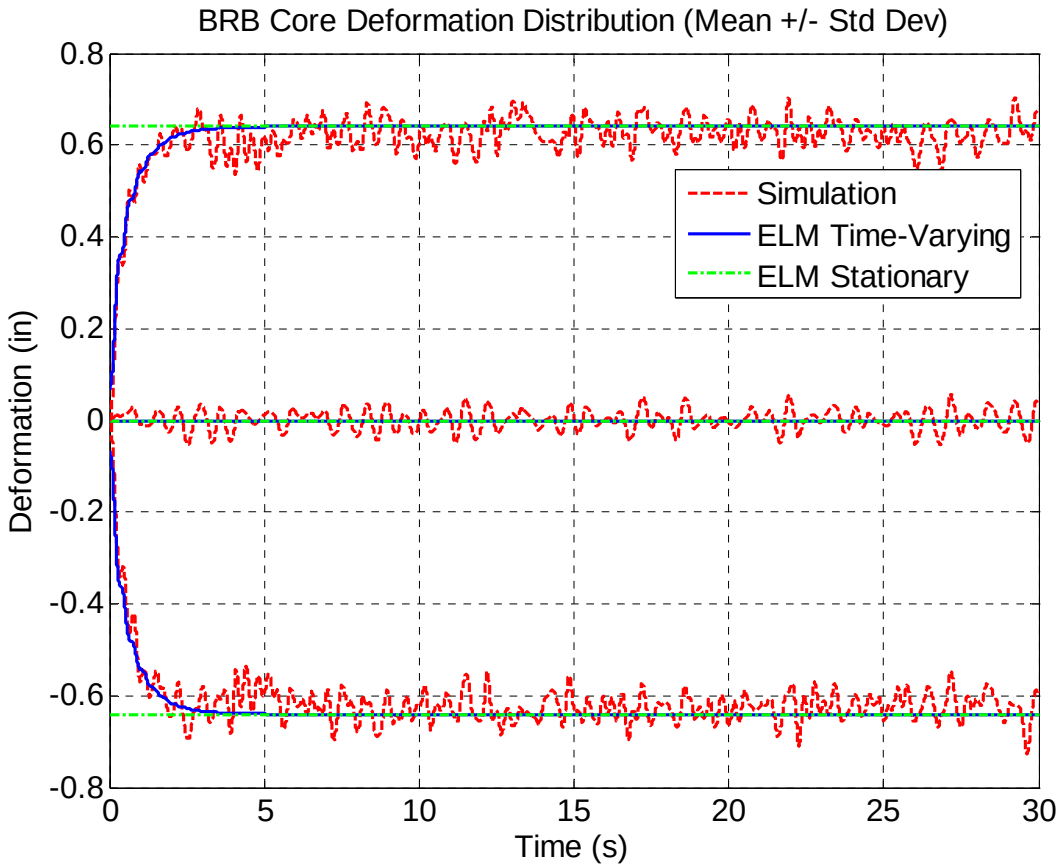

Figure 9.1: Linear System with Stationary White Noise Input ($n_{sim} = 500$)

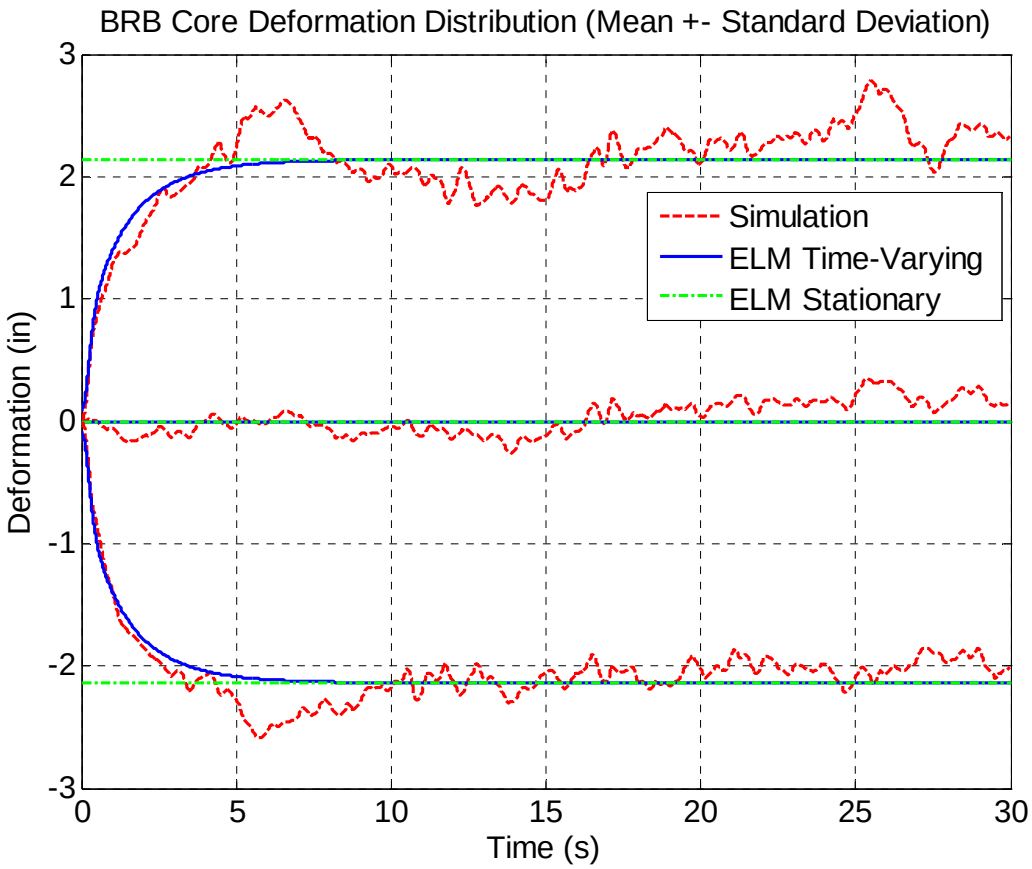

Figure 9.2: Nonlinear System with Stationary White Noise Input ($n_{sim} = 200$)

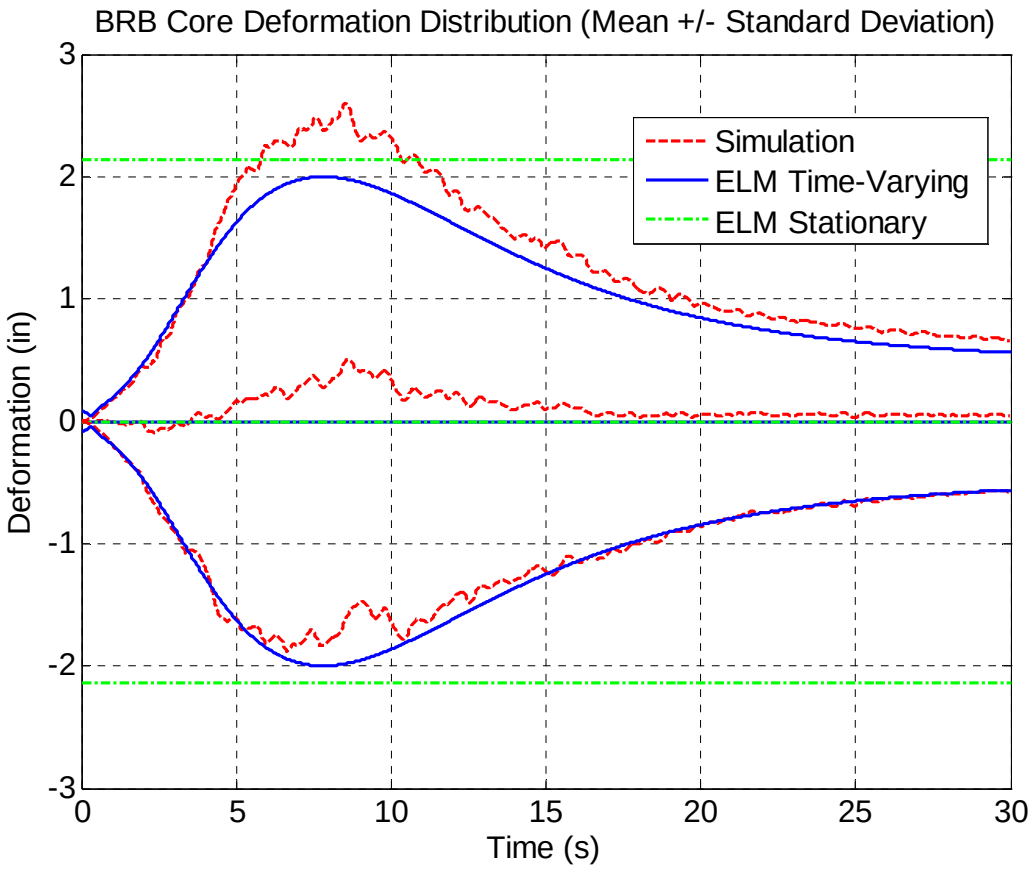

Figure 9.3: Nonlinear System with Non-stationary White Noise Input ($n_{sim} = 200$)

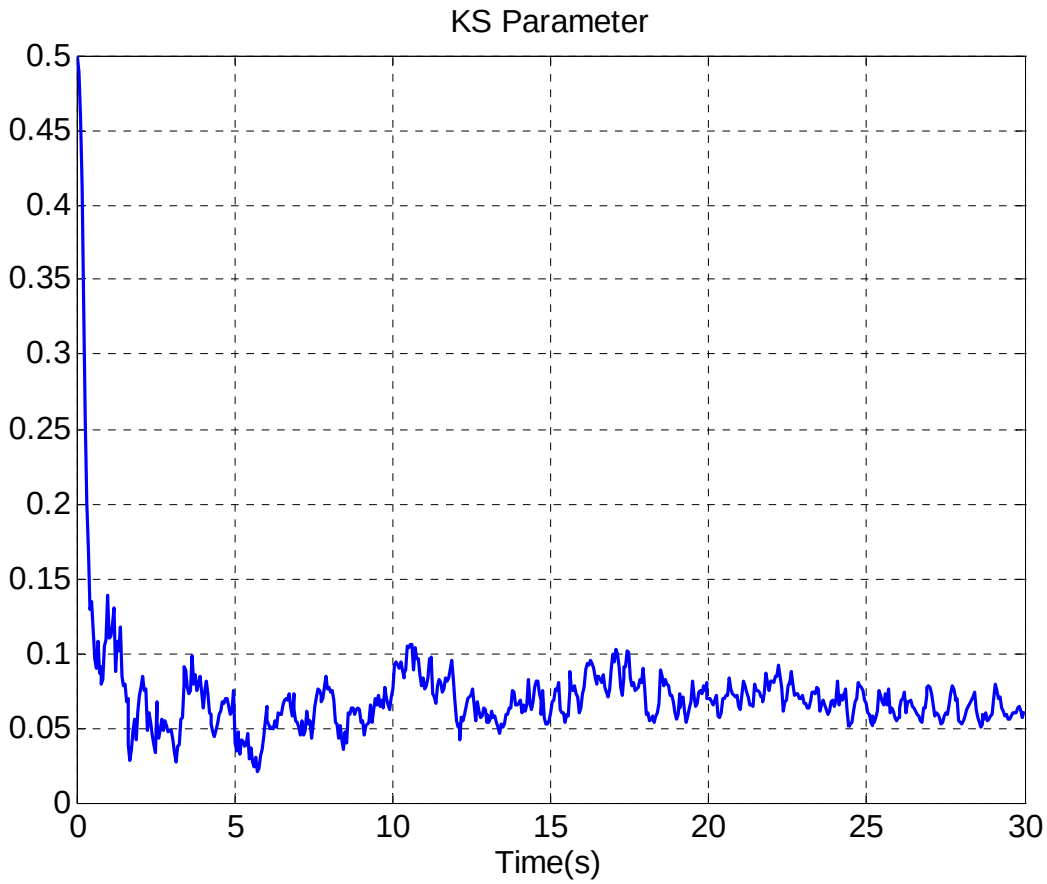

Figure 9.4: Kolmogorov-Smirnov Parameter for $u_c(t)$

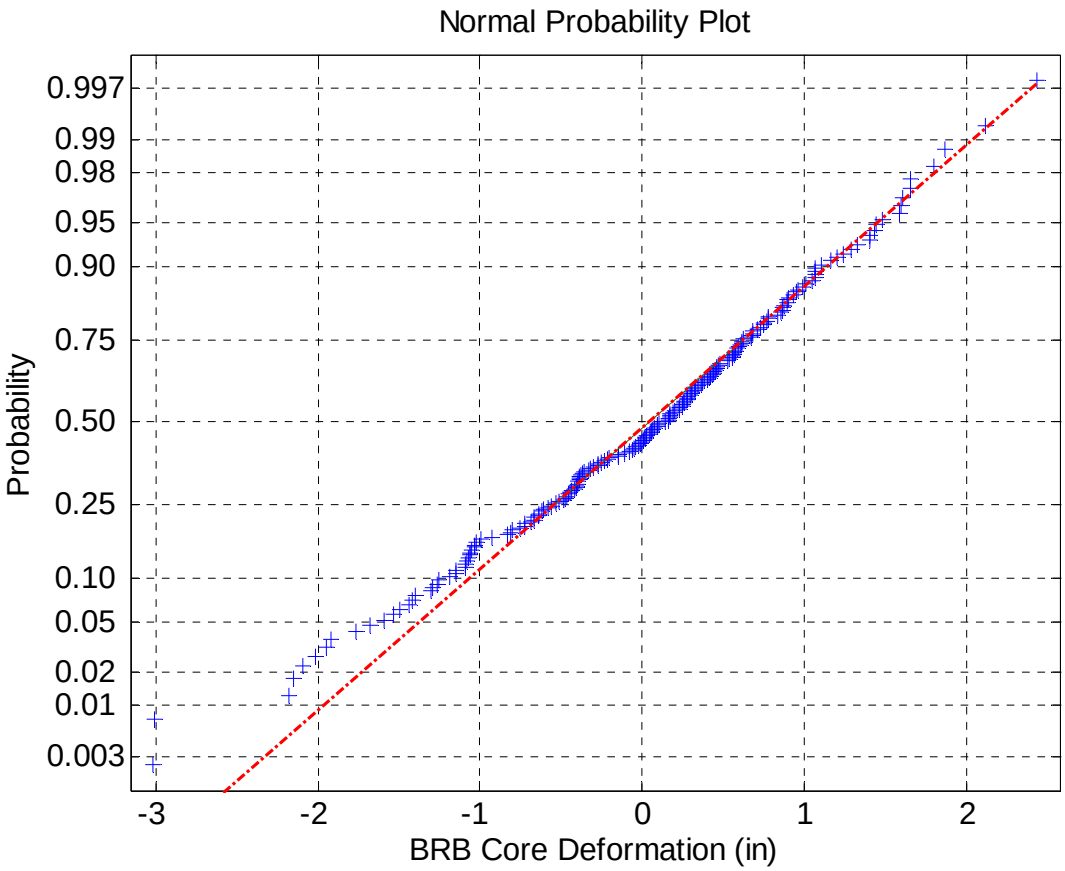

Figure 9.5: Normal Probability Plot of $u_c(20s)$

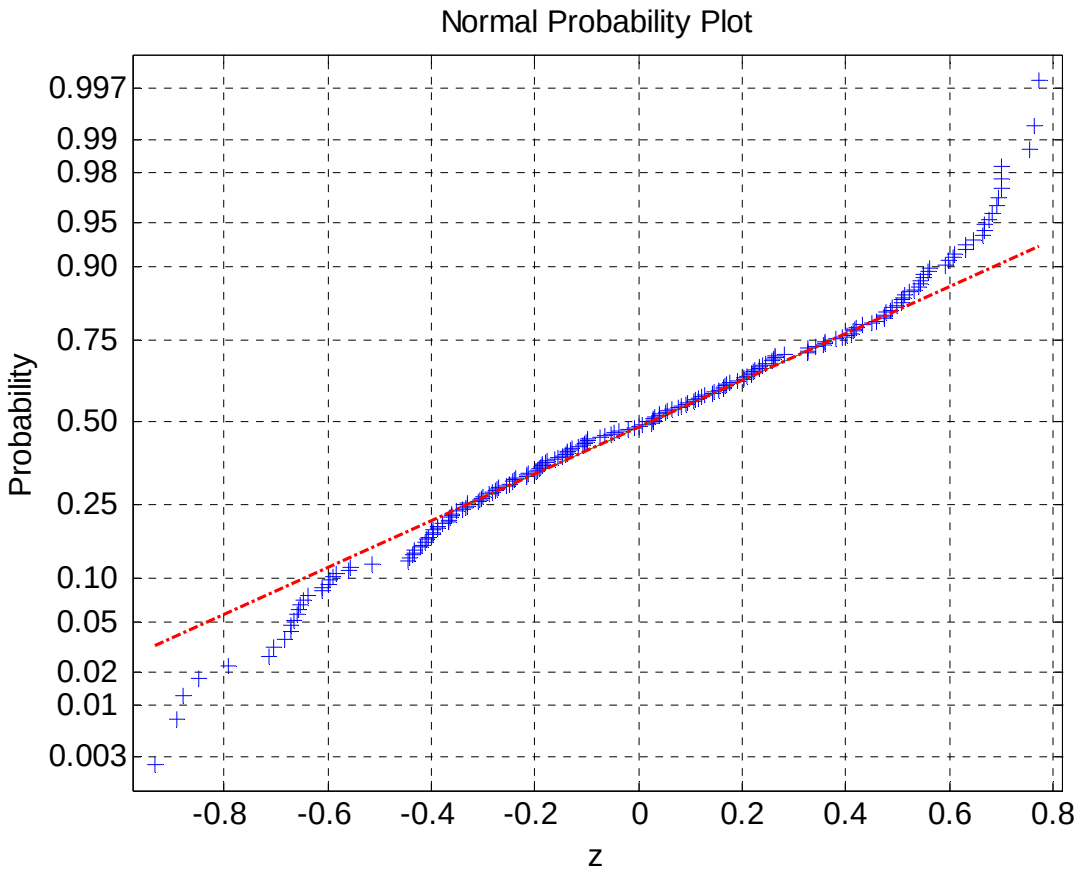

Figure 9.6: Normal Probability Plot of $z(20s)$

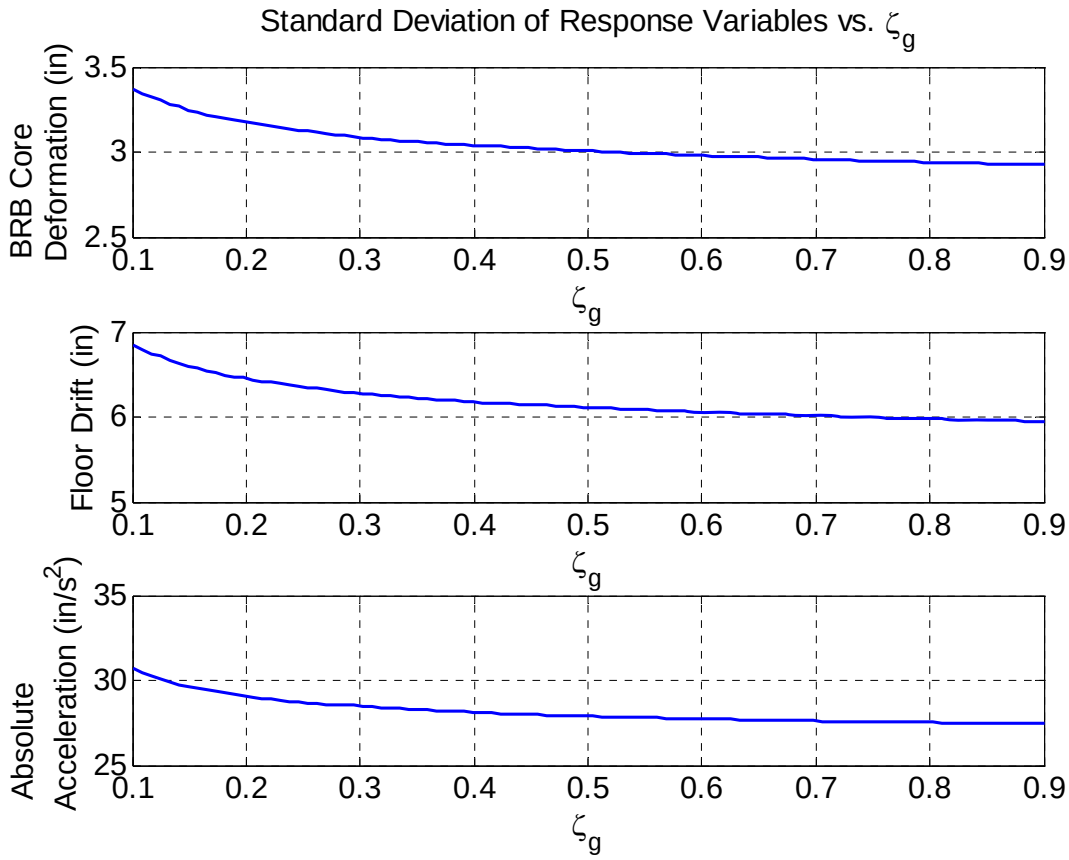

Figure 9.7: Response Variable Standard Deviation versus KT Filter Damping Ratio (ζ_g)

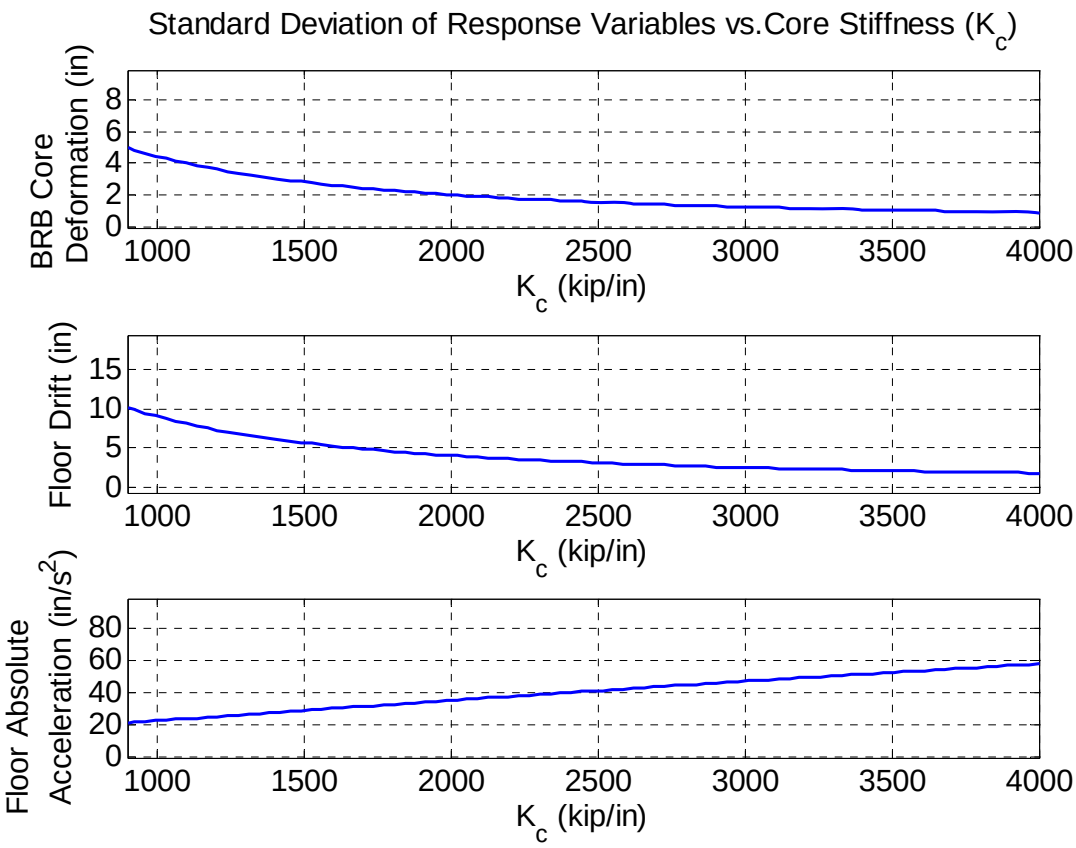

Figure 9.8: Response Variable Standard Deviation versus Core Stiffness

9.7 Chapter 9 Tables

Table 9.1: BRB Properties

Property	Variable	Value
Core Area	A_c	8.3 in^2
Core Length	L_c	10.61 ft
Non-Core Area	A_{nc}	16.6 in^2
Non-Core Length	L_{nc}	5.30 ft
Core Yield Force	P_y	350 kip
Elastic Modulus	E	29,000 ksi

Table 9.2: Bouc-Wen Model Properties

α	u_y	γ_{BW}	β_{BW}	n
0.025	0.348 in	0.45	0.55	1

Table 9.3: BRBF Properties

ω_0	ξ_0	m	K_{wp}
$13.2\frac{\text{rad}}{\text{s}}$	0.05	$87.0\frac{\text{kip}\cdot\text{s}^2}{\text{ft}}$	$1260\frac{\text{kip}}{\text{in}}$

Table 9.4: Input Process Properties

Φ_0	$43.0\frac{\text{in}^2}{\text{s}^3}$
ω_g	$5\pi\frac{\text{rad}}{\text{s}}$
ξ_g	0.60
$\psi(t)$	$\gamma_1 t e^{-\gamma_2 t}$
γ_1	0.45
γ_2	$1/6$

Chapter 10

CAPACITY MODELS AND RELIABILITY ANALYSES

10.1 Overview

The goal of the reliability analysis within the PBEF (as shown in Figure 1.4) is to calculate the probability of brace failure based on the developed capacity models (Chapter 6) and the structural demands estimated by nonlinear dynamic simulation (Chapter 8). In general, probability of brace failure (P_f) may be calculated as a function of a vector of observable variables $\mathbf{x}$ and a subset of their outcome space that defines a failure event. The probability of failure is calculated using the following *n*-fold integral:

$$P_f = \int_{\Omega} f(\mathbf{x}) d\mathbf{x} \tag{10.1}$$

where $f(\mathbf{x})$ is the joint probability density function (PDF) of $\mathbf{x}$, and Ω is the failure domain. The failure domain Ω is defined by use of a limit state function $g(\mathbf{x})$, i.e. $g(\mathbf{x}) \leq 0$ indicates that $\mathbf{x}$ is in Ω. In this research, the limit state function $g(\mathbf{x})$ is given by the equations for remaining capacity (Chapter 6) in which the vector of observable variables $\mathbf{x}$ is defined by capacity model parameters described in Chapter 3. BRB property parameters were considered deterministic while deformation descriptor parameters were considered random variables, because the variability in the BRB property parameters was much smaller than the variability in the deformation parameters.

When many random variables are present in $\mathbf{x}$, the integral given by equation 10.1 can be difficult and time consuming to solve. First and second order reliability methods may be used to approximate the solution to this integral. In this research, the first order reliability method (FORM) [26] was used.

The steps to perform the reliability analysis were as follows:

1) Extract deformation descriptor parameters μ_c, $\mu_{\max}$ and $\mu_{\max loc}$ from the nonlinear dynamic simulation

2) Fit analytical distribution functions to the empirical distributions of μ_c, $\mu_{\max}$ and $\mu_{\max loc}$; combine these distributions with the deterministic BRB property parameters to construct the vector of parameters $\mathbf{x}$

3) Extract the limit state function $g(\mathbf{x})$ (i.e. remaining capacity function) from the appropriate capacity model described in Chapter 6

4) Given $\mathbf{x}$ from Step 2 and $g(\mathbf{x})$ from Step 4, perform a reliability analysis using FORM to calculate the probability of brace failure

Each step is described in detail in the sections that follow.

10.2 Step 1: Deformation Descriptor Terms

For reliability analyses, the probabilistic distributions of uncertain deformation descriptors in $\mathbf{x}$, i.e. μ_c, $\mu_{\max}$ and $\mu_{\max loc}$, must be known. These terms were produced as outputs from the nonlinear dynamic simulation and deformation descriptor calculations described in Sections 8.4 and 8.5. A single value for each term was produced from each simulation. To find the distribution of each term, multiple simulations must be performed to produce random samples generated according to the probabilistic distribution of basic random variables.

An analysis was performed to determine the number of simulations that must be run to adequately characterize the distributions of μ_c, $\mu_{\max}$ and $\mu_{\max loc}$ (see Matlab® code in Appendix D). Multiple simulations were performed using the BRB and BRBF properties defined in Section 9.4.1. The mean and standard deviation of the empirical distributions of μ_c, $\mu_{\max}$ and $\mu_{\max loc}$ were calculated as a function of the number of simulations performed. Results are summarized in Figure 10.1, Figure 10.2, and Figure 10.3. From the figures, it was apparent that at least 50 simulations were required for the mean and standard deviation of μ_c and $\mu_{\max}$ to converge, whereas at least 70 simulations were required for convergence of $\mu_{\max loc}$. Therefore, 70 simulations were performed to determine the distributions of μ_c, $\mu_{\max}$ and $\mu_{\max loc}$ for the reliability analyses. These 70 simulations produced 70 parameter values that composed the empirical distribution for each term; and these distributions were then fit with analytical PDFs, as described below. Note that it is necessary to use more simulations for rigorous distribution fitting, but in this research the number of simulations was limited to 70 to limit the simulation time required.

10.3 Step 2: Distribution Fitting

After creation of empirical distributions (70 observations) of μ_c, $\mu_{\max}$, and $\mu_{\max loc}$ in Step 1, analytical PDFs were fitted to these distributions in Step 2. This was accomplished using statistical tools in the "dfittool" command in Matlab®, which help fit specified PDFs to the empirical distributions so as to minimize the difference between the empirical and analytical distributions. The quality of fitting was determined by evaluating a "likelihood" metric generated by the dfittool command. This likelihood metric is very similar to the likelihood function described in previous chapters, and it measures the quality of fit over the entire range of the distribution. The distribution form that produced the highest value of likelihood was identified as the best fitting. After comparison of the empirical distributions with various analytical distribution forms (e.g. normal, lognormal, Weibull, etc.), it was found that lognormal distribution best fits μ_c and $\mu_{\max}$, while Weibull provides the best match for $\mu_{\max loc}$. Figure 10.4, Figure 10.6, and Figure 10.8 show example empirical distributions and fitted PDFs for μ_c, $\mu_{\max}$ and $\mu_{\max loc}$ respectively. Figure 10.5, Figure 10.7, and Figure 10.9 show example empirical CDFs and fitted CDFs for μ_c, $\mu_{\max}$ and $\mu_{\max loc}$, respectively. After determining which

analytical distribution form best fitted the empirical distribution for each random variable, the distribution form was used to fit all subsequent empirical distributions from simulation for that variable. This was accomplished in an automated means in Matlab® code by using the "lognfit" and "wblfit" commands (see Matlab® code in Appendix D). These commands provided the statistical parameters required to completely define the analytical distributions.

10.4 Step 3: Define Limit State Function

The limit state function $g(\mathbf{x})$ was defined from the remaining capacity models such that $g(\mathbf{x}) = RC(\mathbf{h}, \boldsymbol{\theta}) \leq 0$ defined failure of the brace, where the general form the of the remaining capacity models is as follows:

$$RC = TC - UC + \sigma\varepsilon$$
$$RC = \prod_{i=1}^{m} h_i^{\theta_i} - \sum_{i=m+1}^{n} h_i \theta_i + \sigma\varepsilon \tag{10.2}$$

where $\mathbf{h}$ is a vector of predictor parameters (BRB properties and deformation descriptor parameters from Chapter 3); $\boldsymbol{\theta}$ is a vector of model parameters; and $\sigma\varepsilon$ represents the model error (see Chapter 4 for more information). Specific values of $\mathbf{h}$, $\boldsymbol{\theta}$, and σ used in the parametric studies and fragility analyses are given in Chapter 11.

10.5 Step 4: First Order Reliability Analysis

The FORM was used to calculate an approximate solution to equation 10.1 to give the probability of brace failure. A brief summary of the method and its application to this research is given here; for detailed derivations, see [26].

First, the original random variables in $\mathbf{x}$ are transformed into uncorrelated standard normal random variables $\mathbf{u}$ through a transformation $\mathbf{u} = \mathbf{T}(\mathbf{x})$. Then, using a nonlinear constrained optimization algorithm, one can obtain the point on the limit-state surface $G(\mathbf{u}) = g(\mathbf{x}(\mathbf{u})) = 0$ that is nearest to the origin of the $\mathbf{u}$-space. At this "design point" [26], the limit-state function is linearized, and the probability integral in equation 10.1 is approximately evaluated by the probability in the half-space determined by the linearized limit-state function:

$$P_f \cong \Phi(-\beta) \tag{10.3}$$

where Φ is the standard normal cumulative distribution function, and β is the distance from the origin to the design point, often referred to as "reliability index." The reliability index β is often used as a relative measure of the reliability of structural components or systems.

The limit state function defined generally by equation 10.2 contains uncertainty due to the capacity model error $\sigma\varepsilon$ in which σ determines the magnitude of the model error quantified by the MLE method, and ε is the standard normal random variable. Therefore, the uncertainty in the random variable ε is propagated to the reliability index

evaluated by the FORM analysis. In order to provide the quantified confidence of the estimated reliability index based on this model error, the first order approximation of the mean and variance of $\beta(\varepsilon)$ are obtained as

$$\mu_\beta \cong \beta(\mu_\varepsilon) = \beta(0) \tag{10.4}$$

$$\sigma_\beta^2 \cong \left(\left. \frac{\partial \beta}{\partial \varepsilon} \right|_{\varepsilon=0} \right) \sigma_\varepsilon^2 = \left(\left. \frac{\partial \beta}{\partial \varepsilon} \right|_{\varepsilon=0} \right)^2 \tag{10.5}$$

where μ and σ respectively denote the mean and standard deviation of the corresponding random variable; $\beta(0)$ means the reliability index evaluated by FORM with ε fixed as zero; and the sensitivity of the reliability index with respect to ε is obtained as:

$$\frac{\partial \beta}{\partial \varepsilon} = \frac{1}{\left\| \nabla G(\mathbf{u}^*; \varepsilon) \right\|} \frac{\partial g\left(\mathbf{x}^*; \varepsilon\right)}{\partial \varepsilon} \tag{10.6}$$

where $\mathbf{x}^*$ and $\mathbf{u}^*$ are the design points in the original and standard normal space, respectively. This sensitivity was obtained by use of the open-source software Finite Element Reliability using Matlab® (FERUM) [27].

Assuming $\beta(\varepsilon)$ follows a normal distribution with mean μ_β and standard deviation σ_β, the *p*-percentile (i.e. the value of a random variable below which *p* % of the observations fall) of the reliability index is obtained as

$$\beta_p = \mu_\beta + k_p \sigma_\beta \tag{10.7}$$

where k_p is the *p*-percentile of the standard normal random variable.

In particular, the following percentiles were obtained in this research:

- $\beta_{50} = \mu_\beta$
- $\beta_{10} = \beta_{50} - 1.28 \frac{\partial \beta}{\partial \varepsilon}$
- $\beta_5 = \beta_{50} - 1.65 \frac{\partial \beta}{\partial \varepsilon}$

These reliability indices read as presented in Table 10.1.

For a more conservative estimate of system reliability, reliability values with lower *p*-percentile values would be used, whereas for a less conservative estimate, higher values would be used. β_{50} provides an average value of reliability. In addition, the magnitude of the differences between the reliability indices above is proportional to the value of σ. If $\sigma = 0$, then the value of β is deterministic. More accurate RC models

(those with smaller σ) provide the ability to avoid unnecessary conservatism in evaluating brace reliability.

The reliability analysis by FORM was performed using FERUM [27]. While the open source code provides additional tools for finite element analysis, only the general FORM tool was used in this analysis to perform reliability analyses with a user-defined limit-state function (See the Matlab® code in Appendix D). Three inputs were required to use FERUM:

1) The limit state function $g(\mathbf{x})$

2) Analytical distribution parameters for the random variables in $\mathbf{x}$

3) Quantification of the uncertainty in $g(\mathbf{x})$ (i.e. model error)

The limit state function $g(\mathbf{x})$ was defined by the RC model as shown in equation 10.2; computation of the analytical distribution parameters for the three random variables in the RC model (i.e. μ_c, $\mu_{\max}$, and $\mu_{\max loc}$) was described in Section 10.3; and the uncertainty in $g(\mathbf{x})$ was characterized by the value of σ associated with the RC model. Using these inputs, the FERUM code calculates values of β_{50}, β_{10}, and β_5.

10.6 Chapter 10 Figures

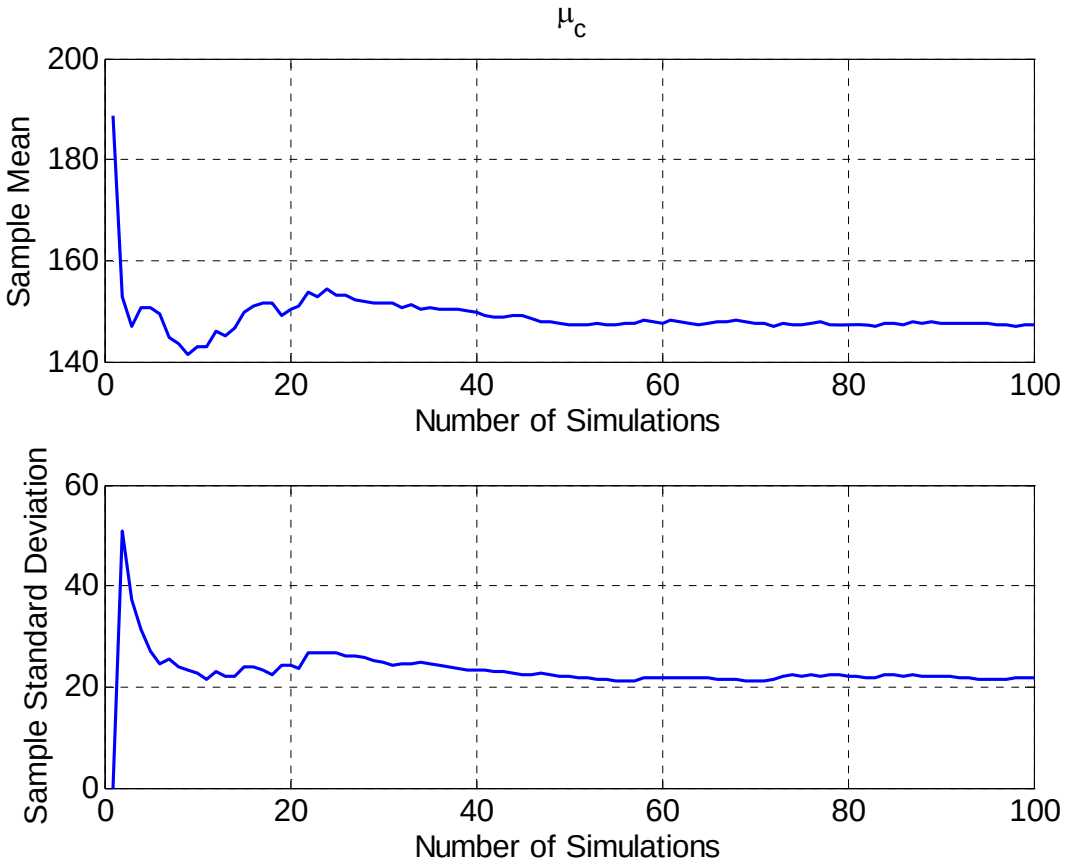

Figure 10.1: Number of Simulations Required for Convergence of μ_c

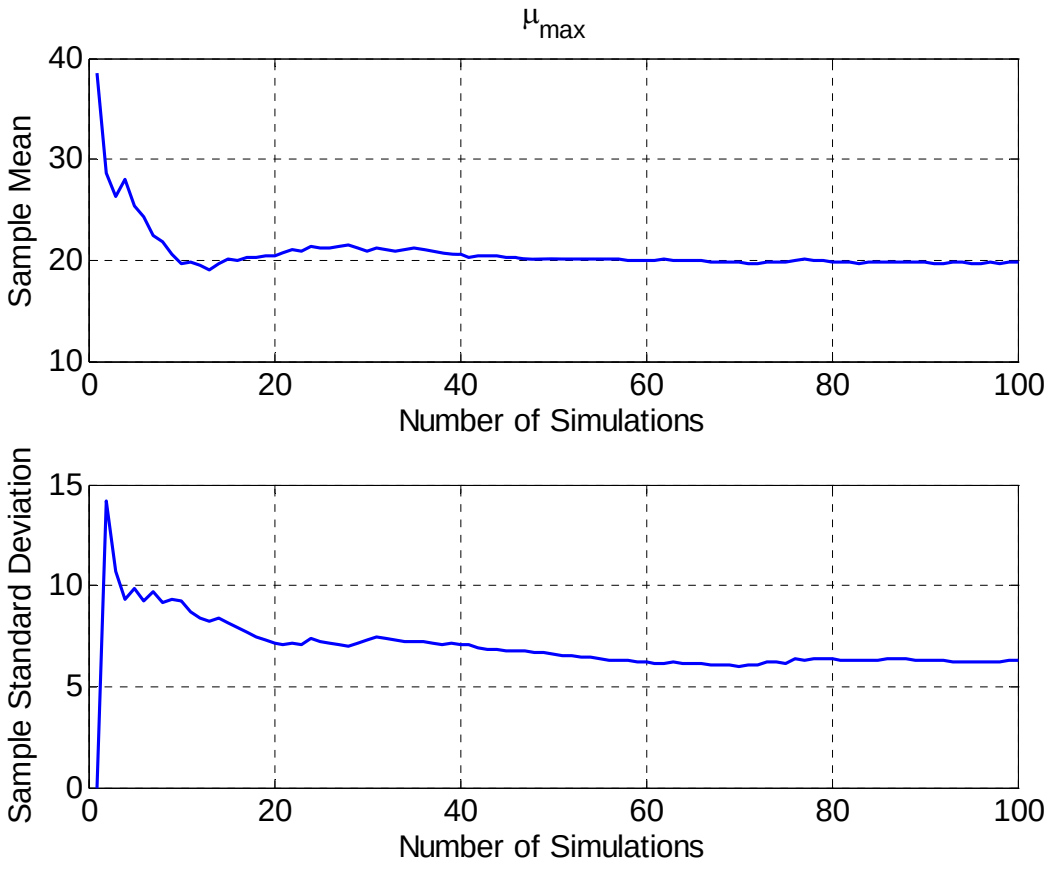

Figure 10.2: Number of Simulations Required for Convergence of μ_{max}

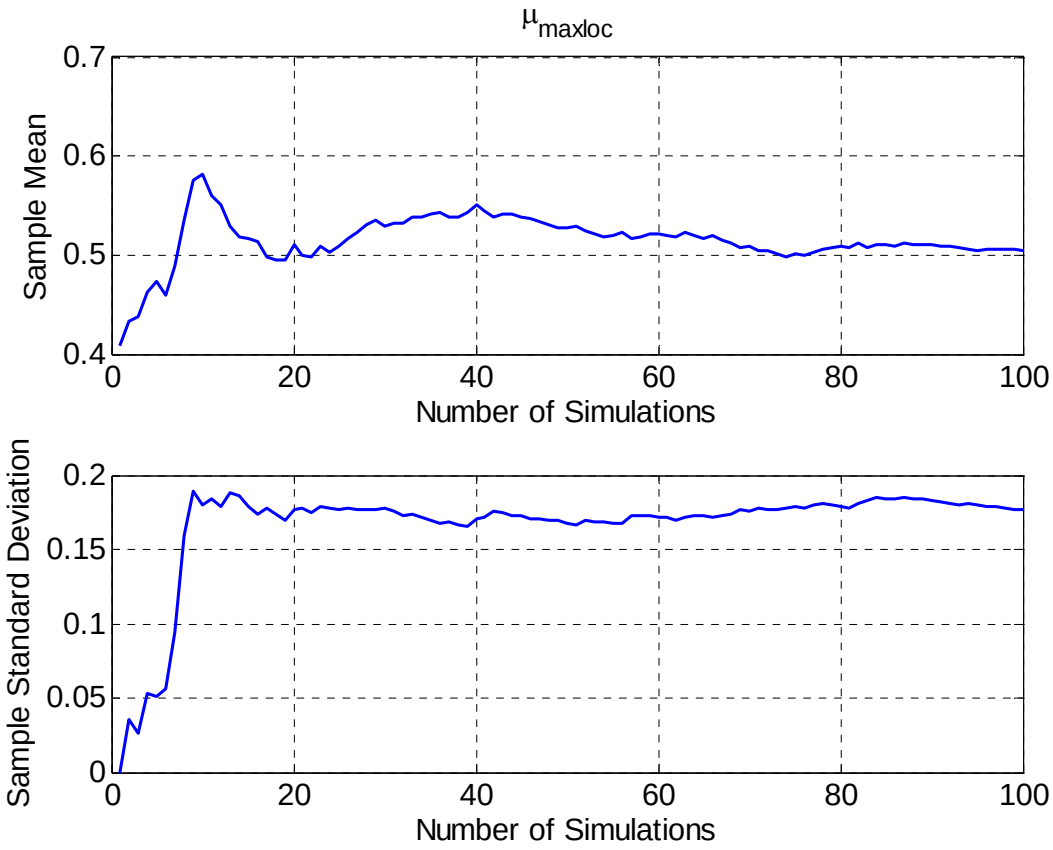

Figure 10.3: Number of Simulations Required for Convergence of $\mu_{\max loc}$

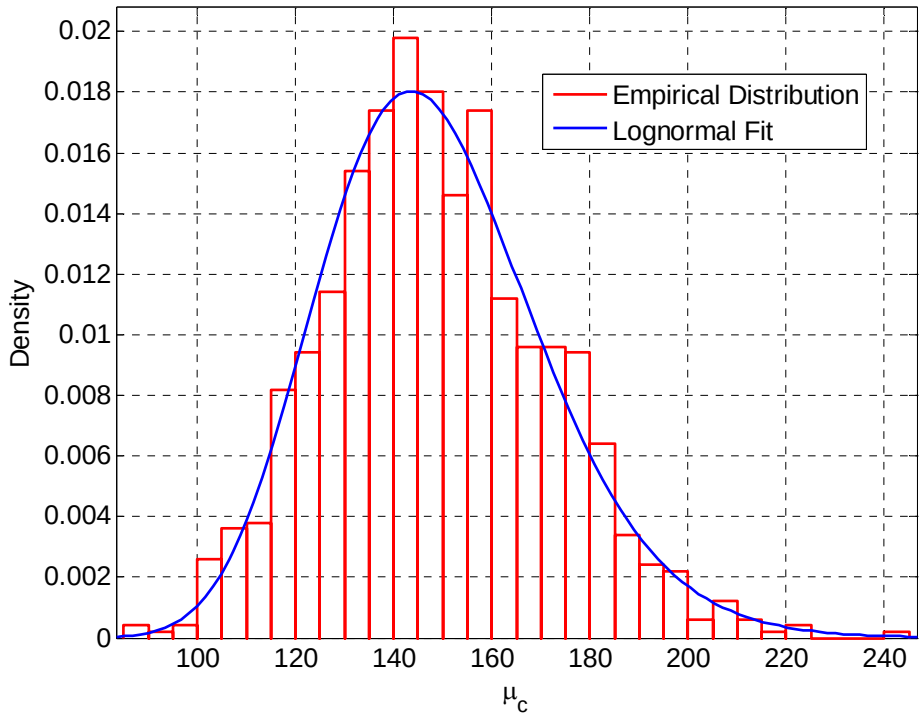

Figure 10.4: μ_c **PDF Fit**

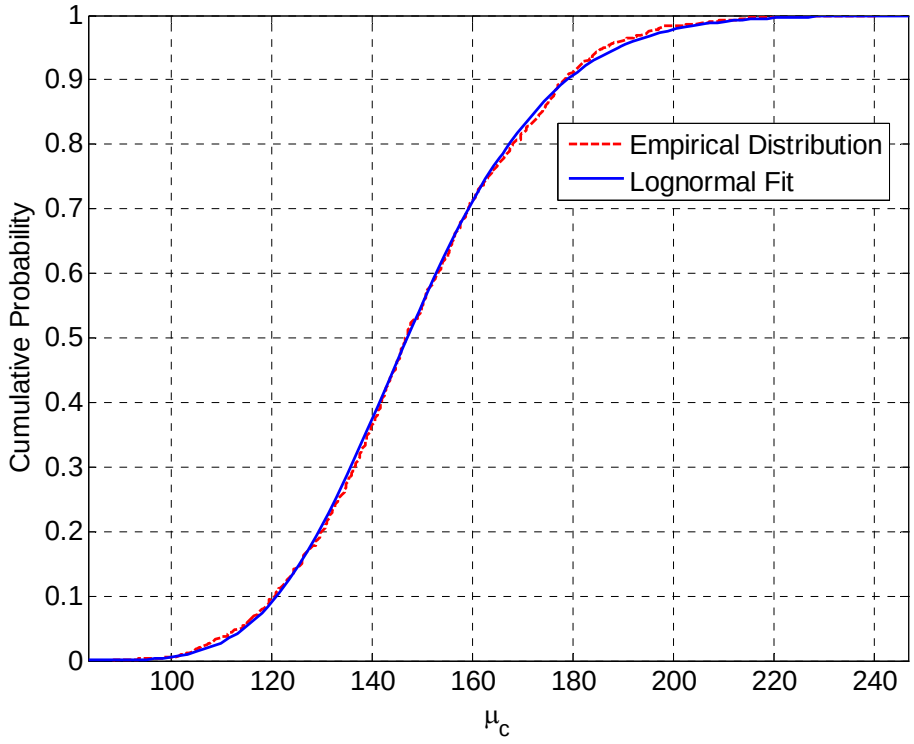

Figure 10.5: μ_c **CDF Fit**

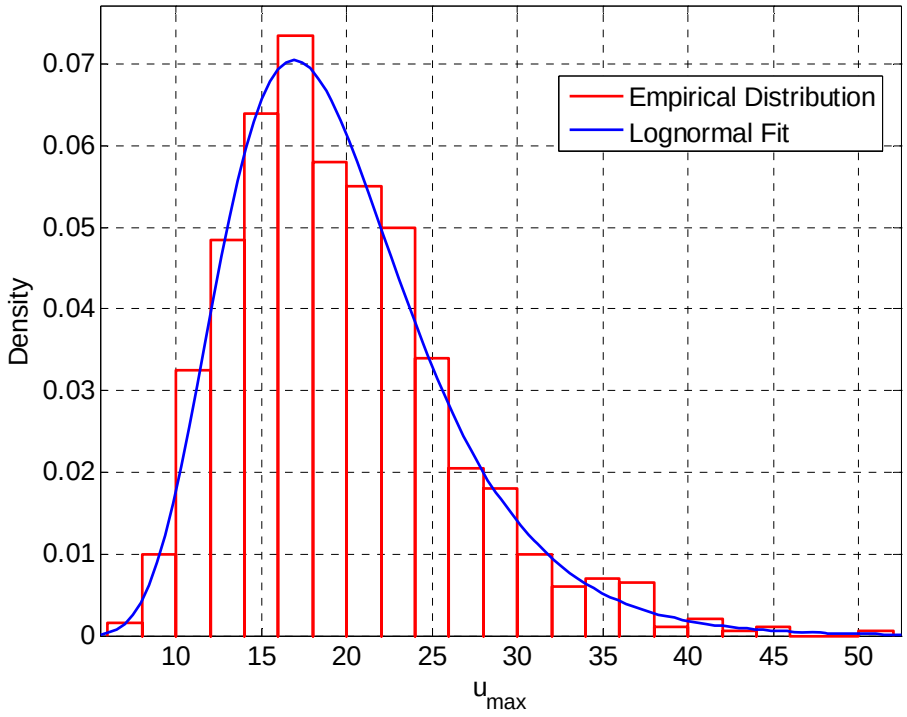

Figure 10.6: μ_{max} **PDF Fit**

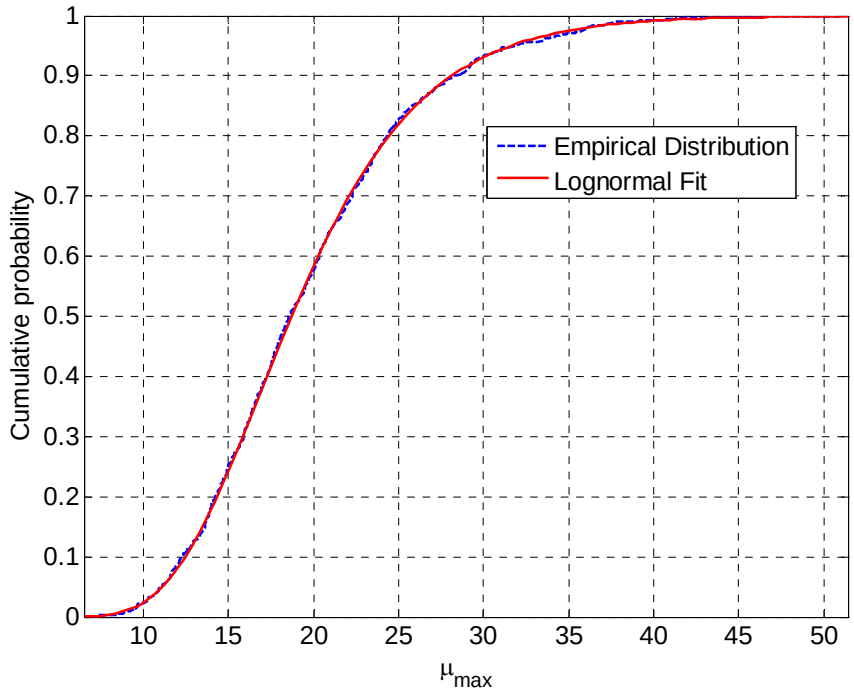

Figure 10.7: μ_{max} **CDF Fit**

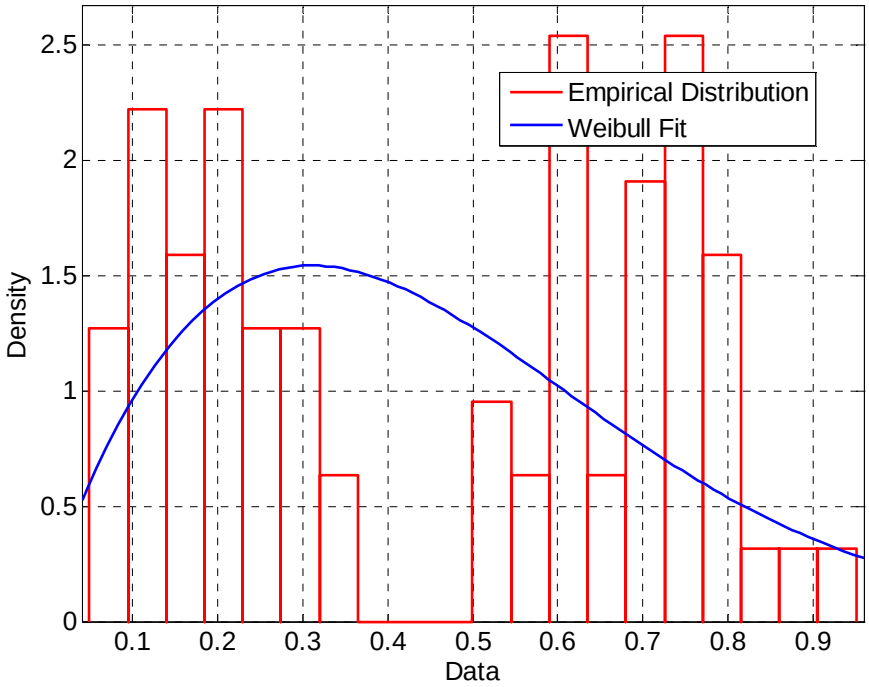

Figure 10.8: $\mu_{\max loc}$ **PDF Fit**

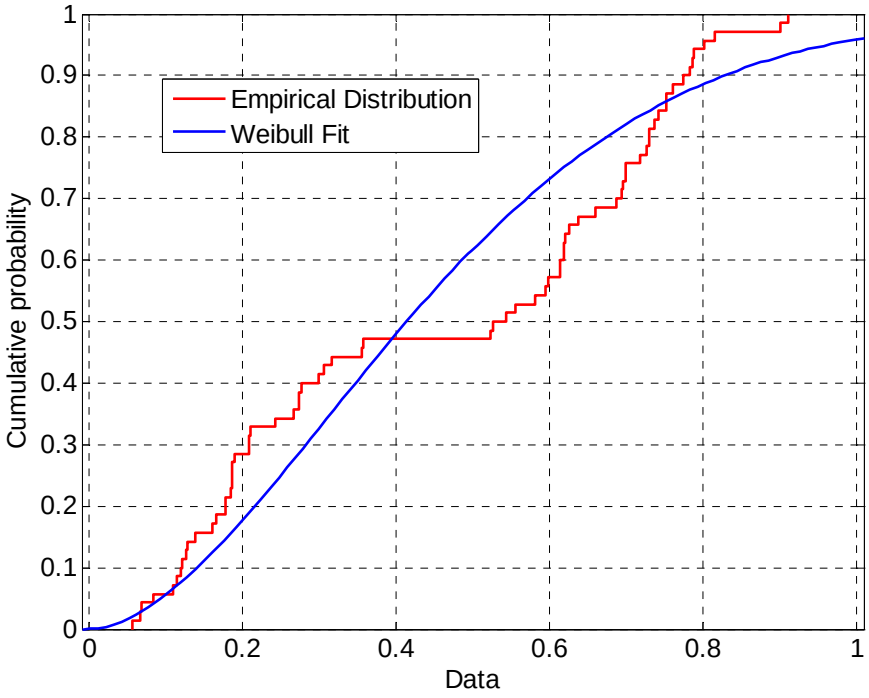

Figure 10.9: $\mu_{\max loc}$ **CDF Fit**

10.7 Chapter 10 Tables

Table 10.1: Reliability Indices Definitions

Parameter	Confidence Level	Probability that β will be observed below the Parameter	Probability that β will be observed above the Parameter
β_{50}	50%	50%	50%
β_{10}	90%	10%	90%
β_{5}	95%	5%	95%

Chapter 11

PARAMETRIC STUDIES AND FRAGILITY ANALYSES

11.1 Overview

While Chapters 7, 8, and 0 provide the overall framework and background for the PBEF, this chapter describes the use of the framework and methods to evaluate system reliability and to investigate parameter effects on system reliability. This chapter describes the following:

- Parameter Analysis – An analysis investigating which parameters affect system reliability.
- Parametric Studies – Studies which quantify system reliability as a function of important parameters (i.e. BRB, BRBF, and seismic loading properties); these studies are performed using various RC models.
- Fragility Analysis – Fragility analyses which produce curves of probability of BRB failure versus ground shaking intensity for given BRB and BRBF properties.
- Conclusions and Applications – A summary of the results from this chapter, lessons learned, and outlook toward potential applications of the PBEF.

11.2 Parameter Analysis

A parameter analysis was performed wherein the most important parameters affecting system reliability were identified. The purpose of this analysis was to reduce the number of parameters considered in the parametric studies. As part of this effort, after identification of the most important parameters, these parameters were utilized in an attempt to create non-dimensional terms that aptly characterize BRB and BRBF behavior.

11.2.1 Determination of Most Important Parameters

The complete list of possibly important parameters, which includes BRB, BRBF, and seismic loading properties, is given in Table 11.1. This list of all parameters was reduced to those important for consideration as follows: First, typical parameter values were assumed for the steel modulus of elasticity and structure damping ratio as $E = 29{,}000ksi$ and $\xi_0 = 0.05$. Second, because of the complexity involved in investigating the effects of earthquake stationarity and duration, values of the modulation function and its parameters were assumed as $\Psi(t) = \gamma_1 t e^{-\gamma_2 t}$, $\gamma_1 = 0.45$ and $\gamma_2 = 1/6$ (as explained in Section 7.2.4). Third, the parameters A_{nc} and L_{nc} were set as a function of parameters A_c and L_c. A_{nc} was set as 2 times A_c, and L_{nc} was set such that the total length of the BRB was

21.2 feet ($21.2' = L_c + 2L_{nc}$), as shown in the BRBF structural model (Figure 8.1). Also, these parameters do not influence ductility capacity based on the RC models developed in Chapter 6. The remaining parameters not mentioned above were the primary ones considered in the parametric studies. Table 11.2 summarizes the classification of parameters.

11.2.2 Non-Dimensional Terms

As a precursor to the parametric studies, non-dimensional terms constructed of those parameters listed in Table 11.1 were investigated. The goal of these investigations was to reduce the number of independent terms in the parametric studies to two. After some investigation, the best two non-dimensional terms were identified as:

- Non Dim 1: $\frac{P_y}{m \cdot S_a}$
- Non Dim 2: $\frac{L_c}{S_a \cdot {t_{EQ}}^2}$

where all terms are as defined previously, except that S_a is the actual mean spectral acceleration from the non-linear dynamic analyses (of which 70 simulations were performed to find the mean spectral acceleration), and t_{EQ} is the seismic loading duration, which, for a specific ground acceleration record, was defined as all that time where the ground acceleration was greater than 0.02 times the peak ground acceleration of the record.

The term Non Dim 1 accounts explicitly for A_c, F_y and m, and indirectly accounts for Φ_0, ϖ_g, and ζ_g through the use of S_a. Similarly, Non Dim 2 accounts for L_c and t_{EQ} explicitly.

Next, two analyses, named NON DIM A and NON DIM B, were performed to evaluate whether the terms Non Dim 1 and Non Dim 2 adequately describe BRB behavior. Table 11.3 and Table 11.4 describe the analysis configuration parameters for NON DIM A and NON DIM B, respectively. Different independent variables were varied in each analysis, but the results for each analysis were both quantified using terms Non Dim 1 and Non Dim 2. Figure 11.1 and Figure 11.2 present system reliability index β_{50} versus terms Non Dim 1 and Non Dim 2 for analysis NON DIM A and NON DIM B, respectively.

Comparing values from Figure 11.1 and Figure 11.2, it is obvious that analyses NON DIM A and NON DIM B produced different results. Not only are specific values of β_{50} different for each analysis, but the overall behavior with respect to the non-dimensional terms is different – the behavior of β_{50} varies with both non-dimensional terms in NON DIM B, but mostly with Non Dim 1 in analysis NON DIM A. Since the analyses produced different results, the two non-dimensional terms, by themselves, are not sufficient to characterize BRB behavior. Therefore, parametric studies must consider more individual parameters instead of two non-dimensional terms.

11.3 Parametric Studies

11.3.1 Methodology

Parametric studies were performed to investigate the influence of BRB, BRBF, and seismic loading properties on system reliability. As discussed in the previous section, while some parameters need not be considered in the parametric studies, there are still a significant number of parameters that must be considered, and Table 11.2 lists those terms to be varied directly. To account for these terms, reliability analyses were performed using Input Module 2 where parameters L_c, A_c, and m were varied directly while terms F_y, F_u and $(S_a)_{target}$ were held fixed. Then, this process was repeated with different values of F_y, F_u and $(S_a)_{target}$. If the results from all the analyses are compiled, they represent a complete set where all parameters are varied.

11.3.2 Presentation of Analysis Results

The following items were presented as primary results from the various analyses:

1) Contour plots of output variables versus A_c and L_c for given values of the other parameters (m, F_y, F_u, and $(S_a)_{target}$).

2) Acceleration spectrum plot for comparison of actual spectral acceleration versus $(S_a)_{target}$

3) Plots which compare results from the various analyses

Because the meaning or values of the parameter m are related to fundamental behavior (mass will vary depending on the size of the system being considered), in the analysis results, the parameter m was replaced with the parameter R, which is commonly known as the response modification coefficient [32] in the field of earthquake engineering. The parameter, which represents the force reduction taken in design and also is closely related to ductility demand, is defined as

$$R = \frac{m \cdot (S_a)_{target}}{P_y} \tag{11.1}$$

The primary output variable from each analysis was the mean reliability index β_{50}. Other output variables included:

- Percentile reliability indices β_{50}, β_{10}, and β_5;
- Distributions of μ_c, μ_{max} and $\mu_{max\,loc}$; and
- Predicted RC, TC and UC.

The primary output variable β_{50} is presented for all analyses performed, whereas the other parameters are presented selectively.

11.3.3 Analyses Performed

A wide variety of parametric study analyses were performed to investigate the influences of BRB, BRBF and seismic loading properties on system reliability. Certain parameters were defined the same in all parametric study analyses, and these are presented in Table 11.5. Of these parameters, certain parameters were constant in the analyses, and others varied between each reliability analysis. Those that were varied included L_c, A_c, and R; the domain of variation for L_c and A_c was set the same as the range of values from the BRB test database, whereas the domain of variation for R was set based on practicality. Those parameters which were defined differently in each parametric study analysis and which provided the variation between the analyses were: RC model used, $(S_a)_{target}$, t_{sim}, F_y, and F_u. Table 11.6 summarizes the suite of analyses performed and defines the parameters which were different for each parametric study analysis.

The analysis suite was configured to investigate the effects of different seismic events or sequences of seismic events, RC model effects, and different steel grades (Grade 36 and Grade 50). In the table, $(S_a)_{target}$ values represent different seismic events and sequences of seismic events, as follows:

- DBE: design basis earthquake (30 s)
- MCE: maximum considered earthquake (30 s)
- DBE-MCE: DBE followed by MCE (30s – 30s for 60 s total)
- MCE-DBE: MCE followed by DBE (30s – 30s for 60 s total)
- MCE-MCE: Two MCEs in a row (30s – 30s for 60 s total)

DBE and MCE are defined in *SEI/ASCE 7-05*. Each seismic event was 30 seconds in length, and the modulation function $\psi(t)$ was the same for all seismic events (as defined in Section 7.2.4). Thus, the DBE and MCE events were 30 seconds in length; and the DBE-MCE, MCE-DBE, and MCE-MCE sequences were composed of two 30 second length events, for a total time of 60 seconds. A sample base acceleration time history is shown for the DBE-MCE sequence in Figure 11.3.

All output variables are presented for Analysis 1, but only the primary output variable β_{50} is shown for the remainder of the analyses. Moreover, the primary output variable β_{50} is shown for all values of R for Analysis 1, but for other analyses, it is shown for only $R = 8$ (which is a typical value of R). Results are presented in Figure 11.4 through Figure 11.35.

11.3.4 Results and Discussion

Figure 11.11 shows the comparison of target versus calculated spectral acceleration values for Analysis 1. Notice that the actual and target values match well. This indicates that the input modules were calibrated correctly.

The effects of BRB, BRB, and seismic loading properties on the system reliability can be classified by the behavior of the reliability index with respect to:

Core Area A_c and Length L_c of BRB: In general, the system reliability varies with both A_c and L_c. As A_c and L_c become smaller, the system reliability goes down; this is logical, as, for a given demand (characterized by the value of R), BRBs with smaller core regions (smaller A_c and L_c) have less volume of material with which to absorb energy through yielding. For RC 1 (see Figure 11.8 and Figure 11.20 through Figure 11.25), changes in L_c tend to have a larger effect on system reliability than changes in A_c, whereas for RC 2 (see Figure 11.26 and Figure 11.29 through Figure 11.34), both parameters appear to have similar level of effects. This difference is attributed to the value of the model parameter associated with A_c. For RC 1, $TC \propto \left(\frac{A_c}{(A_c)_{\max}} \right)^{0.2019}$, whereas for RC 2, $TC \propto \left(\frac{A_c}{(A_c)_{\max}} \right)^{0.425}$. Therefore, the variation of TC hence RC with A_c should be stronger for RC 2 than RC 1.

Response Modification Coefficient R: As the value of R increases, the relative value of the seismic demands on the system increase. As a result, UC increases, and system reliability become smaller, as reflected in Figure 11.4 through Figure 11.10.

Core Yield Strength, F_y: According to the results from model RC 2 (results from RC 1 support this conclusion also), the yield stress has a significant effect on system reliability, as observed by comparing the values of β_{50} for Analysis 8 and Analysis 9. The values from Analysis 8 (Grade 36 steel, Figure 11.26) are higher than values from Analysis 9 (Grade 50 steel, Figure 11.29). This is logical, considering the effect of the yield stress on the predicted TC, where, for RC 2, $TC \propto \varepsilon_{yc}^{-3.45} \left(\frac{F_u}{F_y} \right)^{-1.46} = \left(\frac{F_y}{E} \right)^{-3.45} \left(\frac{F_u}{F_y} \right)^{-1.46} = \frac{F_y^{-1.99} F_u^{-1.46}}{E^{-3.45}}$. Thus, RC 2 predicts that as the core yield strength increases, the predicted TC decreases. This is reflective in the test results reported in the BRB test database – those BRBs with higher yield stress tended to have lower CPD capacity. In addition, this is a logical result, as higher yield stress steel typically has lower ductility than low yield stress steel.

Predicted RC: For RC 1, the TC, UC, and RC distributions are presented in Figure 11.17, Figure 11.18, and Figure 11.19, respectively. As expected, the TC distribution is primarily a function of A_c because of the relative values of the model parameters associated with A_c and L_c. On the other hand, the UC distribution is a function of the ductility parameters μ_c, $\mu_{\max}$, and $\mu_{\max loc}$ (the distribution shown in Figure 11.18 is calculated based on mean values of these parameters), and the distribution of these parameters is shown in Figure 11.14, Figure 11.15, and Figure 11.16. Note that the distribution of μ_c and $\mu_{\max}$ is entirely a function of L_c. This occurs because of the use of R as an independent variable in the reliability analyses. For given values of R and A_c, the values of m are determined per equation 11.1. When A_c is then varied, a new value of m is calculated to ensure R remains the same. In this way, the use of R

removes the variation of system reliability with A_c. While μ_c and $\mu_{\max}$ vary with respect to L_c, $\mu_{\max loc}$ does not; this is logical, as $\mu_{\max loc}$ is a function of seismic loading duration and stationarity, which do not change between runs. The resulting distribution of RC is of course both a function of TC and UC, as $RC = TC - UC$. Finally, the mean system reliability β_{50} is highly correlated to the mean RC. Values of $RC = 0$ relate closely to $\beta_{50} = 0$, and this is logical, as this indicates that there is a 50% chance of failure when the mean RC is zero. RC and β_{50} do not directly correlate because of the shape of the distribution of the random variables μ_c, $\mu_{\max}$, $\mu_{\max loc}$.

It should be noted that the inclusion of $\mu_{\max loc}$ makes the RC 1 model behave incorrectly. From the equation for RC 1, $TC \propto \mu_{\max loc}^{-0.9883}$. Thus loading sequences where the location of the maximum demand is early, e.g. the MCE-DBE sequence, may have higher predicted values of TC than sequences where the maximum demand occurs later, e.g. the DBE-MCE sequence. This is reflected in the results discussed below. It is not, however, logical, as it has been observed (as discussed in Section 0) that BRBs subjected to high early demand tend to have less ductility capacity than those subject to late high demands. The model parameter associated with $\mu_{\max loc}$ was calibrated based on test data, and does match the results from the tests. However, the behavior implied by the tests does not match that which has been observed; this occurs because, for most BRBs in the test database, the imposed deformation histories were cyclic, not simulated seismic loadings, and the effects of the cyclic loadings may not correlate to the effects caused by true seismic loadings. Overall, the effect caused by the $\mu_{\max loc}$ term was judged to not truly represent BRB behavior. For this reason, the RC 2 model was developed without use of the $\mu_{\max loc}$ term.

RC Model Error, σ: The variation between β_{50}, β_{10}, and β_5 is proportional to the value of σ. As the value of σ for RC 1 is much smaller than for RC 2, the variation in the reliability indices is much smaller for RC 1 than for RC 2. The variation between β_{50}, β_{10}, and β_5 for RC 1 may be observed in Figure 11.8, Figure 11.12, and Figure 11.13, while for RC 2 it may be observed in Figure 11.26, Figure 11.27, and Figure 11.28. For RC 1, an average difference between β_{50} and β_{10} is approximately 2 to 3, whereas for RC 2 the average difference is approximately 5 to 6 – quite a disparity.

Seismic Loading Sequence: Obviously, the seismic loading applied to the BRB has a significant effect on the BRB system reliability. In the case of RC 1, the seismic loading sequence affects both BRB TC and UC because of the inclusion of the $\mu_{\max loc}$ term in the TC component. In the case of RC 2, the seismic loading sequence only affects the UC component of BRB RC.

The effect of seismic loading for model RC 1 can be observed by comparing the β_{50} values for the following results:

- Analysis 1, DBE, Figure 11.8
- Analysis 3, MCE, Figure 11.21
- Analysis 4, DBE-DBE, Figure 11.22
- Analysis 5, DBE-MCE, Figure 11.2

- Analysis 6, MCE-DBE, Figure 11.24
- Analysis 7, MCE-MCE, Figure 11.25

In general, the system reliability decreases with the imposed seismic demand. The system reliability for RC 1, ordered from highest to lowest is:

DBE > MCE > DBE-DBE > MCE-DBE > DBE-MCE > MCE-MCE

Interestingly, the reliability for the DBE-DBE loading is approximately the same as that of the MCE-DBE loading; in addition, the reliability for the MCE-DBE loading is significantly higher than for the DBE-MCE loading, even though the UC for each should be approximately the same. This phenomenon occurs because of the inclusion of the $\mu_{\max loc}$ in the TC component, as discussed previously.

The effect of seismic loading for model RC 2 can be observed by comparing the β_{50} values for the following results:

- Analysis 8, DBE, Figure 11.26
- Analysis 10, MCE, Figure 11.30
- Analysis 11, DBE-DBE, Figure 11.31
- Analysis 12, DBE-MCE, Figure 11.32
- Analysis 13, MCE-DBE, Figure 11.33
- Analysis 14, MCE-MCE, Figure 11.34

In general, again, the system reliability decreases as the seismic loading severity increases. The system reliability for RC 2, ordered from highest to lowest is:

DBE > MCE > DBE-DBE > DBE-MCE > MCE-DBE > MCE-MCE

Unlike the results from the RC 1 model, the system reliability for the DBE-DBE loading is higher than that for the DBE-MCE and MCE-DBE models; also, the system reliability for these two loading sequences is fairly similar. This is expected because the RC 2 model does not include the $\mu_{\max loc}$ term, and the TC does not depend on the loading history.

While in general, for both RC 1 and RC 2 results, system reliability decreases as the seismic loading severity increases, the relative change between the reliability for one loading and another is not uniform across the spectrum of BRB properties – i.e. it varies with A_c and L_c. For example, consider the comparison between the results for Analysis 10 (RC 2, MCE) and the results for Analysis 11 (RC2, DBE-DBE). Figure 11.35 shows the difference between the β_{50} values for the two analyses. At small values of A_c and L_c, the MCE loading results in higher system reliability, whereas for larger values of A_c and L_c, the DBE-DBE loading results in higher system reliability.

11.4 Fragility Analysis

Fragility analyses may be conducted easily using the PBEF created in this research effort. The results of these analyses are fragility curves, which give conditional probability of BRB fatigue fracture given ground shaking intensity. The curve can be created for any assumed structure and BRB.

In this research effort, fragility analyses were performed for two example structures. BRB, BRBF, and seismic loading properties of the fragility analyses are summarized in Table 11.7 and Table 11.8. Structure properties in each analysis were

based on average values from the BRB test database and are the same for each analysis, except that the core length of the analysis Fragility 2 was half that of Fragility 1. Input module 1 was used to perform the fragility analyses, and the only variable varied in each analysis was the input PSD intensity Φ_0.

Figure 11.36 shows the relationship between the probability of brace failure (fatigue fracture) and the peak ground acceleration for each fragility analysis. (While the analyses produce a series of points, log-normal CDFs can easily be fitted to the data (see [44] for the approach)).Obviously, the system of analysis Fragility 2 (with $L_c = 48$ in) is a more vulnerable system than that of Fragility 1 (with $L_c = 97$ in). This is logical since the BRB with the shorter yielding region develops larger inelastic deformations for the same overall brace deformation when compared to the BRB with longer yielding region. It should be noted that this represents the probability of brace failure for a seismic loading duration of 30 seconds. Certainly, longer duration loadings would require lower values of PGA to cause failure. This is only one example of the myriad of fragility analyses that could be performed using this method. For example, different analyses could be conducted to investigate the effects of BRB core area, seismic loading duration, stationarity, etc.

11.5 Conclusions and Applications

Parametric studies were conducted, using both RC 1 and RC 2 models, to investigate the influence of BRB, BRBF, and seismic loading properties on the system reliability. The variation of *TC*, *UC*, and *RC* with BRB and BRBF properties was shown, and it was demonstrated that the mean system reliability is highly correlated with the mean predicted *RC*. The various effects of BRB and BRBF properties along with the imposed seismic loadings were discussed. Specifically, the RC 1 model was found to behave incorrectly due to the inclusion of the $\mu_{\max loc}$ term. While RC 2 did behave correctly, because the RC 2 model was both less precise and accurate than the RC 1 model, the bounds on system reliability (i.e. β_{10}, β_5, etc.) were much wider for RC 2 than RC 1.

This PBEF and the results from the parametric study can be directly applied to evaluate the performance of BRBs and BRBF in relation to fatigue fracture of the BRB core, without the need to perform nonlinear dynamic or reliability analyses. A basic design case exists where one might proceed as follows:

1) Proportion a BRBF using a code-based equivalent lateral force seismic design procedure. This procedure uses a response modification coefficient of typically 7 or 8 [32] and leads to selection of BRB properties (A_c, L_c, F_y, etc.).

2) Determine the confidence level required; i.e. determine the desired value of the reliability index and if this is based on β_{50}, β_{10}, or β_5 (as discussed in Section 10.5).

3) Evaluate the predicted value of reliability based on the figures presented in this chapter. Or, if the BRB and BRBF properties do not match those on which the

results presented in the figures are based, perform a single reliability analysis using the PBEF for the specific BRB, BRBF, and seismic loading properties to determine the reliability index. Or, at the user's risk, reliability indices can be interpolated form the presented figures.

4) If the reliability index is greater than that desired, BRB design is finished. If it is lower, BRB properties may need to be changed based on the behavior presented in the figures such that the reliability index is greater than or equal to that desired.

5) Reiterate strength design of the BRB and BRBF based on the new BRB properties.

6) Repeat these steps until BRB and BRBF properties satisfy both strength design requirements and design for fatigue fracture requirements.

In the case when the specific tools and models presented in this research do not satisfy a given BRB and BRBF design application, the PBEF can be easily altered to accommodate different:

- **Seismic loadings**: This can be accomplished through altering the input modules described in Chapter 7 or by creating new input modules. To be functional, the input module simply has to produce a base-acceleration time history for input into the BRBF system model. For example, instead of using randomly generated loadings, a specific earthquake record or suite of records could be used.

- **BRB and BRBF models**: By altering the system models described in Chapter 8, users of the PBEF can customize the analyses based on desired structural and BRB models. For example, multiple degree-of-freedom models could be used, or a different hysteric model for the BRB could be implemented.

- **Ductility capacity models**: If more accurate and precise models ductility capacity models are developed, they can easily be implemented in the PBEF; to implement models, users must simply define a limit state function $g(\mathbf{x})$ such that $g(\mathbf{x}) \leq 0$ defines failure. Also, multiple limit state functions could be used (for example, for a multiple BRB structure).

- **Analyses:** A wide variety of analyses can be performed with the PBEF. For example, fragility analyses could be performed for a wide class of BRBs, BRBFs, and seismic loadings. In addition, parametric studies could be performed that vary different properties than those in this research.

11.6 Chapter 10 Figures

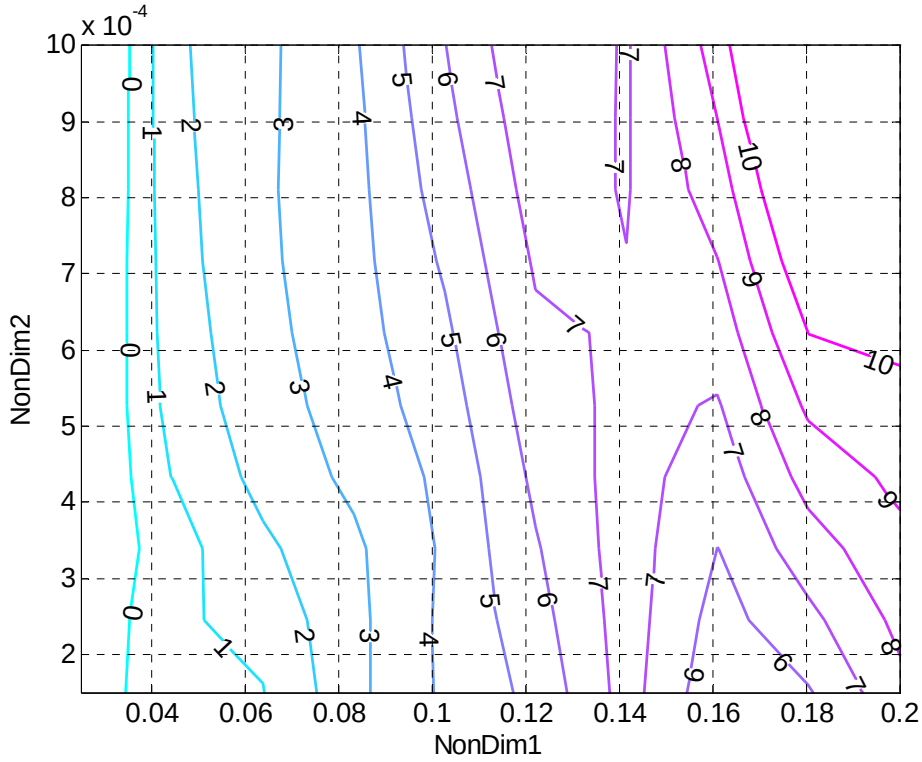

Figure 11.1: β_{50} , Analysis NON DIM A

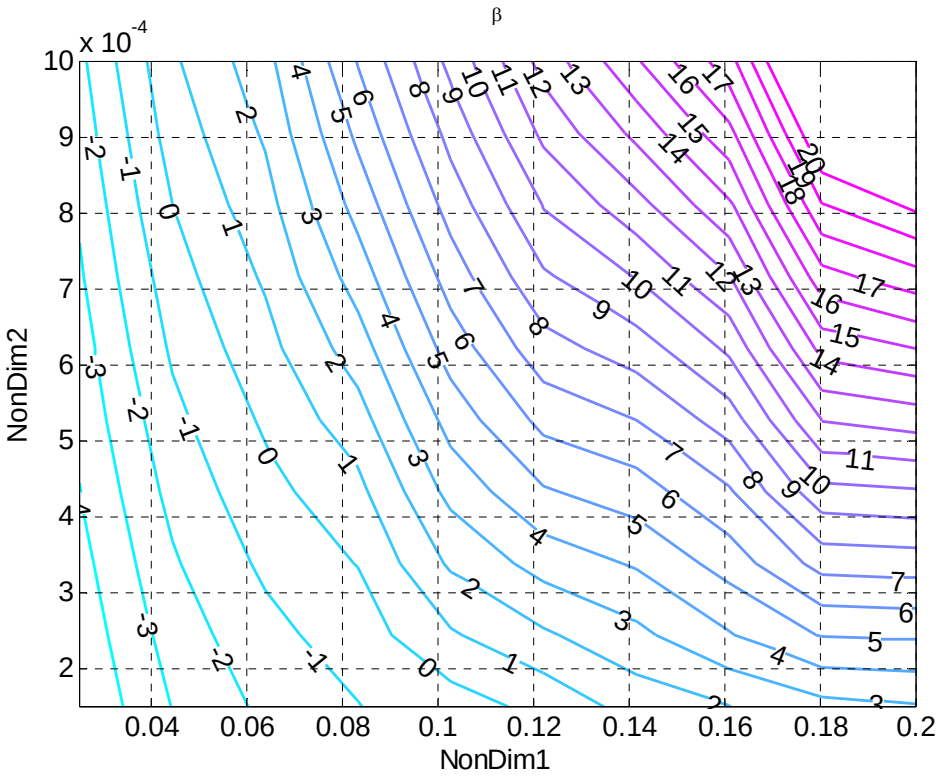

Figure 11.2: β_{50} , Analysis NON DIM B

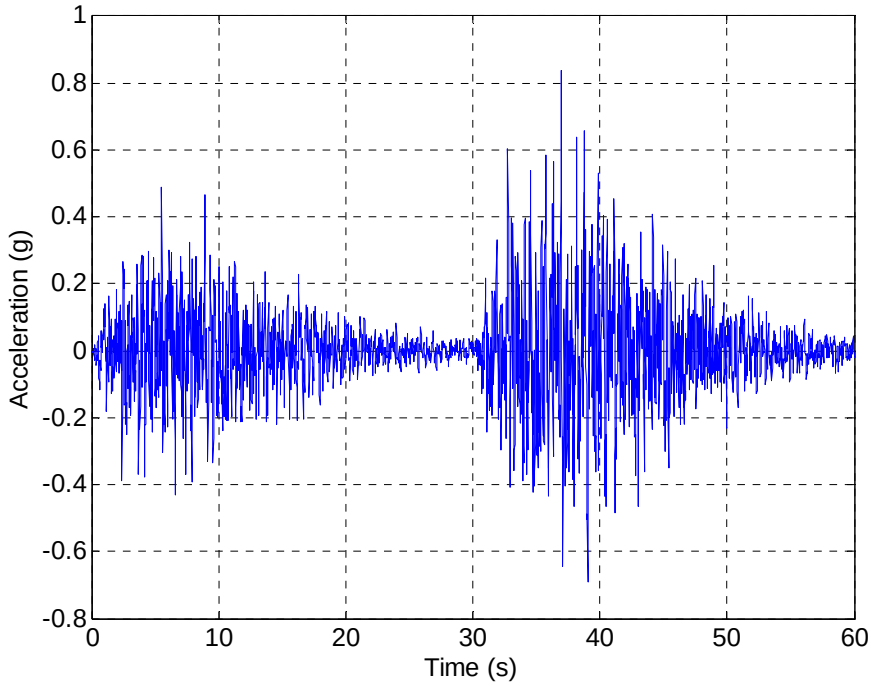

Figure 11.3: Sample Base Acceleration Time History for DBE-MCE Sequence

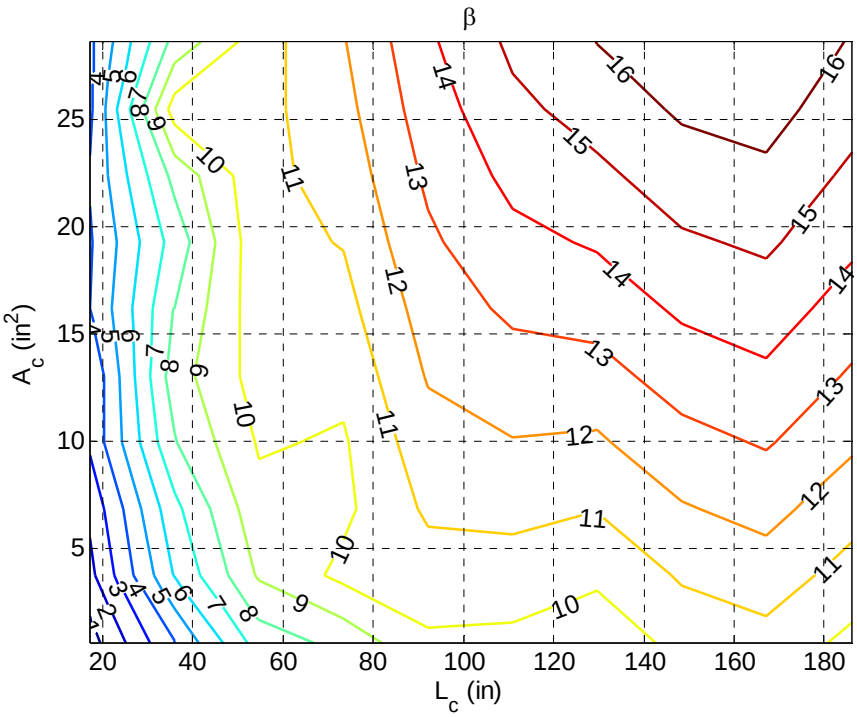

Figure 11.4: β_{50} **, Analysis 1 (RC 1, Grade 36, DBE),** $R = 4$

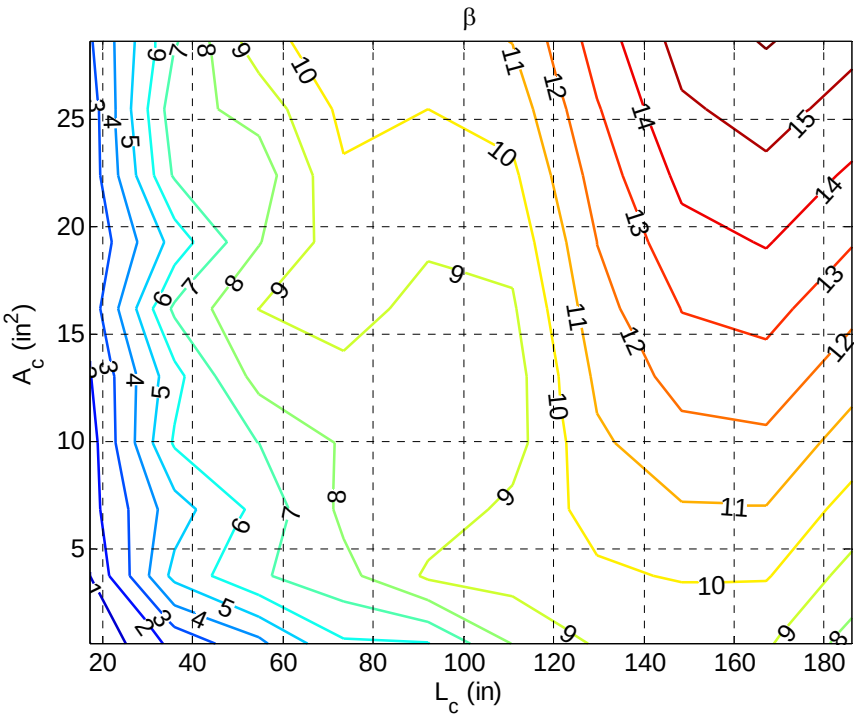

Figure 11.5: β_{50} **, Analysis 1 (RC 1, Grade 36, DBE),** $R = 5$

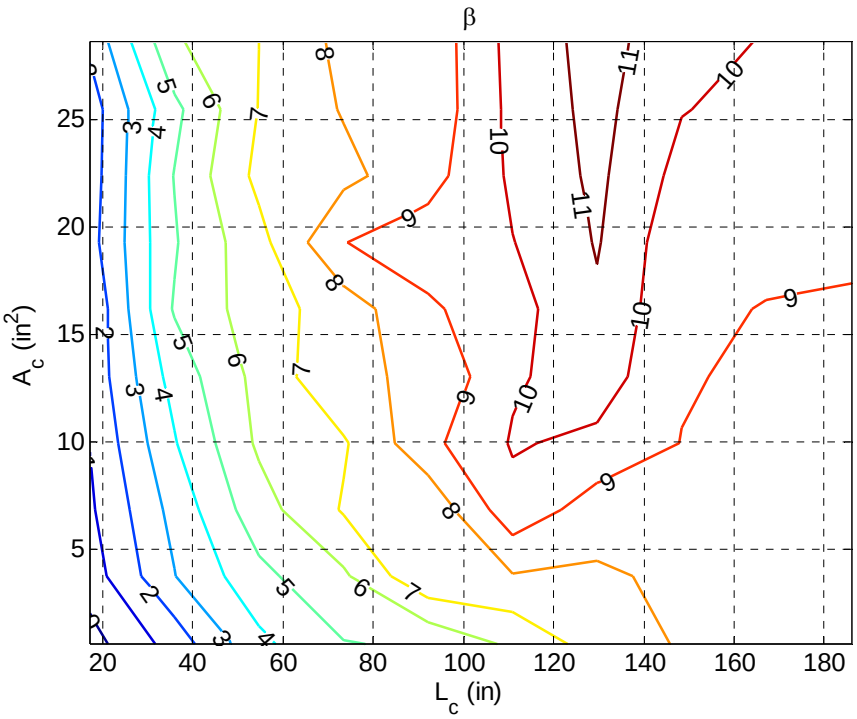

Figure 11.6: β_{50} **, Analysis 1 (RC 1, Grade 36, DBE),** $R = 6$

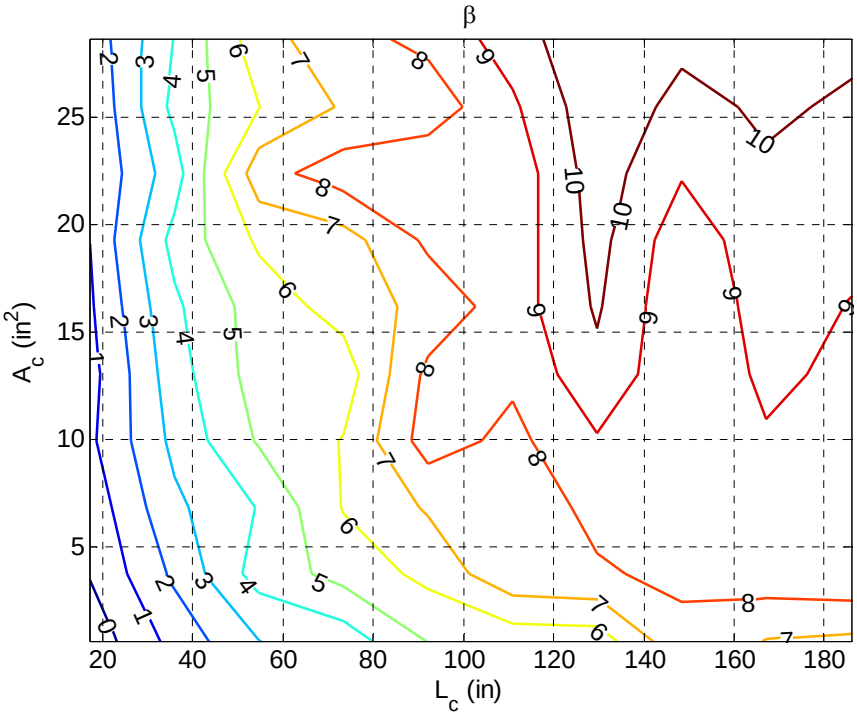

Figure 11.7: β_{50} **, Analysis 1 (RC 1, Grade 36, DBE),** $R = 7$

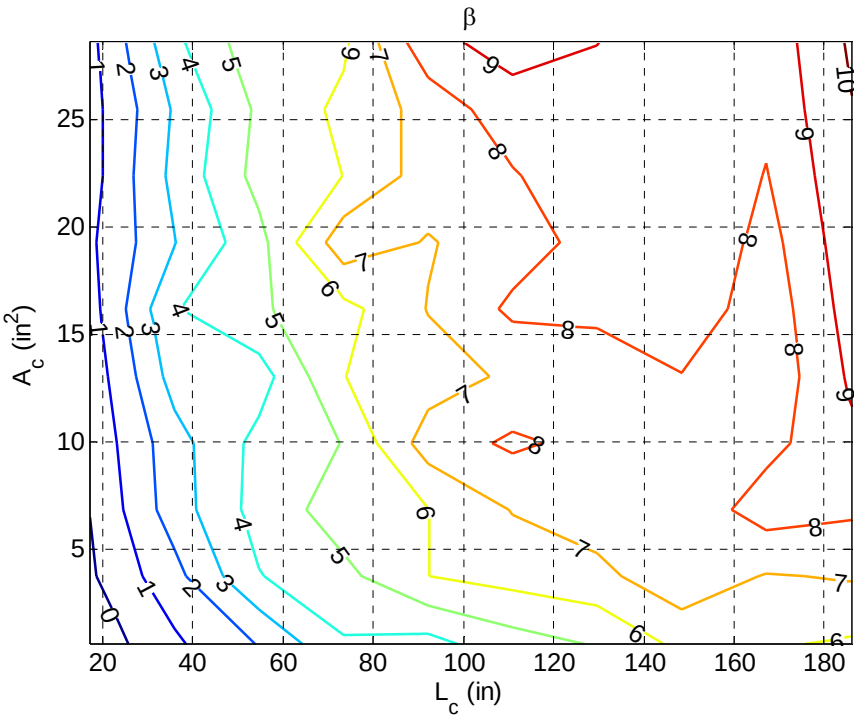

Figure 11.8: β_{50} **, Analysis 1 (RC 1, Grade 36, DBE),** $R = 8$

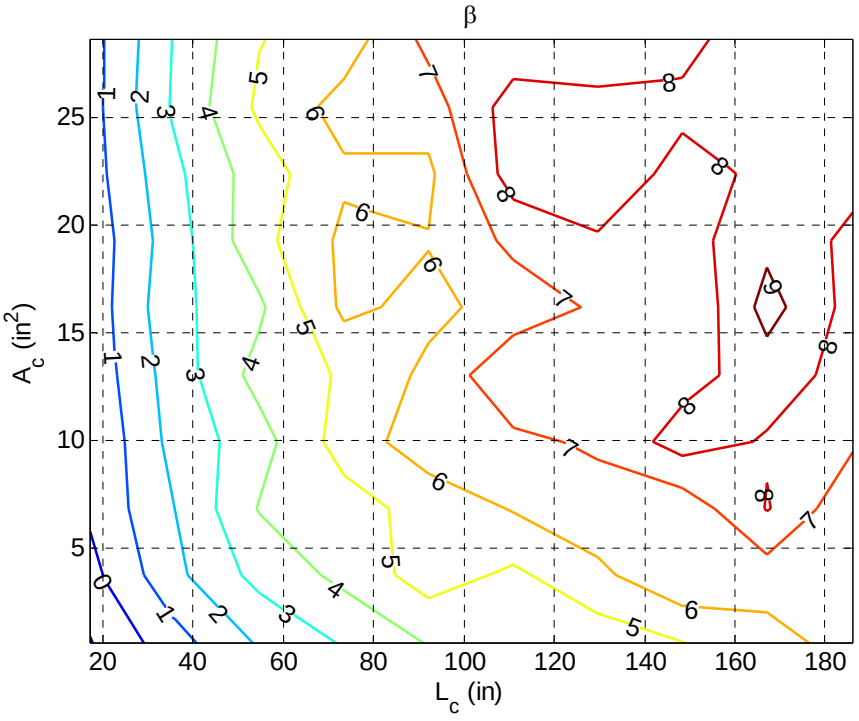

Figure 11.9: β_{50} **, Analysis 1 (RC 1, Grade 36, DBE),** $R = 9$

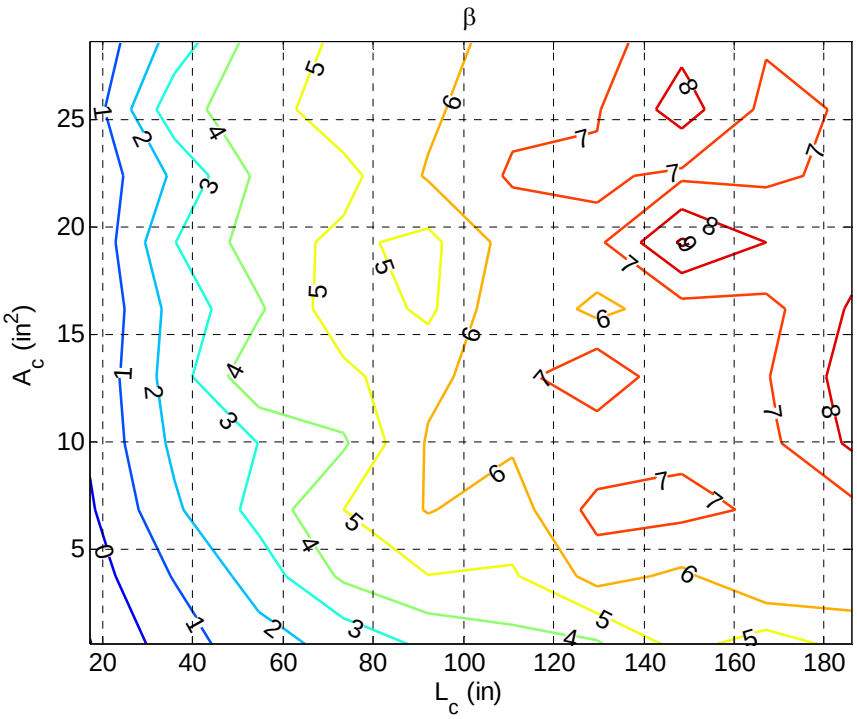

Figure 11.10: β_{50} **, Analysis 1 (RC 1, Grade 36, DBE),** $R = 10$

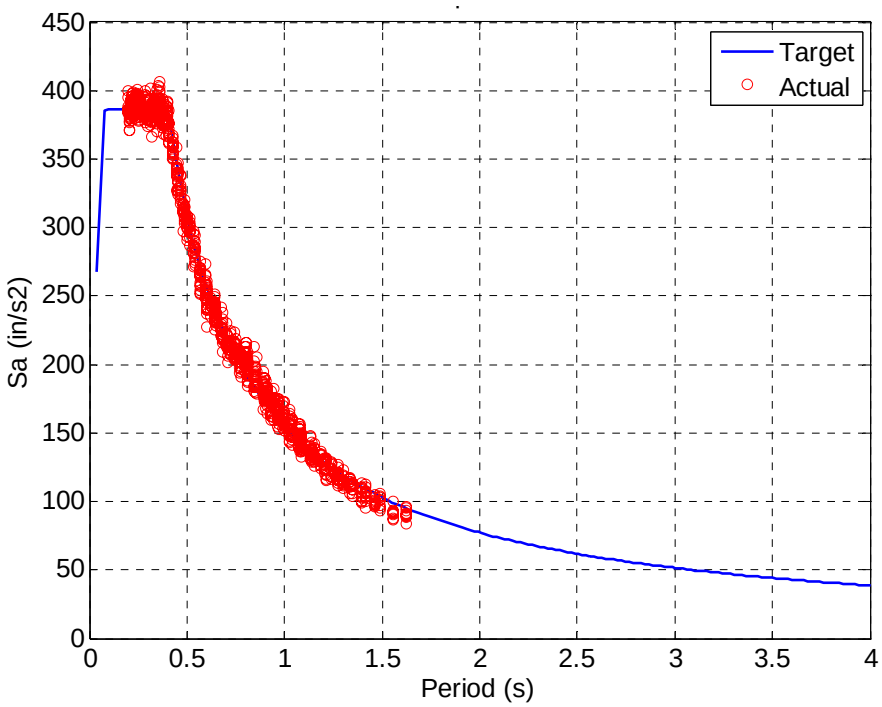

Figure 11.11: Analysis 1 Spectral Acceleration

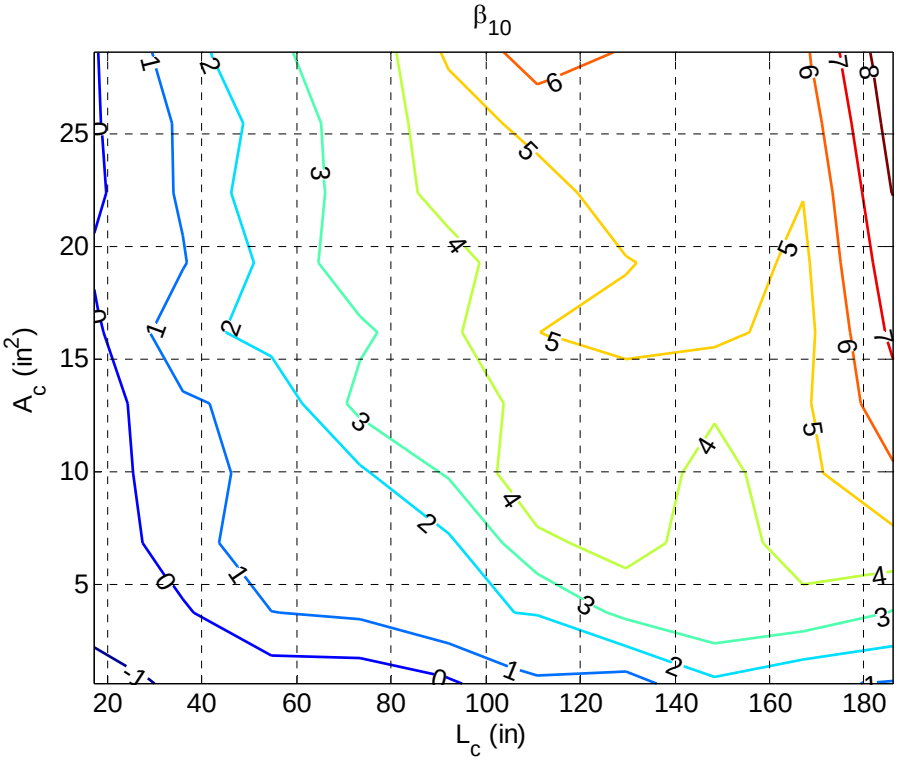

Figure 11.12: β_{10}**, Analysis 1 (RC 1, Grade 36, DBE),** $R = 8$

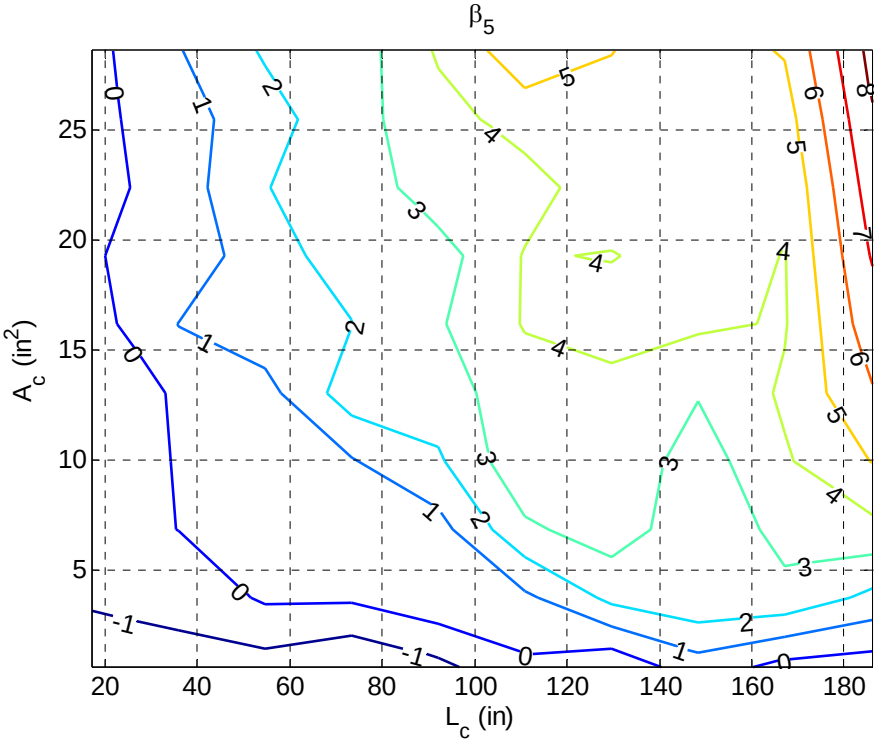

Figure 11.13: β_5**, Analysis 1 (RC 1, Grade 36, DBE),** $R = 8$

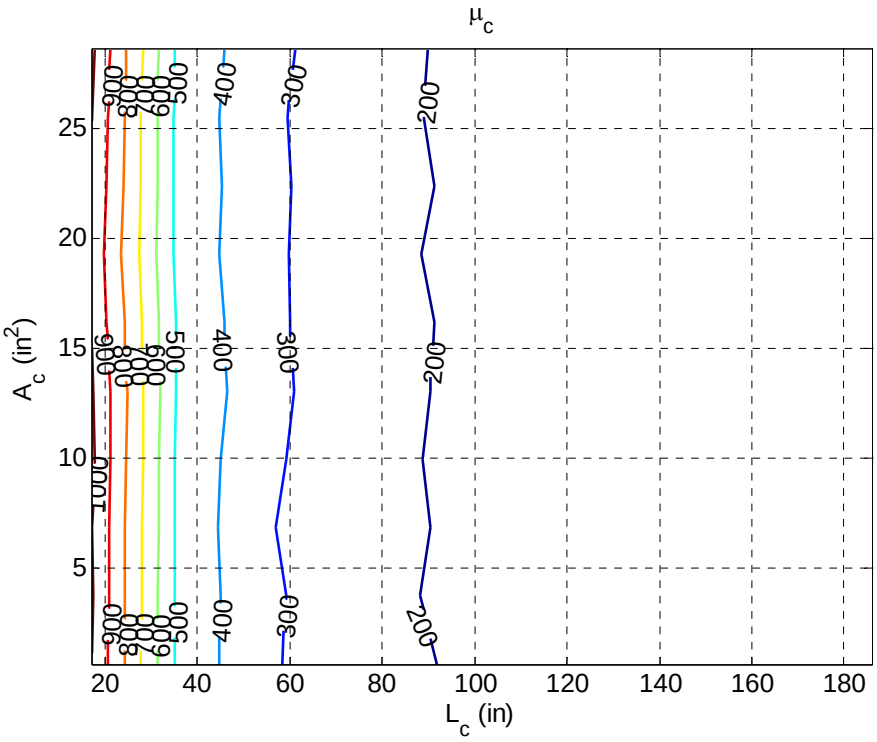

Figure 11.14: μ_c **, Analysis 1 (RC 1, Grade 36, DBE),** $R = 8$

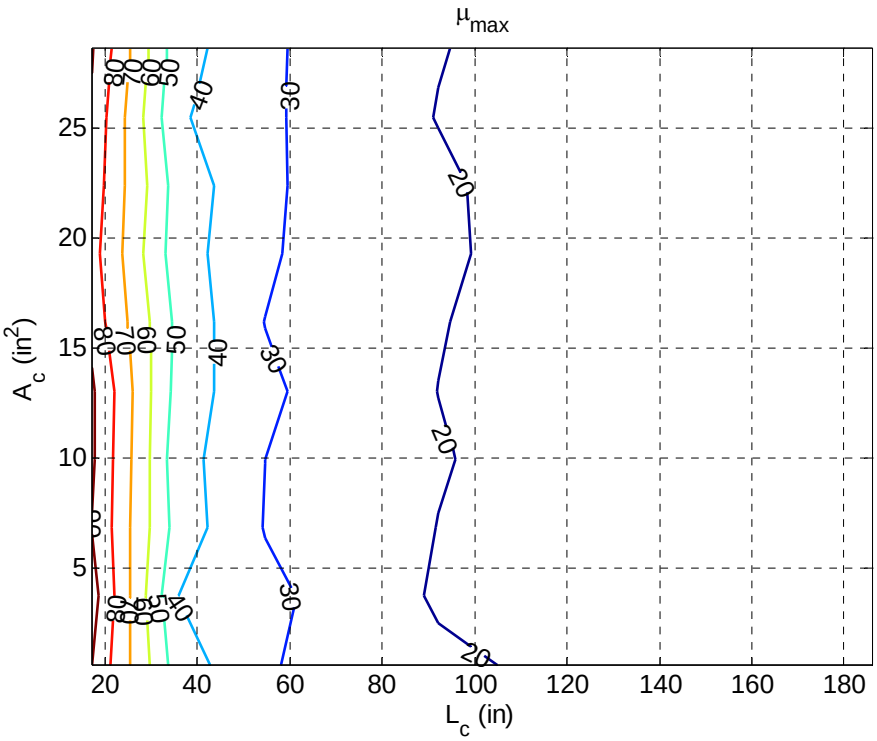

Figure 11.15: μ_{max} **, Analysis 1 (RC 1, Grade 36, DBE),** $R = 8$

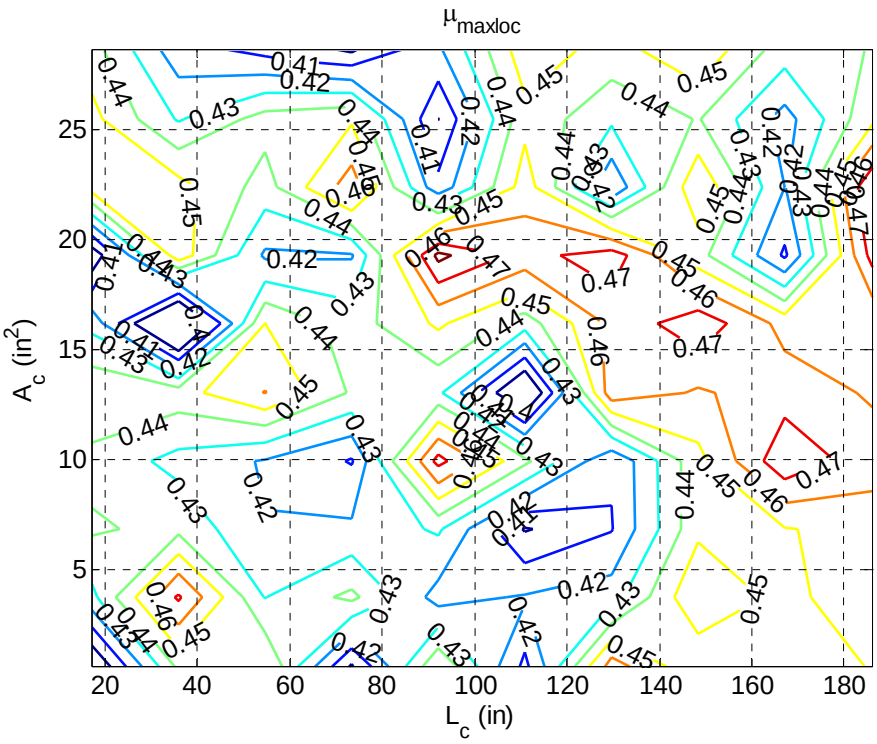

Figure 11.16: $\mu_{\max loc}$**, Analysis 1 (RC 1, Grade 36, DBE),** $R = 8$

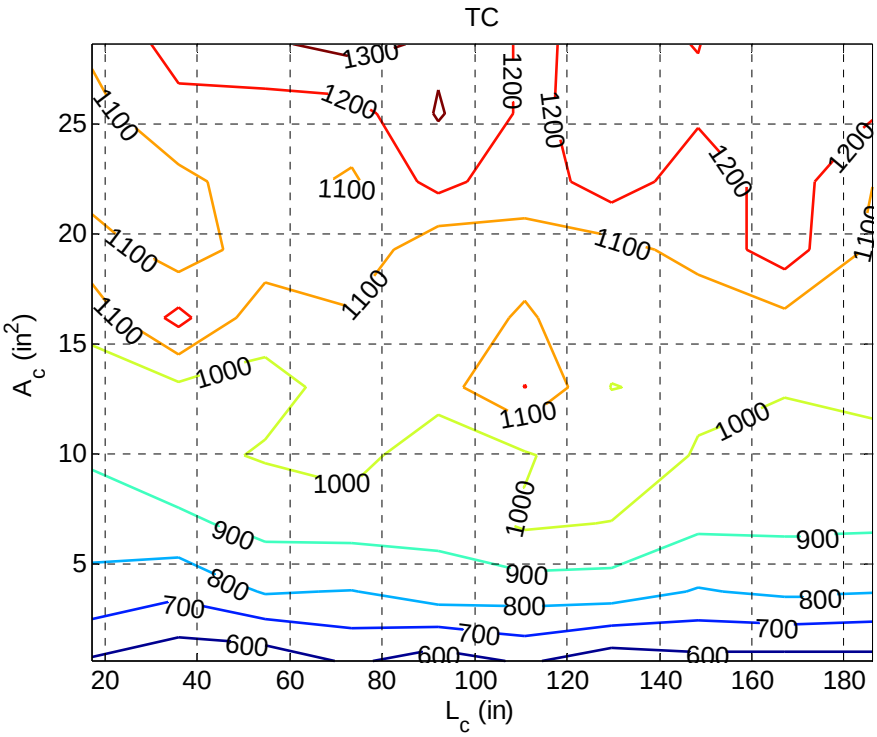

Figure 11.17: TC**, Analysis 1 (RC 1, Grade 36, DBE)**

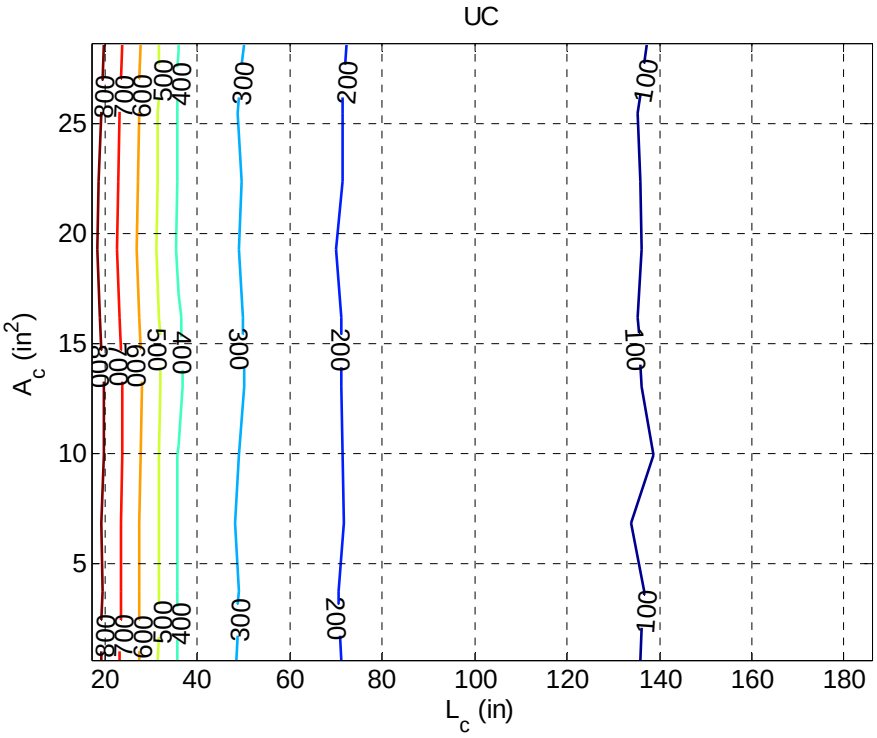

Figure 11.18: *UC* **, Analysis 1 (RC 1, Grade 36, DBE),** $R = 8$

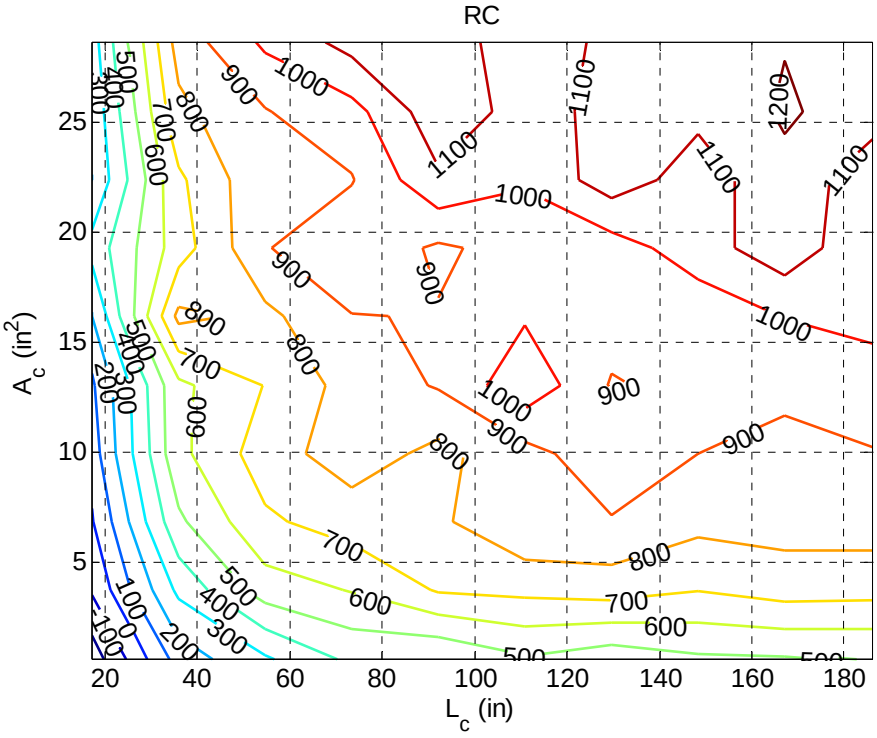

Figure 11.19: *RC* **, Analysis 1 (RC 1, Grade 36, DBE),** $R = 8$

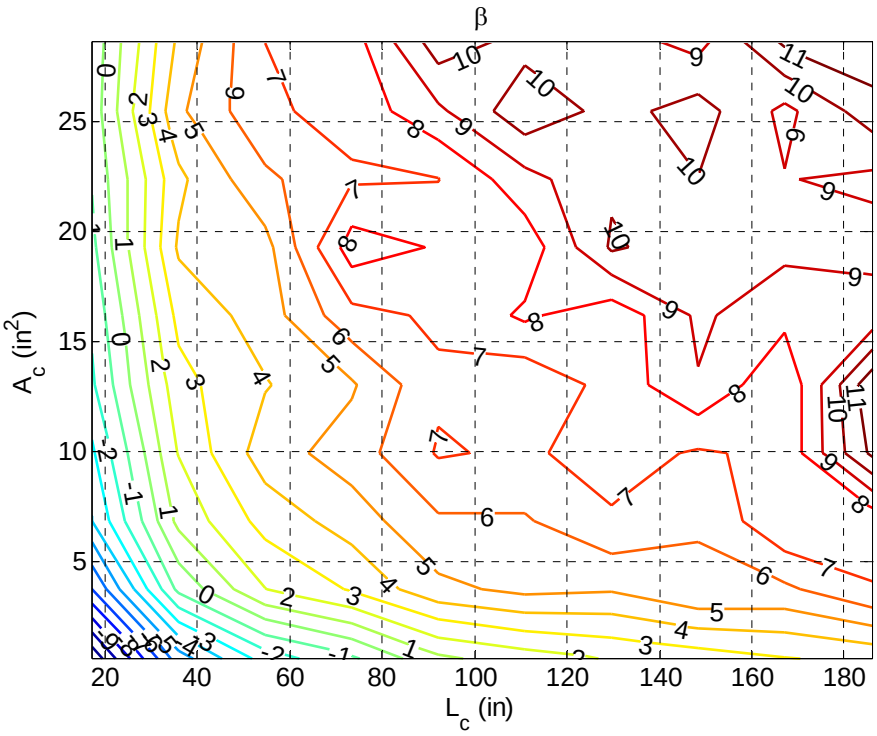

Figure 11.20: β_{50} **, Analysis 2 (RC 1, Grade 50, DBE),** $R = 8$

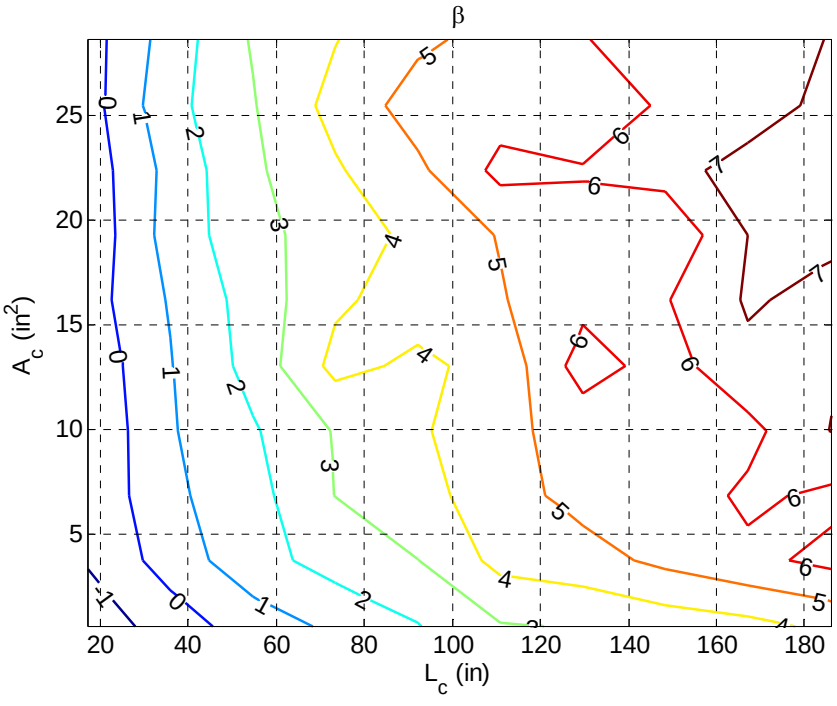

Figure 11.21: β_{50} **, Analysis 3 (RC 1, Grade 36, MCE),** $R = 8$ **(MCE)**

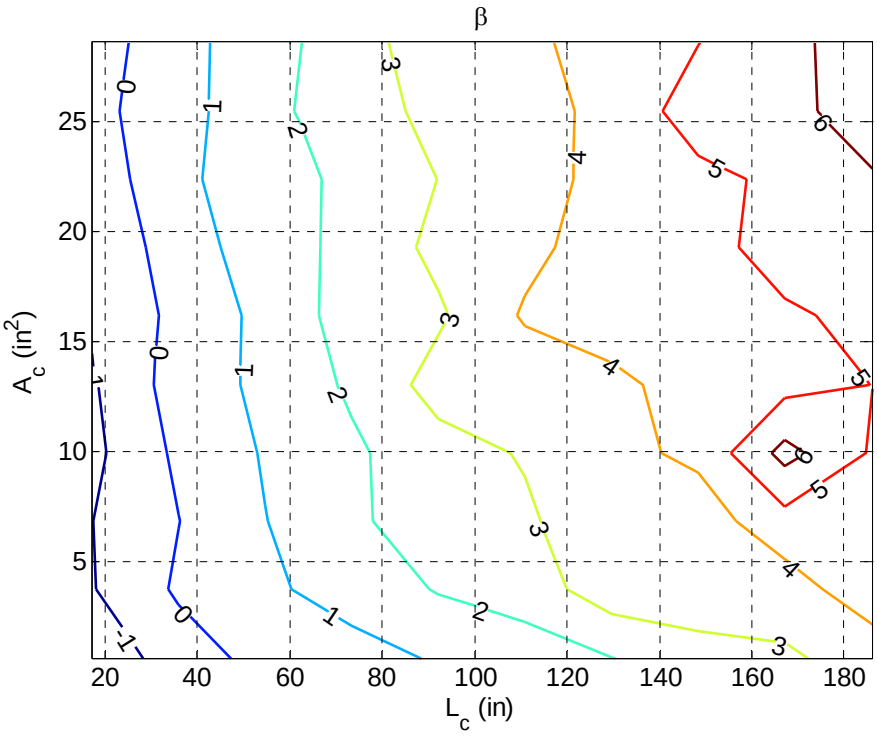

Figure 11.22: β_{50} **, Analysis 4 (RC 1, Grade 36, DBE-DBE),** $R = 8$

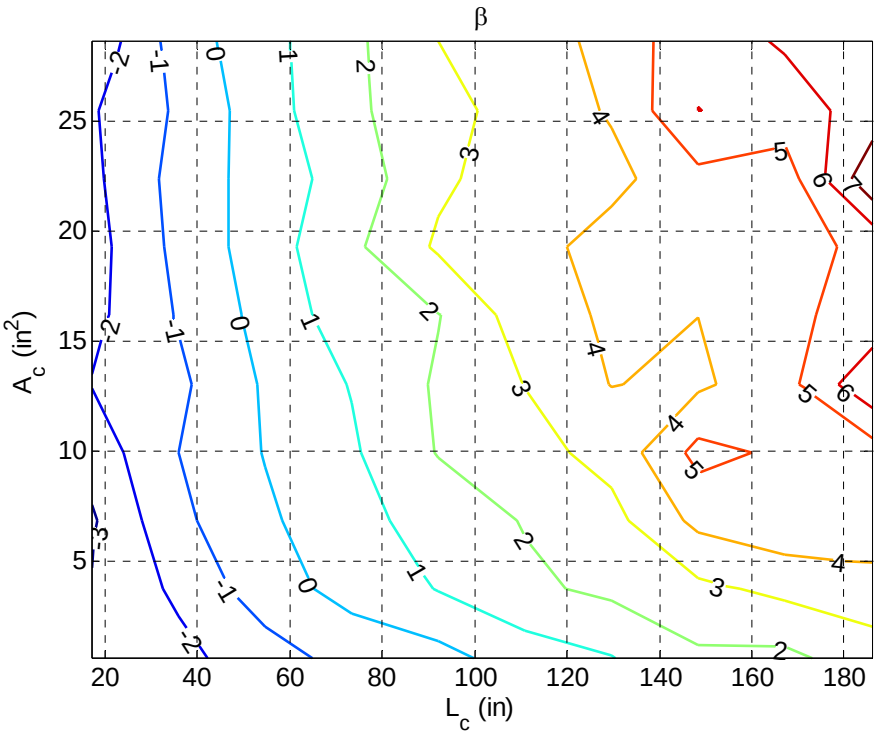

Figure 11.23: β_{50} **, Analysis 5 (RC 1, Grade 36, DBE-MCE),** $R = 8$

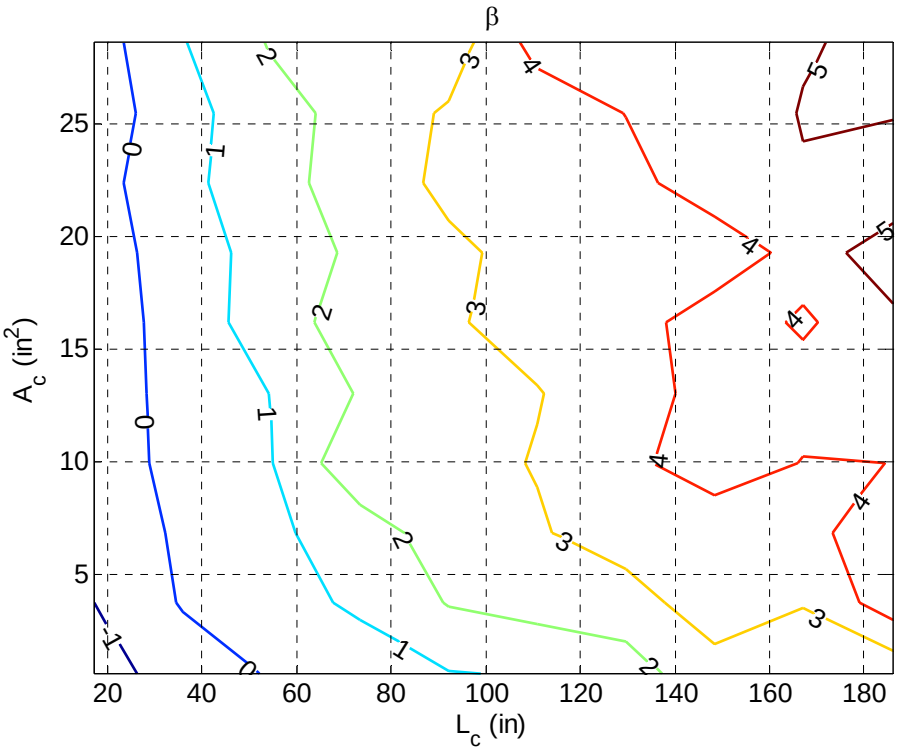

Figure 11.24: β_{50} **, Analysis 6 (RC 1, Grade 36, MCE-DBE),** $R = 8$

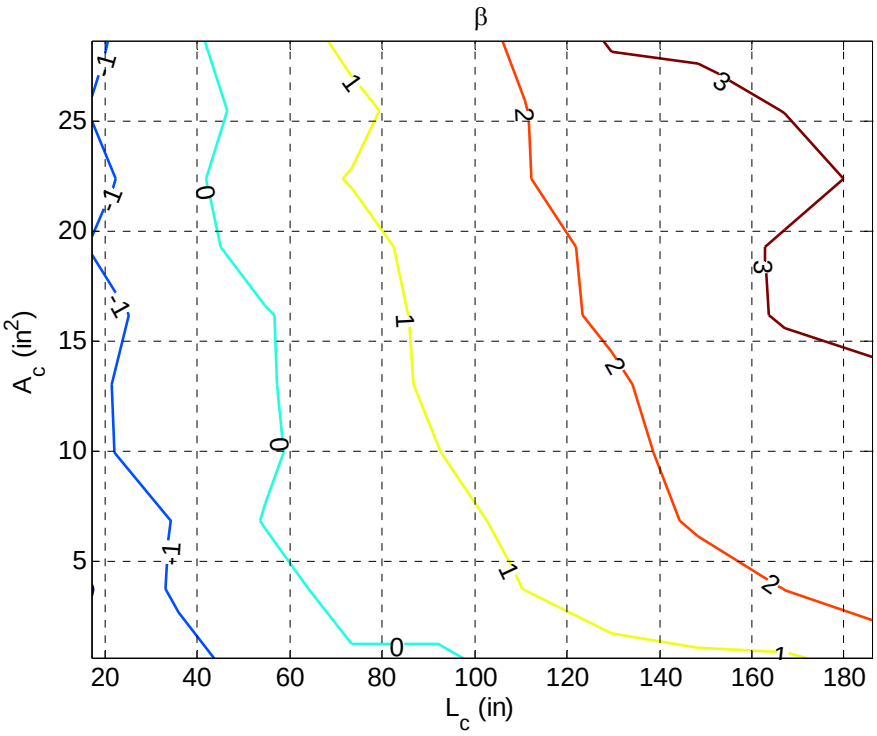

Figure 11.25: β_{50} **, Analysis 7 (RC 1, Grade 36, MCE-MCE),** $R = 8$

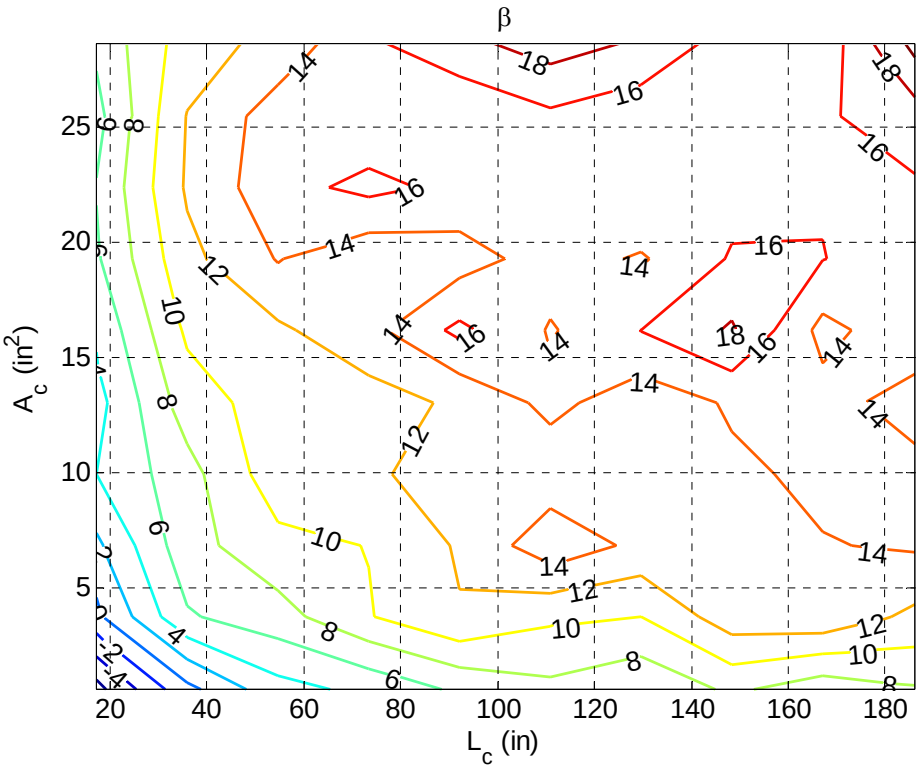

Figure 11.26: β_{50} **, Analysis 8 (RC 2, Grade 36, DBE),** $R = 8$

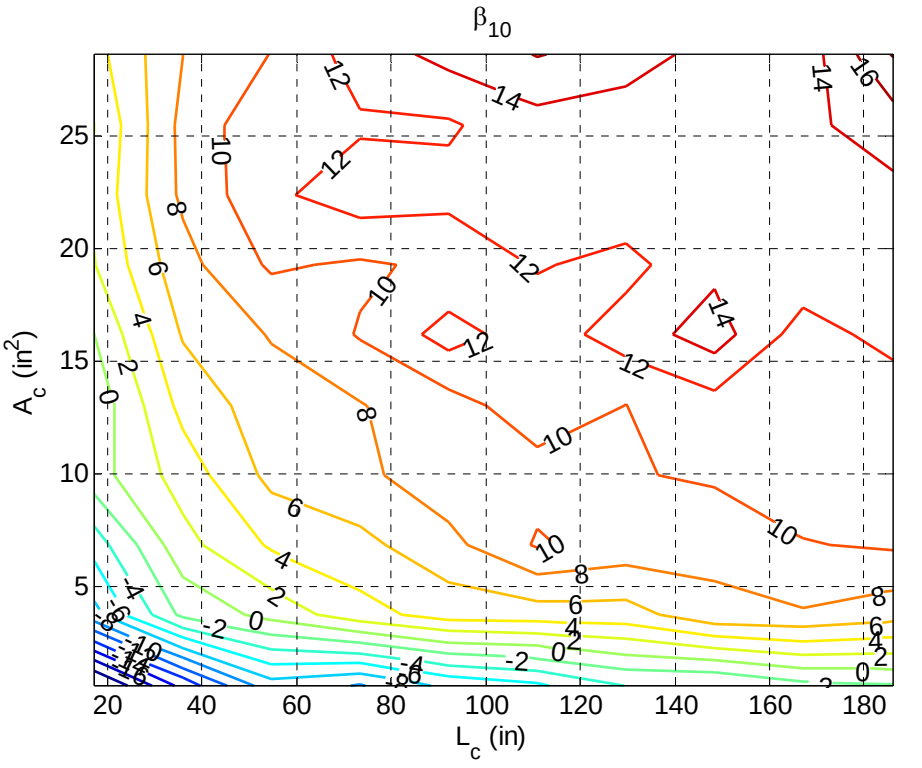

Figure 11.27: β_{10} **, Analysis 8 (RC 2, Grade 36, DBE),** $R = 8$

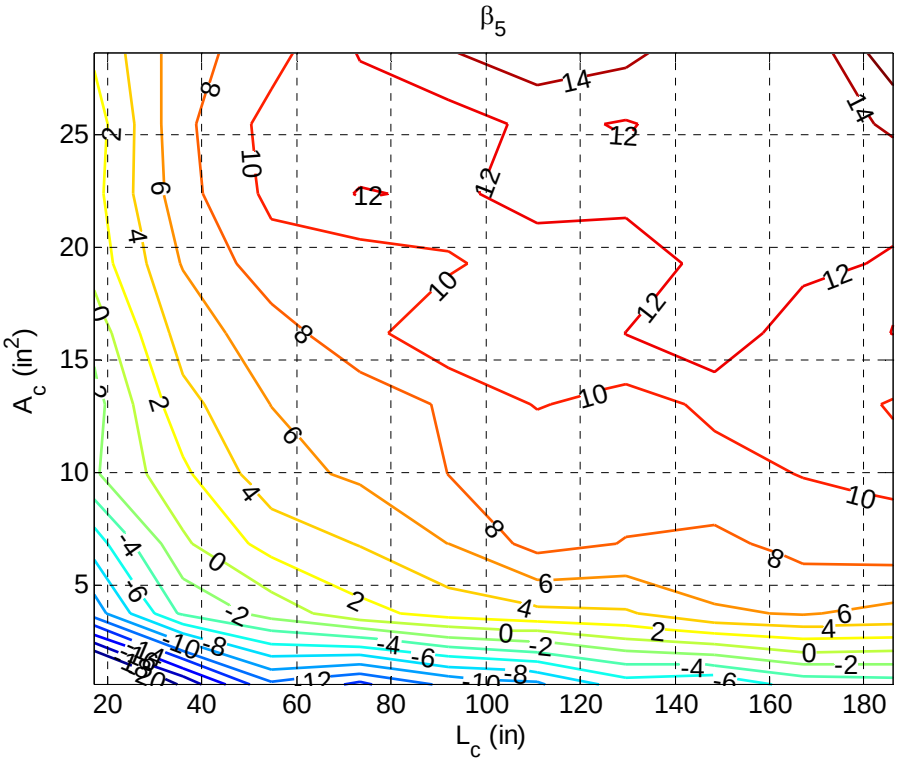

Figure 11.28: β_5 **, Analysis 8 (RC 2, Grade 36, DBE),** $R = 8$

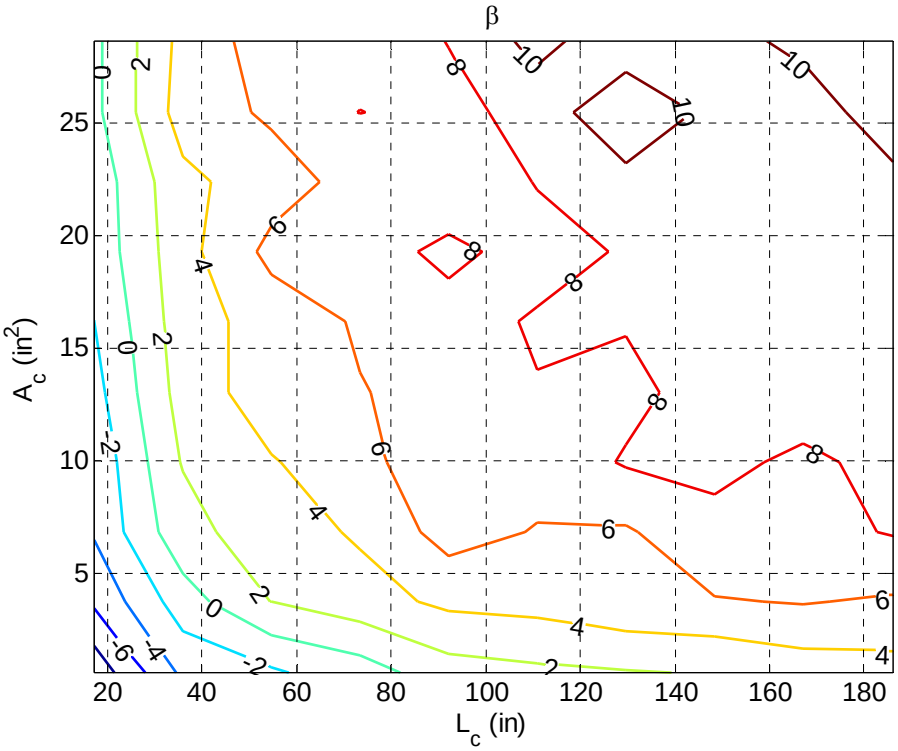

Figure 11.29: β_{50} **, Analysis 9 (RC 2, Grade 50, DBE),** $R = 8$

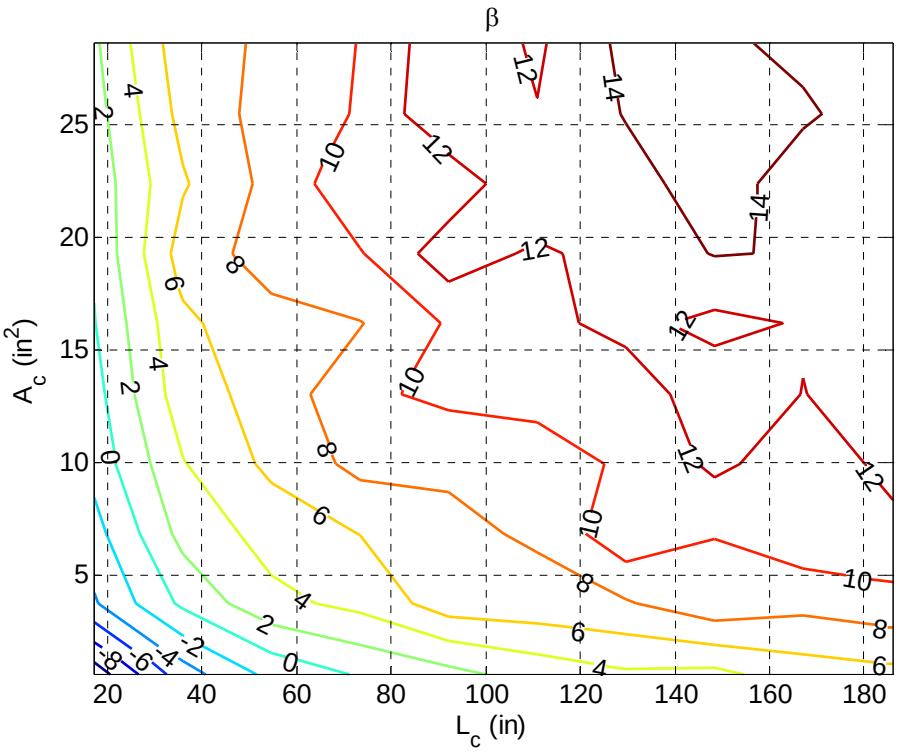

Figure 11.30: β_{50} **Analysis 10 (RC 2, Grade 36, MCE),** $R = 8$

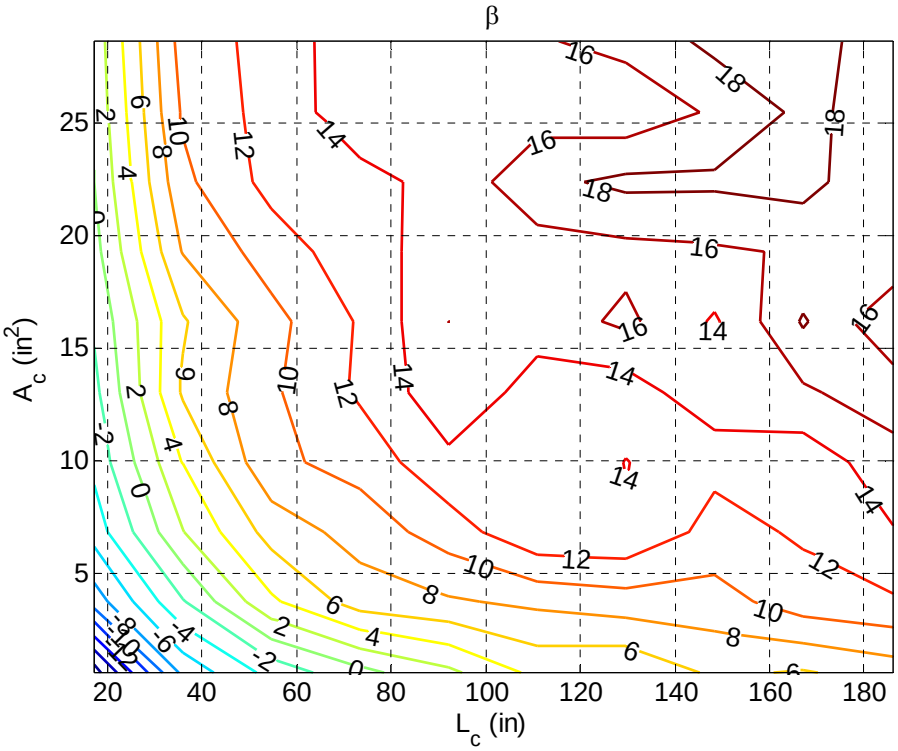

Figure 11.31: β_{50} **, Analysis 11 (RC 2, Grade 36, DBE-DBE),** $R = 8$

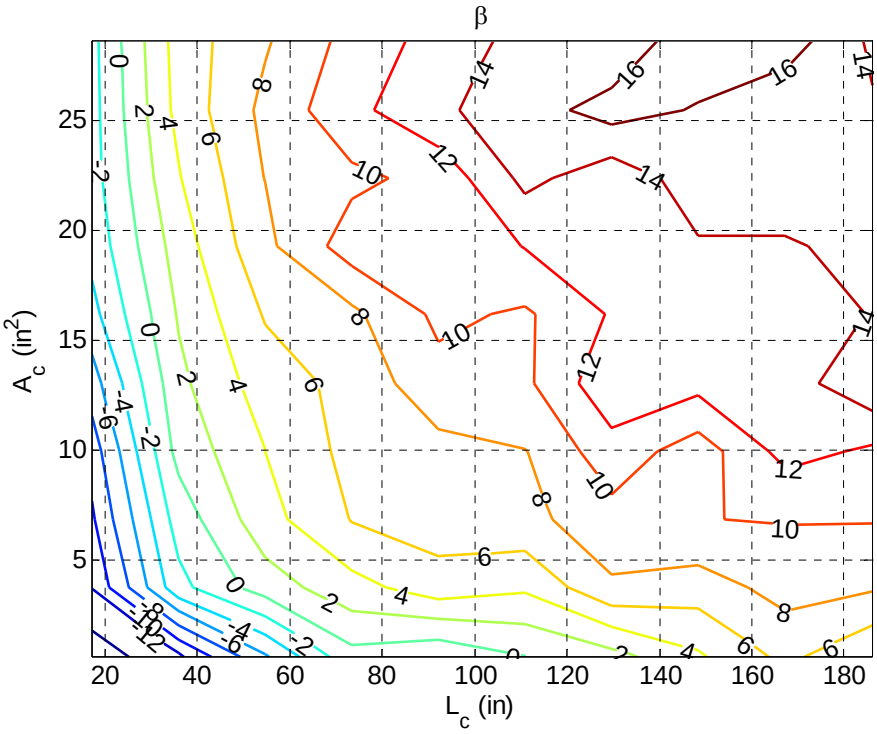

Figure 11.32: β_{50} **, Analysis 12 (RC 2, Grade 36, DBE-MCE),** $R = 8$

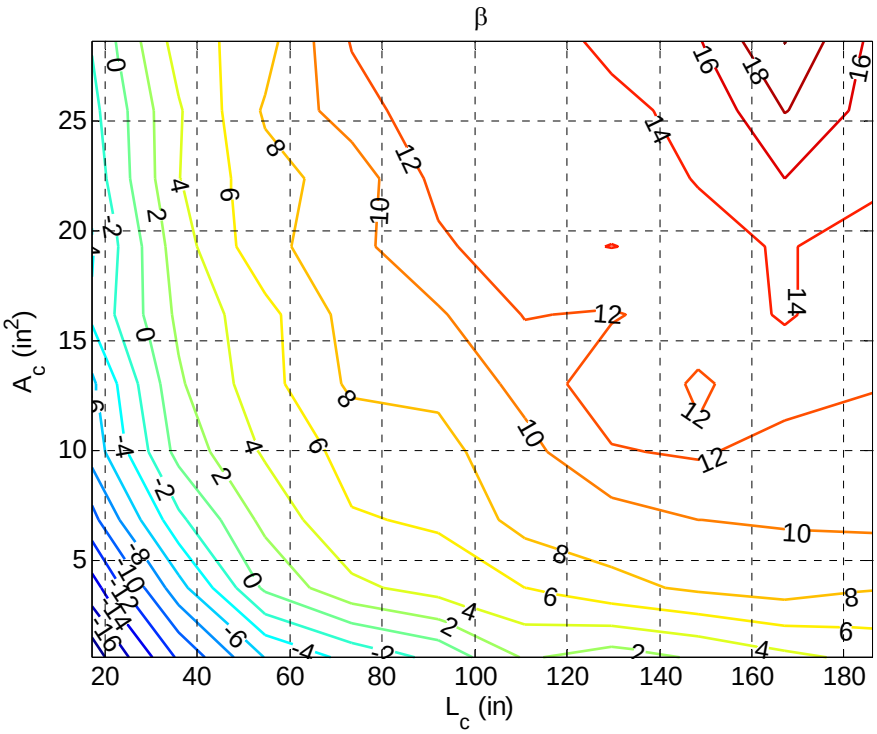

Figure 11.33: β_{50} **, Analysis 13 (RC 2, Grade 36, MCE-DBE),** $R = 8$

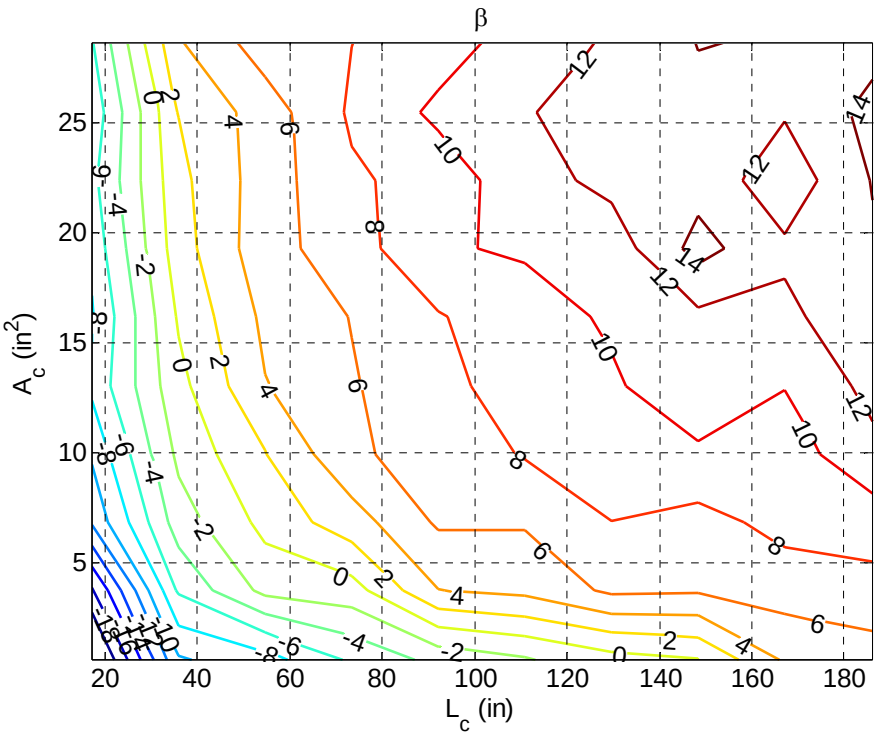

Figure 11.34: β_{50} **, Analysis 14 (RC 2, Grade 36, MCE-MCE),** $R = 8$

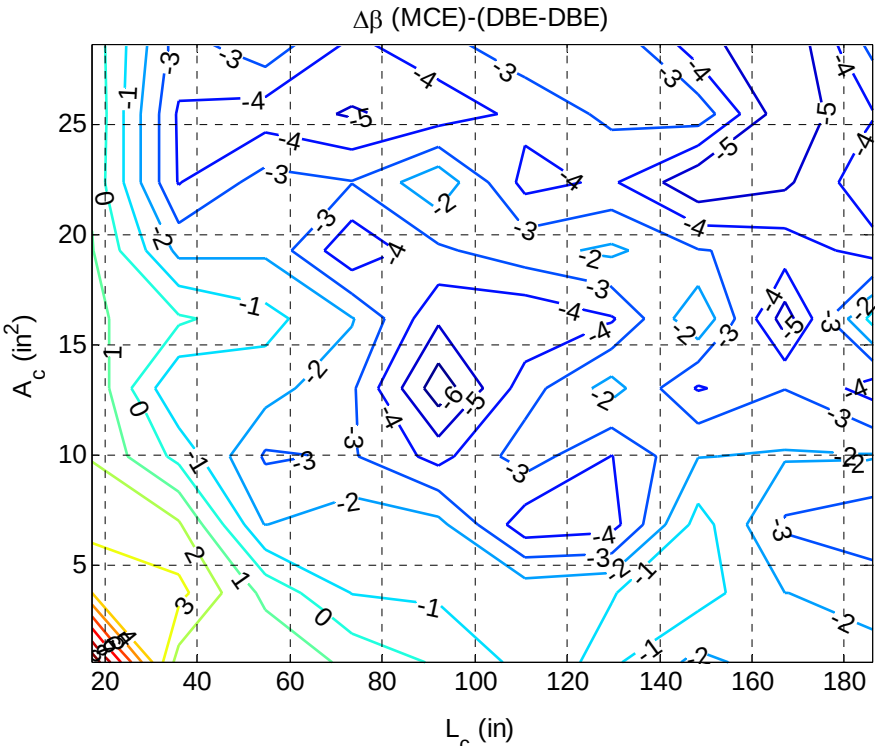

Figure 11.35: Difference in β_{50} **: Analysis 10 (MCE) minus Analysis 11 (DBE-DBE)**

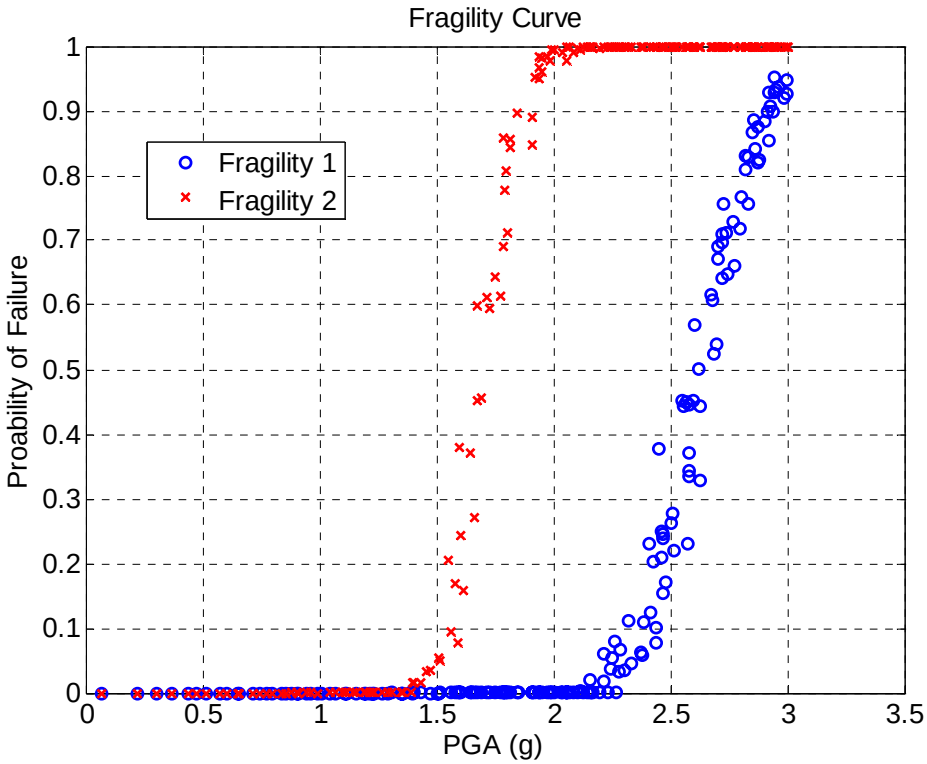

Figure 11.36: Fragility Analyses Results

11.7 Chapter 11 Tables

Table 11.1: List of All Possibly Important Parameters for Analysis

BRB Properties	BRBF Properties	Seismic Loading Properties
A_c	m	Φ_0
A_{nc}	ζ_0	$(S_a)_{target}$
L_c		ϖ_g
L_{nc}		ζ_g
E		$\Psi(t)$: Stationarity and duration
F_y		
F_u		

Table 11.2: Parameters Varied in Parametric Studies

Parameters Directly Varied	Parameters Not Directly Varied
A_c	E
L_c	ζ_0
m	A_{nc}
F_y	L_{nc}
F_u	$\Psi(t)$: Stationarity and duration
Φ_0	
$(S_a)_{target}$	
ϖ_g	
ζ_g	

Table 11.3: Analysis NON DIM A Configuration Parameters

Analysis Name		NON DIM A			
Number of Points[1]:		1600			
Input Module		1			
RC Model		RC 1			
Parameters					
	Parameter	Low[2]	High[3]	N[4]	Set[5]
BRB Parameters	$A_c(in^2)$				3.3
	$A_{nc}(in^2)$				$2A_c$
	$L_c(in)$				127.3
	$L_{nc}(in)$				127.3
	$E(ksi)$				29,000
	$F_y(ksi)$				42.2
	$F_u(ksi)$				65.0
BRBF Parameters	$m(kip*s^2/in)$	2	10	40	
	ζ_0				0.05
Seismic Loading Parameters	$\Phi_0(in^2/s^3)$	50	400	40	
	$(S_a)_{target}(in/s^2)$				NA
	$\varpi_g(rad/s)$				15.7
	ζ_g				0.60
	$\Psi(t)$				$\Psi(t) = 0.45te^{-0.167t}$
	$t_{sim}(s)$				30

1 Total number of reliability analyses performed
2 Lowest value of parameter considered
3 Highest value of parameters considered
4 Number of increments between Low and High parameter values
5 If parameter not varied, this is what it was set as for the analysis.
NA Not applicable to this analysis
Note: All terms are described in the List of Symbols.

Table 11.4: Analysis NON DIM B Configuration Parameters

Analysis Name		NON DIM B			
Number of Points[1]:		1600			
Input Module		1			
RC Model		RC 1			
Parameters					
	Parameter	Low[2]	High[3]	N[4]	Set[5]
BRB Parameters	$A_c(in^2)$	0.5	4	40	
	$A_{nc}(in^2)$	17	75	40	
	$L_c(in)$				127.3
	$L_{nc}(in)$				127.3
	$E(ksi)$				29,000
	$F_y(ksi)$				42.2
	$F_u(ksi)$				65.0
BRBF Parameters	$m(kip*s^2/in)$				1.7
	ζ_0				0.05
Seismic Loading Parameters	$\Phi_0(in^2/s^3)$				45
	$(S_a)_{target}(in/s^2)$				NA
	$\varpi_g(rad/s)$				15.7
	ζ_g				0.60
	$\Psi(t)$				$\Psi(t) = 0.45te^{-0.167t}$
	$t_{sim}(s)$				30

1 Total number of reliability analyses performed
2 Lowest value of parameter considered
3 Highest value of parameters considered
4 Number of increments between Low and High parameter values
5 If parameter not varied, this is what it was set as for the analysis.
NA Not applicable to this analysis
Note: All terms are described in the List of Symbols.

Table 11.5: Parameter Values Defined the Same in All Parametric Study Analyses

Parameters					
	Parameter	Low[2]	High[3]	N[4]	Set[5]
BRB Parameters	$A_c(in^2)$	0.63	28.62	10	
	$A_{nc}(in^2)$				$2A_c$
	$L_c(in)$	17.25	185.9	10	
	$L_{nc}(in)$				$\frac{21.21'-L_c}{2}$
	$E(ksi)$				29,000
BRBF Parameters	R	0	10	10	
	ζ_0				0.05
	$\Psi(t)$				$\Psi(t) = 0.45te^{-0.167t}$

1 *Total number of reliability analyses performed*
2 *Lowest value of parameter considered*
3 *Highest value of parameters considered*
4 *Number of increments between Low and High parameter values*
5 *If parameter not varied, this is what it was set as for the analysis.*
NA *Not applicable to this analysis*
Note: *All terms are described in the List of Symbols.*

Table 11.6: Parameter Values used in Specific Parametric Study Analyses

Analysis	RC Model	$(S_a)_{target}$	t_{sim} (s)	F_y (ksi)	F_u (ksi)
1	RC 1	DBE	30	42	62
2	RC 1	DBE	30	55	72
3	RC 1	MCE	30	42	62
4	RC 1	DBE-DBE	60	42	62
5	RC 1	DBE-MCE	60	42	62
6	RC 1	MCE-DBE	60	42	62
7	RC 1	MCE-MCE	60	42	62
8	RC 2	DBE	30	42	62
9	RC 2	DBE	30	55	72
10	RC 2	MCE	30	42	62
11	RC 2	DBE-DBE	60	42	62
12	RC 2	DBE-MCE	60	42	62
13	RC 2	MCE-DBE	60	42	62
14	RC 2	MCE-MCE	60	42	62

Table 11.7: Fragility Analysis 1 Parameters

Analysis Name		Fragility 1			
Number of Points[1]:		200			
Input Module		1			
RC Model		RC 2			
Parameters					
	Parameter	Low[2]	High[3]	N[4]	Set[5]
BRB Parameters	$A_c(in^2)$				8.35
	$A_{nc}(in^2)$				16.7
	$L_c(in)$				97
	$L_{nc}(in)$				$\frac{21.21'-L_c}{2}$
	$E(ksi)$				29,000
	$F_y(ksi)$				42
	$F_u(ksi)$				62
BRBF Parameters	$m(kip*s^2/in)$				1.7
	ζ_0				0.05
Seismic Loading Parameters	$\Phi_0(in^2/s^3)$	1	2000	200	
	$(S_a)_{target}(in/s^2)$				NA
	$\varpi_g(rad/s)$				15.7
	ζ_g				0.60
	$\Psi(t)$				$\Psi(t) = 0.45te^{-0.167t}$
	$t_{sim}(s)$				30

1 Total number of reliability analyses performed
2 Lowest value of parameter considered
3 Highest value of parameters considered
4 Number of increments between Low and High parameter values
5 If parameter not varied, this is what it was set as for the analysis.
NA Not applicable to this analysis
Note: All terms are described in the List of Symbols.

Table 11.8: Fragility Analysis 2 Parameters

Analysis Name		Fragility 2			
Number of Points[1]:		200			
Input Module		1			
RC Model		RC 2			
Parameters					
	Parameter	Low[2]	High[3]	N[4]	Set[5]
BRB Parameters	$A_c(in^2)$				8.35
	$A_{nc}(in^2)$				16.7
	$L_c(in)$				48
	$L_{nc}(in)$				$\frac{21.21'-L_c}{2}$
	$E(ksi)$				29,000
	$F_y(ksi)$				42
	$F_u(ksi)$				62
BRBF Parameters	$m(kip*s^2/in)$				1.7
	ζ_0				0.05
Seismic Loading Parameters	$\Phi_0(in^2/s^3)$	1	4000	100	
	$(S_a)_{target}(in/s^2)$				NA
	$\varpi_g(rad/s)$				15.7
	ζ_g				0.60
	$\Psi(t)$				$\Psi(t) = 0.45te^{-0.167t}$
	$t_{sim}(s)$				30

1 Total number of reliability analyses performed
2 Lowest value of parameter considered
3 Highest value of parameters considered
4 Number of increments between Low and High parameter values
5 If parameter not varied, this is what it was set as for the analysis.
NA Not applicable to this analysis
Note: All terms are described in the List of Symbols.

Chapter 12

CONCLUSIONS

12.1 Summary

This research developed a performance-based engineering framework (PBEF) for evaluating the risk of fatigue fracture of BRBs subjected to seismic loadings. The overall architecture of the PBEF is presented in Figure 1.4. Components of the PBEF can be divided into three categories: modules, analyses, and results. Modules were mathematical constructs used to model the physical reality; analyses were mathematical simulations performed in Matlab®; and results are the outputs from the analyses. In addition, two analysis tracks were outlined in this research. The first analysis pathway outlines the overall PBEF, while the second is a random vibration analysis that was performed beforehand and used to inform the development of the PBEF. The overall analysis flows and PBEF components are further summarized below.

The components of Analysis Pathway 1, the performance-based engineering framework, include: stochastic modeling of seismic loads; dynamic analyses of the BRBF; cumulative plastic ductility (CPD), i.e. fatigue, models for BRBs; structural reliability analyses; parametric studies on how BRB and BRBF properties affect performance; and fragility modeling. The analysis flow of the pathway is described below.

Using the **seismic loading input module**, input ground acceleration records were randomly generated from power spectrum density models and modulated with envelope functions (to account for non-stationary). The generated time records were used as input excitations to the **BRBF system model**, which was a single-degree-of-freedom lumped-mass system. Within the **BRBF system model,** the BRB hysteretic behavior was modeled using a Bouc-Wen model. **Non-linear dynamic simulations** were performed to obtain BRB core deformation time history records.

This study used **BRB remaining capacity (RC) models**, which, given the BRB core deformation history as inputs, predict the remaining CPD capacity of the brace, where values less than zero indicated failure. These RC models were the result of a significant effort to develop models that predict BRB cumulative plastic ductility capacity. The development of BRB CPD capacity models is outlined in the flowchart presented in Figure 1.3. First, a BRB test database (described in Chapter 2) was compiled based on literature review of brace tests performed by various researchers from the U.S. and other countries; from this test database, predictive parameters were developed (as described in Chapter 3) to be used as inputs to BRB CPD capacity models. Predictive parameters were divided into BRB material properties, geometric properties, and parameters that characterized the imposed deformation history. Following the creation of predictive parameters, CPD capacity models were developed using the maximum likelihood estimation (MLE) method. Three types of capacity models were investigated in this research:

1) End-capacity models: these predict a total, static CPD capacity of BRBs. If the imposed deformation exceeds the end-capacity, the BRB is considered to have failed.

2) Damage models: in these models, damage accumulates with imposed deformation and is measured by a damage index, where 0 indicates no damage, and 1 indicates failure.

3) Remaining capacity models: these are a combination of end-capacity and damage models. They predict the remaining CPD capacity available for a brace, which decreases with the applied deformation history. When remaining capacity reaches 0, the brace is said to fail.

End capacity models were developed first, and are described in Chapter 4. Next, damage models were investigated (Chapter 5). Finally, given lessons learned from the development of end-capacity and damage models, remaining capacity models were developed, and this is described in Chapter 6. Two best RC models, RC 1 and RC 2, were developed for use in the PBEF framework. The predictive equation for each is given below.

RC 1:

$$RC = 2^{-3.434}\left(\frac{A_c}{(A_c)_{\max}}\right)^{0.2019}\left(\frac{L_c}{(L_c)_{\max}}\right)^{0.0466}\varepsilon_{yc}{}^{-1.319}\left(\frac{F_u}{F_y}\right)^{0.2181}\mu_{\max loc}{}^{-0.9883} - 0.8677\mu_c + 185.8\frac{\mu_{\max}}{\mu_c}$$

RC 2:

$$R = 2^{-21.20}\left(\frac{A_c}{(A_c)_{\max}}\right)^{0.425}\left(\frac{L_c}{(L_c)_{\max}}\right)^{0.044}\varepsilon_{yc}{}^{-3.45}\left(\frac{F_u}{F_y}\right)^{-1.46} - 152.9\frac{\mu_c}{\mu_{ult}} - 1.12\frac{\mu_{\max}}{\mu_{ult}}$$

Issues arose with model RC 1 because of the inclusion of the $\mu_{\max loc}$ term, which describes the relative location of the maximum ductility demand in the imposed history, into the predictive equation. Specifically, RC 1 predicted behavior that did not agree with observed behavior. These issues did not arise with model RC 2, which behaved correctly.

Given BRB demand (i.e. core deformation histories generated from the dynamic analyses) and supply (i.e. remaining capacity predicted by the RC models), structural **reliability analyses** were performed to evaluate the probability of brace failure. The analyses were conducted using the first order reliability method (FORM) and were facilitated by using the Matlab® open-source code Finite Element Reliability Using Matlab® (FERUM). In the reliability analyses, the epistemic uncertainty in the fatigue capacity predictions was accounted for explicitly, and, as a result, the probabilities of brace failure were calculated in terms of mean probability, 90% confidence level probability, and 95% confidence level probability.

Using the tools described above, a **parametric study** was conducted to explore the effects of the seismic loading, BRB, and BRBF characteristics on the probability of brace failure. For given seismic loadings, two-dimensional contour plots were constructed from which the probability of brace failure can be determined directly

knowing BRB and BRBF properties. Also, for a given set of BRB and BRBF properties (average values from the BRB test database), **fragility analyses** were performed to create fragility curves that provided conditional probability of brace failure given ground shaking intensity parameters.

Somewhat separate from but related to Analysis Pathway 1 (the PBEF), Analysis Pathway 2 relates to a random vibration analysis, which was actually performed before developing Analysis Pathway 1 and the PBEF. The main purpose of the random vibration analysis was to determine the mean and variance of the BRB core deformation process such that distributions of the deformation descriptor predictor parameters described in Chapter 3 could be evaluated. This was accomplished by performing random vibration analysis using the **BRBF system model**, where the non-linear equations of motion (EOM) were linearized using the equivalent linearization method (ELM). Using the random vibration analysis tools, the effects of seismic loading, BRB, and BRBF properties on the mean and variance of the BRB core deformation process were determined. Thus the effects of the seismic loading, BRB, and BRBF properties on BRB demands and system reliability were quantified, and this information was used to evaluate which terms to include in the parametric studies.

12.2 Conclusions and Future Applications

The primary result from this research effort was development of the PBEF and its components. Specifically, extensive effort was put forth to develop BRB CPD capacity models that are probabilistic (i.e. they have an explicitly quantified model error) and are based upon knowing readily available brace properties (geometric and material properties) and only the imposed deformation history (no brace force data is required). Since the models are probabilistic, they are readily applicable to the PBEF described herein.

In the end, remaining capacity models have been developed that perform adequately in the PBEF framework; however, they may not conform to engineering-level accuracy or precision expectations, and it is obvious that developing both accurate and precise model is incredibly challenging using just basic BRB properties and only the imposed deformation history. The variability in the imposed deformation histories (regular cyclic, to irregular cyclic, to simulated seismic) made it difficult to create precise models. There are three recommended actions to create better BRB CPD capacity models:

1) Obtain knowledge about more BRB properties, particularly those related to ductility (such as ultimate stress and ultimate strain capacity).

2) Implement a more uniform testing program, something perhaps similar to what is required to create a fatigue curve, where the imposed deformation histories are similar (i.e. do not mix cyclic and simulated seismic loadings).

3) Measure both the force and deformation histories of the BRBs and use the information to build capacity models (as Takeuchi et al. [20] did).

Multiple analyses were performed using the PBEF and RC models. The primary analyses were parametric studies that resulted in plots which related the system reliability index to the BRB core area, BRB core length, and the response modification coefficient. They were constructed for given values of other BRB properties (yield strength, ultimate strength, etc.). These could be used directly in a design scenario to evaluate the reliability of a BRB and BRBF in reference to the potential for fatigue fracture given BRB, BRBF, and seismic loading properties. In addition to parametric studies, fragility analyses were performed for a set of example BRB, BRBF, and seismic loading properties (average values from the BRB test database) which produced fragility curves that related peak ground acceleration to the probability of brace failure. These types of curves could be applied in loss assessment studies.

While the analyses performed using the PBEF are specific to a range of BRB, BRBF, and seismic loading properties, the framework itself is flexible enough to allow for alterations to account for (1) different seismic loadings, (2) various BRB and BRBF systems (SDOF, multi-degree-of-freedom, etc.), and (3) new CPD capacity models (such as more precise models developed in the future). Future work may utilize this basic PBEF and its flexibility to develop better, more capable modules and run more advanced analyses. As design paradigms continue to shift away from prescriptive procedures to adaptable performance-based design frameworks, this research may be utilized as-is or in a more-developed form as a useful tool for performance-based design of BRBs and BRBF.

Appendix A

Table A.1: BRB Test Database is located in the attached APPENDIX FILES.

Table A.2: BRB Deformation Histories is located in the attached APPENDIX FILES.

Appendix B

Table B.1: BRB Deformation History Parameters is located in the attached APPENDIX FILES.

Deformation Calculations Plots are presented in the attached APPENDIX FILES, that, for each specimen, present:

- The imposed deformation history divided into core, not-core, plastic, and elastic deformation;
- Histogram of the Rainflow distribution for total deformation;
- Histogram of the Rainflow distribution for plastic deformation; and
- Histogram of the Rainflow distribution for elastic deformation.

The Matlab® m-files used to perform deformation calculations are summarized in the table below. The code files themselves are located in the attached APPENDIX FILES.

Table B.2: M-files used for Deformation Calculations

Filename	Purpose
DefCalcs.m	Performs the deformation calculations described in 2.3 given BRB properties (Table A.1) and imposed deformation histories (Table A.2).
Rainflow.m	A function which is called in the DefCalcs.m file that calculates the Rainflow distribution (see Section 3.3.4)

Appendix C

Remaining Capacity History Comparisons

Plots comparing the predicted and measured remaining capacity (for both the RC 1 and RC 2 models) over the imposed deformation history for all specimens that had ultimate stress information available are presented in the attached APPENDIX FILES.

M-files for End-Capacity Models

All five types of end-capacity models used the same basic codes. These m-files are described in the table below. The code files for all end-capacity models are located in the attached APPENDIX FILES.

Table C.1: M-Files for End-Capacity Models

Filename	Purpose
BM_Controller.m	Controls the entire capacity modeling process and calls the other codes listed in this table
BM_EA.m	Performs error analysis to quantify μ_Z and COV_Z (see Section 4.4)
BM_Input.m	Input variables for the capacity modeling process
BM_LookForward.m	Code used to estimate which parameters to remove in the model reduction process (see Section 4.4)
BM_Output.m	Produces outputs from the process, including Excel files and graphs
GammaFunction.m	This function is the formulation of the capacity equation (Section 4.1)
lhood.m	Performs parameter estimation using the MLE method and the likelihood function (see Section 4.2)

M-files for Damage Models

The m-files used to develop the augmented damage models are the same as those for the end-capacity models outlined above. They are located in the attached APPENDIX FILES.

M-files for Remaining Capacity Models

All remaining capacity models were developed using the same codes which are summarized in the table below. The code files are located in the attached APPENDIX FILES.

Table C.2: M-files for Remaining Capacity Models

Filename	Purpose
RemCapController_Yaxisintervals.m	Controls the entire process and divides the imposed deformation history into even Y-axis increments
RemCapBM.m	Controls the parameter estimation process and calls the lhood.m code (Section 6.2)
lhood.m	Performs parameter estimation using the MLE method and the likelihood function (Section 6.2)
RemCapPredict.m	This function is the formulation of the remaining capacity equation (Section 6.1)
Rainflow.m	Function which performs the Rainflow calculations (Section 3.3.4)
DefCalcsFunction.m	Function which performs deformation calculations to obtain deformation history predictive parameters (Section 3.3)

Appendix D

Files for Performance-Based Engineering Framework (Analysis Pathway 1)

Files utilized in Analysis Pathway 1 are summarized in the following table. They are located in the attached APPENDIX FILES.

Table D.1: Files for Analysis Pathway 1

Filename	Purpose
RSC.m	Main controller code for Analysis Pathway 1; calls Simulink® files and FERUM code
ferum.m	Main FERUM code which calls the FORM code (Section 10.5)
form.m	Performs FORM to determine probability of failure and sensitivities (Section 10.5)
RSCSys_PSD.sim	Simulink® model for system with Input Module 2 (Figure 8.3)
RSCSyst_WN.sim	Simulink® model for system with Input Module 1 (Figure 8.3)
RSPostContour.m	Post-processes the results from the RSC.m code to produce reliability surface contour plots (Section 11.6)
RSC_Compare.m	Post-processes the results from the RSC.m code to compare results from difference analyses (e.g. Figure 11.35)
RSPost4D.m	Post-processes the results from the RSC.m code to produce spectral acceleration plots (e.g. Figure 11.11)
FragPost.m	Post-processes the results from the RSC.m code to produce the fragility analysis results (Section 11.4)
InputGenFxn.m	Generates the acceleration time history values given an input PSD function (Sections 7.2 and 7.3)
PSDGenFxn	Calibrates the input PSD function such that acceleration time history values produced conform to a target spectrum (Section 7.3)
nsim_determination.m	Matlab® code used to determine the number of simulations necessary for convergence of random variables (see Section 10.2)

Files for Random Vibration Analysis (Analysis Pathway 2)

M-files utilized in Analysis Pathway 2 are summarized in the following table. They are located in the attached APPENDIX FILES.

Table D.2: Files for Analysis Pathway 2

Filename	Purpose
Input.m	Contains all inputs for the various analyses; called at the beginning of all analysis codes
Simulation.m	Performs the Monte Carlo simulation (Section 9.3.2); calls Simulink® model System.sim during use
System.sim	Simulink® model of the BRBF system used in Monte Carlo simulation
TVLyap.m	Solves the time-varying Lyapunov equation given by (9.10)
StaLyap.m	Solves the stationary Lyapunov equation given by (9.9)
PostProcess.m	Compares results from the three analysis methods; used to print the figures shown in Section 9.6
lyapfun.m	A function called in the TVLyap.m code
Sensitivity.m	Performs design iterations to explore the effects of BRB and BRB parameters on the variance of the core deformation process (Section 9.4.4)
StaLyapSe.m	Same as StaLyap.m but formatted for the sensitivity.m code

References

[1] Black, C.J., Makris, N., and Aiken, I.D. "Component Testing, Seismic Evaluation, and Characterization of Buckling-Restrained Braces." *Journal of Structural Engineering, ASCE*, Vol. 130, No. 6, 2004, pp. 880-894.

[2] Merritt, S., Uang, C., and Gianmario, B. "Subassemblage Testing of Corebrace Buckling-Restrained Braces." *Report No. TR-2003/01*, The University of California, San Diego, 2003.

[3] Merritt, S., Uuang, C., and Gianmario, B. "Subassemblage Testing of Star Seismic Buckling-Restrained Braces." *Report No. TR-2003/04*, The University of California, San Diego, 2003.

[4] Tsai, K., Loh, C., Hwang, Y., and Went, C.. "Seismic Retrofit of Building Structures with Dampers in Taiwan." *Proceedings of Symposium of Seismic Retrofit of Buildings and Bridges with Base Isolation and Dampers*, January 17, 2003.

[5] Usami, T., Kasai, A., and Kato, M. "Behavior of Buckling-Restrained Brace Members." *Proceedings of the Conference on Behaviour of Steel Structures in Seismic Areas*, June 9-12, 2003.

[6] Iwata, M., and Murai, M.. "Buckling-Restrained Brace Using Steel Mortar Planks; Performance Evaluation as a Hysteric Damper." *Earthquake Engineering and Structural Dynamics*, Vol. 35, No. 14, 2006, pp. 1807-1826.

[7] Iwata, M. and Kato, T.. "Buckling-Restrained Braces as Hysteric Dampers." B*ehaviour of Steel Structures in Seismic Areas: Proceedings of the Third International Conference STESSA 2000,* August 21-24, 2000.

[8] Watanabe, A. "Development of Composite Brace with a Large Ductility." *Proceedings of U.S.–Japan Workshop: Composite and Hybrid Structures*, September 10-12, 1992.

[9] Carden, L.P., Itani, A.M., and Buckle, I.G. "Cyclic Behavior of Buckling-Restrained Braces for Ductile End Cross Frame." *Engineering Journal,* AISC, Vol. 43, No. 2, 2006, pp. 127-139.

[10] Carden, L.P., Itani, A.M., and Buckle, I.G. "Seismic Performance of Steel Girder Bridges with Ductile Cross Frames Using Buckling-Restrained Braces." *Journal of Structural Engineering,* ASCE, Vol. 132, No. 3, pp. 338-345

[11] Reaveley, L.D., Okahashi, T., and Farr, C. "Corebrace Series E Buckling-Restrained Brace Test Results." The University of Utah, 2004.

[12] Benzoni, G., and Innamorato, D.. "Star Seismic Brace Tests: Mercy San Juan Hospital Project." *Report No. SRMD-2007/05*, The University of California, San Diego, 2007.

[13] Romero, P., Reavely, L.D., Miller, P.J., and Okahashi, T. "Full Scale Testing of WC Series Buckling-Restrained Braces." The University of Utah, 2006.

[14] Tremblay, R., Bolduc, P., Neville, R., and DeVall, R. "Seismic Testing and Performance of Buckling-Restrained Bracing Systems." *Canadian Journal of Civil Engineering*, Vol. 33, No. 2, 2006, pp. 183-198.

[15] Newell, J., Uang, C., and Benzoni, G.. "Subassemblage Testing of Corebrace Buckling-Restrained Braces (F-Series)." *Report No. TR-05/01*, The University of California, San Diego, 2005.

[16] Fahnestock, L.A., Ricles, J.M., and Sause, R. "Experimental Evaluation of a Large-Scale Buckling-Restrained Braced Frame." *Journal of Structural Engineering*, ASCE, Vol. 133, No. 9, 2007, pp. 1205-1214.

[17] Aiken, I.D., Mahin, S.A., and Uriz, P. "Large-Scale Testing of Buckling Restrained Braced Frames." *Proceedings, Japan Passive Control Symposium*, Tokyo Institute of Technology, Yokohama, Japan, December 2002.

[18] Tsai, K.C., Hsiao, B.C., Lai, J.W., Chen, C.H., Lin, M.L., and Weng, Y.T.,"Pseudo Dynamic Experimental Response of a Full Scale CFT/BRB Composite Frame." *Proceedings of the Joint NCREE/JRC Workshop on International Collaboration on Earthquake Disaster Mitigation Research*, Tapei, Taiwan, 2003.

[19] Fahnestock, L.A., Sause, R., Ricles, J.M. "Seismic Response and Performance of Buckling-Restrained Braced Frames." *Journal of Structural Engineering*, ASCE, Vol. 133, No. 9, 2007, pp. 1195-1204.

[20] Takeuchi, T., Ida M., Yamada, S., and Suzuki K. "Estimation of Cumulative Deformation Capacity of Buckling Restrained Braces." *Journal of Structural Engineering,*Vol. 134, No. 5, 2008, pp. 822-831.

[21] Benavent-Climent, A. "An Energy-Based Damage Model for Seismic Response of Steel Structures." *Earthquake Engineering and Structural Dynamics*, Vol. 36, No. 8, 2007, pp. 1049-1064.

[22] ASTM 1049-85. "Standard Practices for Cycle Counting in Fatigue Analysis." 2005.

[23] Song, J., Kang, W.-H., Kim, K.S., and Jung, S. "Probabilistic Shear Strength Models for Reinforced Concrete Beams Bayesian Updating Based on Experimental Observations." *Proceedings of the 5th Conference on Computational Stochastic Mechanics*, Rodos, Greece, June 21-23, 2006, pp. 623-632.

[24] Park, Y.-J., and Ang, A.H.-S. "Mechanistic Seismic Damage Model for Reinforced Concrete." *Journal of Structural Engineering*, ASCE, Vol. 111, No. 4, 1985, pp. 722-739.

[25] Fahnestock, L. A., Sause, R., and Ricles, J. M. "Analytical and Large-Scale Experimental Studies of Earthquake-Resistant Buckling-Restrained Braced Frame Systems." *Advanced Technology for Large Structural Systems Report No. 06-01,* September, 2006.

[26] Der Kiureghian, A. "First- and Second-order Reliability Methods." *Engineering Design Reliability Handbook*, edited by E. Nikolaidis, D.M. Ghiocel, and S. Singhal, CRC Press, Boca Raton, FL, 2005, Chap. 14.

[27] "Finite Element Reliability Using Matlab." <http://www.ce.berkeley.edu/FERUM/> Accessed January 2008.

[28] Wen, Y.K. "Equivalent Linearization for Hysteric Systems under Random Excitation." *Mechanical Engineering*, ASME, Vol. 47, No. 3, 1980, pp. 150-154.

[29] Kanai, K. "Semi-empirical Formula for the Seismic Characteristics of the Ground." *University of Bull., Earthquake Research Institute,* Vol. 35, 1957, pp. 309-325.

[30] Tajimi, H. "A Statistical Method of Determining the Maximum Response of a Building Structure during an Earthquake." *Proceedings of the 2nd World Conference on Earthquake Engineering,* Tokyo and Kyoto, Vol. II, 1960, pp. 781-798.

[31] Clough, R.W., and Penzien, J. "Dynamics of Structures." Computers and Structures, Inc.: Berkeley, CA, 1985, pp. 598-603.

[32] American Society of Civil Engineers. “Minimum Design Loads for Buildings and Other Structures.” *ASCE Standard ASCE/SEI 07-05*, 2005, pp. 109-118.

[33] Sabelli, R. et al. “Seismic Demands on Steel Braced Frame Buildings with Buckling-Restrained Braces.” *Engineering Structures*, Vol. 25, 2003, pp. 655-666.

[34] Akiyama, H. “Earthquake-Resistant Design Method for Buildings based on Energy Balance.” Gihodo Press, Tokyo, 1999, (in Japanese).

[35] Gardoni, P. “Probabilistic models and fragility estimates for structural components and systems.” *Ph.D. Thesis*, University of California, Berkeley, California, 2002.

[36] Devore, J. L. “Probability and Statistics: Fifth Edition.” Brooks/Cole: Pacific Grove, CA, 2000, pp. 267-273.

[37] Deodatis, G. and Shinozuka, M. “Stochastic wave models for stationary and homogeneous seismic ground motion.” *Structural Safety*, V. 10, No. 1-3, May 1991, pp. 235-246.

[38] Song, J., and A. Der Kiureghian. “Generalized Bouc-Wen model for highly asymmetric hysteresis.” *Journal of Engineering Mechanics*, ASCE, Vol. 132, No. 6, 2006, pp. 610-618.

[39] Dormand, J. R., and P. J. Prince. “A family of embedded Runge-Kutta formulae." *Journal of Applied Computational Mathematics*, Vol. 6, 1980, pp 19-26.

[40] Silva, Clarence W. *Vibration: Fundamentals and Practice (2nd Edition)*. Taylor and Francis: New York, 2007, pages 185-191.

[41] Atalik, T. S., and Utku, S. “Stochastic Linearization of Multidegree-of-Freedom Nonlinear Systems.” *Journal of Earthquake Engineering and Structural Dynamics*, Vol. 4, 1976, pp. 411-420.

[42] Bartels, R.H. and G.W. Stewart. "Solution of the Matrix Equation AX + XB = C." *Comm. of the ACM,* Vol. 15, No. 9, 1972.

[43] Stuart, A., Ord, K., and Arnold S. *Kendall's Advanced Theory of Statistics. T. 2A*. London: Arnold, a member of the Hodder Headline Group, 1999, ss. 25.37-25.43.

[44] Nielson, B. G. and DesRoches R. “Analytical seismic fragility curves for typical bridges in the Central and Southeastern United States.” *Earthquake Spectra,* Vol. 23, No. 3, 2007.

List of Recent NSEL Reports

No.	*Authors*	*Title*	*Date*
001	Nagayama, T. and Spencer, B.F.	Structural Health Monitoring Using Smart Sensors	Nov. 2007
002	Sun, S. and Kuchma, D.A.	Shear Behavior and Capacity of Large-Scale Prestressed High-Strength Concrete Bulb-Tee Girders	Nov. 2007
003	Nagle, T.J. and Kuchma, D.A.	Nontraditional Limitations on the Shear Capacity of Prestressed, Concrete Girders	Dec. 2007
004	Kwon, O-S. and Elnashai, A.S.	Probabilistic Seismic Assessment of Structure, Foundation, and Soil Interacting Systems	Dec. 2007
005	Nakata, N., Spencer, B.F., and Elnashai, A.S.	Multi-dimensional Mixed-mode Hybrid Simulation: Control and Applications	Dec. 2007
006	Carrion, J. and Spencer, B.F.	Model-based Strategies for Real-time Hybrid Testing	Dec. 2007
007	Kim, Y.S., Spencer, B.F., and Elnashai, A.S.	Seismic Loss Assessment and Mitigation for Critical Urban Infrastructure Systems	Jan. 2008
008	Gourley, B.C., Tort, C., Denavit, M.D., Schiller, P.H., and Hajjar, J.F.	A Synopsis of Studies of the Monotonic and Cyclic Behavior of Concrete-Filled Steel Tube Members, Connections, and Frames	April 2008
009	Xu, D. and Hjelmstad, K.D.	A New Node-to-node Approach to Contact/Impact Problems for Two Dimensional Elastic Solids Subject to Finite Deformation	May 2008
010	Zhu, J. and Popovics, J.S.	Non-contact NDT of Concrete Structures Using Air Coupled Sensors	May 2008
011	Gao, Y. and Spencer, B.F.	Structural Health Monitoring Strategies for Smart Sensor Networks	May 2008
012	Andrews, B.M., Fahnestock, L.A. and Song, J.	Performance-based Engineering Framework and Ductility Capacity Models for Buckling-Restrained Braces	July 2008